Thermal budgets of magma storage constrained by diffusion chronometry: the Cerro Galán ignimbrite

Jordan Lubbers[1,2*], Adam Kent[1], Shanaka de Silva[1]

[1]College of Earth, Ocean, and Atmospheric Sciences, Oregon State University, Corvallis OR, 97331, USA

Now at:

[2]Alaska Volcano Observatory U.S. Geological Survey, Anchorage AK, 99508, USA

[*]Corresponding author: jelubber@gmail.com (920) 737-4821

ABSTRACT

The long-term thermochemical conditions at which large bodies of silicic magma are stored in the crust is integral to our understanding of the timing, frequency, and intensity of volcanic eruptions, and provides important context for interpreting volcano monitoring data. Despite this, however, individual magmatic systems may exhibit a range of time-temperature paths, or thermal histories, that are the result of many complex and, in some cases competing processes. This complexity contributes to an incomplete understanding of the long-term thermal evolution of magma stored within the Earth's crust. Of recent interest to the volcanology community is the length of time large volumes of rheologically eruptible and geophysically detectable magma exist within the crust prior to their eruption. Here we use a combination of diffusion chronometry, trace element, and thermodynamic modeling to quantify the long-term thermal evolution of the 2.08 Ma, 630km^3 Cerro Galán Ignimbrite (CGI) in NW Argentina; one of the largest explosive volcanic eruptions in the recent geologic record. We find that diffusion of both Mg and Sr in plagioclase indicate that erupted magmatic material only spent decades to centuries at or above temperatures (~750°C) required to maintain significant volumes of stored eruptible magma. Calculated plagioclase equilibrium compositions reveal an array of liquids that is controlled overall by fractionation of plagioclase + biotite + sanidine, although high-resolution trace element transects record a diversity of fractionation pathways. Overall, we suggest that there is compelling evidence that the magma erupted from the CGI magmatic system spent most of its upper crustal residence in a largely uneruptible state and was rapidly remobilized shortly before eruption.

INTRODUCTION

Large silicic magma reservoirs, responsible for producing the biggest explosive volcanic eruptions in the geologic record (Mason *et al.*, 2004; Wilson *et al.*, 2021), exist as local thermal anomalies in the otherwise cold mid- to upper- continental crust (Turcotte and Schubert, 2002; Huber *et al.*, 2019). Maintaining magma volumes that are sufficiently melt-rich to erupt reflects a balance between conductive cooling, advective gain or loss of heat via eruption and the addition of recharge magma, and latent heat of crystallization (Degruyter and Huber, 2014). Because of this, rapid addition of magma is thought to be necessary to grow and sustain large volumes of magma in the upper crust (Gelman *et al.*, 2013; de Silva and Gregg, 2014; Annen *et al.*, 2015). Individual magma systems (and different regions within a single magma system) may also have unique time-temperature paths, or thermal histories, that are the amalgamation of many complex and, sometimes, competing processes (e.g., recharge, eruption, second boiling, thermal buffering, magma ascent, etc.; Rout et al., 2021). Gaining a better understanding of the thermal state and evolution of a magma reservoir, although a challenging endeavor, remains important as it has been shown to be responsible for controlling important processes such as eruption timing, frequency, and dynamics (Degruyter and Huber, 2014).

The thermal histories of crustal magma systems, and the conditions that give rise to large bodies of eruptible magma, have been investigated for several decades using numerical modeling (Annen et al., 2006; Gelman et al., 2013; Jellinek and DePaolo, 2003; Karakas et al., 2017) and, more recently, these issues have been investigated by petrological and geochemical techniques. The latter are based on a range of approaches, including single mineral geochronology (Klemetti *et al.*, 2011; Barboni *et al.*, 2016; Andersen *et al.*, 2017; Szymanowski *et al.*, 2017), thermobarometry and phase equilibria (Walker *et al.*, 2013) or a combination of these approaches. Additionaly, in recent years, diffusion chronometry in a range of different minerals (Bradshaw, 2017; Cooper and Kent, 2014; Rubin et al., 2017; Shamloo and Till, 2019) has also emerged as a powerful way to constrain the thermal evolution of magmas. Although diffusion chronometry is more often used to quantify timescales of short duration magmatic processes – typically those associated with the buildup to eruption (Rubin *et al.*, 2017; Ruth *et al.*, 2018; Shamloo and Till, 2019; Couperthwaite *et al.*, 2020; Mutch *et al.*, 2021) – mineral and element pairs with slower diffusivities at temperatures relevant to silicic magmatic systems can also be

used to study longer term magmatic processes (e.g. crystal storage, magma recharge; Cooper and Kent, 2014; Rubin et al., 2017).

Based on these studies, two broad end-member models have emerged. In the first model crustal magma reservoirs spend the vast majority of their time at near-solidus conditions, where they are not eruptible, and experience punctuated thermal events that generate eruptible volumes of magma (Cooper and Kent, 2014; Rubin *et al.*, 2017; Szymanowski *et al.*, 2017). This model is supported by geophysical approaches, which rarely observe melt-dominated (greater than 50%) magma reservoirs (Lundstrom and Glazner, 2016), although some exceptions to this may exist (Laumonier *et al.*, 2019). In contrast, the second model argues that magma reservoirs spend the vast majority of their time at temperatures that allow for the presence of a significant and eruptible melt fraction throughout much of their history to be present (Barboni et al., 2016; Kaiser et al., 2017; Tierney et al., 2016).

These end-member models imply distinctly different thermal behavior within the associated magmatic reservoir and are important to constrain. However, just considering two end-member possibilities is also likely to obscure important details about the complexity of magmatic systems, and larger magmatic reservoirs likely exhibit both storage types within a single continuously evolving or integrated magmatic system (Andersen *et al.*, 2017; Bradshaw, 2017; Mucek *et al.*, 2021). Previous thermal history investigations have focused largely on systems that erupt both relatively small volumes of magma (Barboni et al., 2016; Cooper and Kent, 2014; Rubin et al., 2017; Tierney et al., 2016; Till et al., 2015) and those that erupt significantly larger volumes of magma (Andersen *et al.*, 2017; Bradshaw, 2017; Szymanowski *et al.*, 2017; Shamloo and Till, 2019). However, many of these also utilize relatively small datasets for an individual eruption, and thus are less suitable to see if there is complexity in the thermal histories experienced by different magmatic components within an individual magma reservoir.

One way to investigate this issue further is to conduct more detailed studies of a single large eruption, and to combine constraints from diffusion modeling with other petrologic approaches (e.g., thermometry, geochemical and thermodynamic modeling) to provide additional context within which to interpret results. In addition, use of multiple trace elements for diffusion modeling can also make diffusion constraints more robust (Chamberlain et al., 2014; Morgan and Blake, 2006; Shamloo and Till, 2019; Till et al., 2015). Here we utilize diffusion modeling of Sr and Mg in plagioclase and detailed documentation of core to rim changes in plagioclase

chemistry in the 2.08 Ma, 630 km^3 Cerro Galán Ignimbrite (Folkes *et al.*, 2011c; Kay *et al.*, 2011). We also combine these results with thermodynamic modeling (Gualda *et al.*, 2012) and other petrological observations to constrain the long-term thermal evolution in this system.

Geologic Background

The Cerro Galán caldera, located in northwest Argentina on the eastern edge of the Puna plateau, is a part of the larger Central Volcanic Zone of the Andes (Figure 1). Between 5.6 and 2.08 Ma the Cerro Galán magmatic system produced a total of > 1200km^3 of high-K, crystal rich (40-50%), homogenous (68-71wt% SiO_2) rhyodacite (Folkes *et al.*, 2011a, 2011c) that has been classified as a series of 'monotonous intermediates' (Hildreth, 1981). The largest and most recent eruption, the 2.08 Ma Cerro Galán Ignimbrite (CGI), produced 630km^3 of ignimbrite that extends at least 40 km outward from the caldera in all directions and up to 80km north of the caldera (Folkes *et al.*, 2011c).

The CGI is a massive, crystal-rich (40-50% crystals), and generally pumice poor ignimbrite with a mineral assemblage of plagioclase (20%) + quartz (10%) + biotite (10%) + Fe-Ti oxides (3%) + sanidine (1%) + apatite (1%) + zircon (0.5%). The majority of pumice have between 69-71 wt% SiO_2, however, two types of pumice are evident (Wright *et al.*, 2011): 1) the majority of pumice (~95%) are "white pumice" that contain 44 – 57% crystals, no microlites, > 76 wt.% SiO_2 groundmass, and higher Ba concentrations; 2) a volumetrically small proportion of pumice (~5%) are "grey pumice" that contain 35 – 59% crystals, abundant microlites, groundmass SiO_2 concentrations of 69 – 74 wt.%, and ~150 ppm lower Ba concentrations at equivalent SiO_2 concentrations as white pumice. Fe-Ti oxide geothermometry on white pumice record temperatures of 790-820°C (Wright *et al.*, 2011); however, Folkes et al., (2011) note that due to the high fO_2 (+1-1.7 NNO) calculated for the CGI these temperature estimates may have uncertainties of 50-100 °C. Trace element ratios in the CGI, when compared to previous ignimbrites from the Galán magmatic system, indicate a closed system (Folkes *et al.*, 2011b). Appearance of sanidine in the CGI, coupled with the disappearance of amphibole present in previous eruptions from the Cerro Galán system has been experimentally demonstrated to be the result of a shallowing of the magmatic system over time, and this is also supported by volatile contents in quartz-hosted melt inclusions (Grocke *et al.*, 2017). Previous reconnaissance studies (Folkes *et al.*, 2011b; Wright *et al.*, 2011) of the thermal evolution of the Cerro Galán Ignimbrite indicate that there are multiple populations of plagioclase with one population recording magma

storage for long durations at high temperature (> 750 °C; type 1), while the other dominant population records short time at high temperature (type 2). Additionally, these different plagioclase populations contain unique trace element signatures with type 1 plagioclase exhibiting a positive correlation between Ba and An, while type 2 exhibits a negative correlation. This has been interpreted as being the result of plagioclase recording crystallizing environments in which the magma system switches from conditions that inhibit sanidine crystallization (type 2) to those that promote it (type 1) as the magma system shallows with time (Bradshaw, 2017). It is also possible, however, that these trends may be heavily influenced by the presence of biotite (up to 15 vol% vs. 1.5 vol% sanidine in the CGI) and reflect a magma reservoir with diverse crystallization conditions, further establishing the need for an in depth, multidisciplinary assessment of the time-temperature evolution of the Cerro Galán magmatic system.

METHODS

Bulk Rock Geochemistry

Eight samples from representative locations around the Cerro Galán caldera were chosen for bulk rock geochemical analysis (Figure 1). Samples were analyzed at Washington State University for both major (SiO_2, TiO_2, Al_2O_3, FeO, MnO, MgO, CaO, Na_2O, K_2O, P_2O_5) and trace element (La, Ce, Pr, Nd, Sm, Eu, Gd, Tb, Dy, Ho, Er, Tm, Yb, L, Ba, Th, Nb, Y, Hf, Ta, U, Pb, Rb, Cs, Sr, Sc, Zr, V, Cr, Ni, Cu, Zn, Ga) compositions. Major elements, high field strength elements (HFSE), and their corresponding uncertainties were characterized using a ThermoARL AdvantXP XRF and the method of Johnson et al. (1999). Rare earth elements (REE) and remaining trace elements along with their uncertainties were measured by inductively coupled plasma mass spectrometry (ICP-MS) using an Agilent 7700 Q-ICP-MS according to Knaack et al. (1994). Bulk rock major and trace element concentrations, along with their uncertainties can be found in online Supplementary spreadsheet.

Electron Probe Micro Analysis

Major element (Na, Si, Al, Fe, Ca, K, Mg, Ti) spot analyses and backscattered electron (BSE) images of plagioclase were conducted using Cameca SX100 electron probe microanalyzer (EPMA) at Oregon State University with a focused beam of 5μm, 15kV accelerating voltage, and 30nA current beam current. Calibration used standard reference material NMNH 115900.

Uncertainties were calculated by repeated measurement of standard reference materials. Average measured values, accepted values, and their uncertainties can be found in Table 1.

Laser Ablation Inductively Coupled Plasma Mass Spectrometry (LA-ICP-MS)

Trace element analyses of pumice glass and plagioclase were conducted using a Photon Machines Analyte G2193 ArF Excimer laser system connected to a ThermoFisher Scientific iCAP-RQ ICP-MS at the Oregon State University W.M. Keck Collaboratory for Plasma Spectrometry. Analyses used the following isotopes: plagioclase - ^{7}Li, ^{24}Mg, ^{27}Al, ^{29}Si, ^{43}Ca, ^{48}Ti, ^{57}Fe, ^{88}Sr, ^{138}Ba, ^{139}La, ^{140}Ce, ^{153}Eu, ^{208}Pb; pumice glass - ^{24}Mg, ^{43}C, ^{48}Ti, ^{59}Co, ^{85}Rb, ^{88}Sr, ^{89}Y, ^{90}Zr, ^{93}Nb, ^{137}Ba, ^{139}La, ^{140}Ce, ^{141}Pr, ^{146}Nd, ^{147}Sm, ^{153}Eu, ^{157}Gd, ^{163}Dy, ^{166}Er, ^{172}Yb, ^{178}Hf, ^{208}Pb, ^{232}Th, ^{238}U. Analyses of plagioclase were conducted as a line of spots with dimensions 5 by 50 μm with 5 μm between spot centers, pulse rate of 50 Hz, and analysis time of 10 seconds per spot. This approach allows for high spatial resolution to be maintained in the direction of the transect, while still allowing for higher count rates to improve precision. Ablated material was carried to the mass spectrometer using an Aerosol Rapid Introduction System (ARIS; Teledyne Photon Machines Inc., Bozeman MT, USA) microcapillary tube to decrease washout time, allow for easier ablation peak identification, and help improve detection of low concentration elements. All total, 81 plagioclase transects across 9 samples were gathered. Profile locations within individual plagioclase were chosen following the advice provided in Shea et al., (2015) to mitigate the influence of sectioning effects and merging diffusion fronts in our diffusion models. Trace element analyses of microlite free pumice glass were conducted using 30 μm diameter circular spots, a pulse rate of 7 Hz, laser energy of 6.42 J·cm^{-2}, and analysis time of 30 seconds per spot. A total of 16 glass analyses were utilized in this study.

Elemental concentrations were calculated from analyte raw signals using the methodology of Kent and Ungerer, (2006), Longerich et al., (1996) and the software LaserTRAM-DB (Lubbers *et al.*, 2021). Anorthite contents of plagioclase were calculated using measured Ca/Si ratios similar to the method of (Kent *et al.*, 2008). BCR-2G was used as the calibration standard and was analyzed every 5 profiles or 10 spot analyses (i.e., ~15 minutes of analysis time) along with ATHO-G to monitor for drift in the mass spectrometer. BCR-2G, ATHO-G, NIST-612, and BHVO-2G were run as standard blocks at the beginning, middle, and end of each experiment. Their concentrations and uncertainties can be found in the Supplementary Data. Analyses suggest precision for trace elements measurements in all

materials are < 5% except for heavy rare earths, Co, and V in glass analyses, which are < 10-15%.

Diffusion Chronometry

This study utilizes Mg and Sr diffusion in plagioclase to quantify the duration that a given crystal (or area of a crystal) has resided in a magma a certain temperature. Trace element partitioning in plagioclase is dependent on anorthite (An) content (Bindeman *et al.*, 1998; Dohmen and Blundy, 2014; Nielsen *et al.*, 2017) and follows an Arrhenius relationship such that:

1. $RT\,ln(K_D) = AX_{An} + B$

Where R is the gas constant, T is temperature in Kelvin, K_d is the partition coefficient, X_{An} is the molar fraction of anorthite, and both A and B are constants (Bindeman *et al.*, 1998; Nielsen *et al.*, 2017). Likewise, the rate at which self-diffusion of both Mg and Sr occurs within plagioclase is dependent on An content (Cherniak and Watson, 1994; Giletti and Casserly, 1994; LaTourrette and Wasserburg, 1998; Costa *et al.*, 2003; Van Orman *et al.*, 2014). Having both the partition and diffusion coefficient values dependent on An content then necessitates a diffusion equation that incorporates these observations. As such we utilize the solution from Costa et al. (2003) to model how Mg and Sr profiles will change with both space (x) and time (t):

2. $$\frac{\delta C}{\delta t} = \left(\frac{\delta D}{\delta x}\frac{\delta C}{\delta x} + D\frac{\delta^2 C}{\delta x^2}\right) - \frac{A}{RT}\left(D\frac{\delta C}{\delta x}\frac{\delta X_{An}}{\delta x} + C\frac{\delta D}{\delta x}\frac{\delta X_{An}}{\delta x} + DC\frac{\delta^2 X_{An}}{\delta x^2}\right)$$

Where D is the diffusion coefficient of the trace element being modeled, C is the concentration of that trace element measured at a given point, and A is the thermodynamic constant from Equation 1. This solution to the diffusion equation proceeds towards an equilibrium profile that is dictated by the observed An profile as well as the composition of plagioclase that is in equilibrium with the melt at the time of eruption (e.g., the rim).

We model the modification of Sr and Mg contents in plagioclase via diffusion using a finite difference forward model following the method of Costa et al. (2008) adapted to Equation 2 (see Appendix 1 for discretized version used in the model). Diffusion coefficients for Mg and Sr were taken from Van Orman et al. (2014) and Giletti and Casserly (1994), respectively, and are shown in $\mu m^2 \cdot s^{-1}$ below:

$$D_{Mg} = 10^{12}\left(exp\left[\frac{-6.06 - 7.96X_{An} - 287{,}000}{RT}\right]\right)$$

$$D_{Sr} = 10^{12}\left(2.92 \cdot 10^{-4.1X_{An}-4.08} exp\left[\frac{-276{,}000}{RT}\right]\right)$$

When compared to the diffusion coefficient used in Costa et al. (2003), Van Orman et al. note that their relationship has a weaker compositional dependence and stronger temperature dependence. This ultimately leads to Mg diffusion coefficient values to be roughly a factor of 5 slower than those calculated using Costa et al. (2003) at CGI plagioclase An values. We argue that by using the relationship from Van Orman et al. (2014), then, that our Mg diffusion times are more reflective of potential "maximums" than if the Costa et al. (2003) value was used. Equilibrium profiles were calculated by using Equation 1 applying the constants provided in Bindeman et al., (1998) and the composition of the most rimward analysis in the transect used to calculate an equilibrium liquid composition. This partitioning model was chosen over Nielsen et al., (2017) as it has significantly lower uncertainties for Sr and Mg. We then assume that this liquid composition is what the plagioclase in the measured profile would be equilibrating with. While these analyses are not always exactly at the rim of the grain, we find that calculated equilibrium liquids for each profile are broadly consistent with one another (i.e., 0.4 ± .1 wt% Mg; 157 ± 37 ppm Sr), regardless of whether or not they are at the core or rim of a given grain.

Initial model conditions

Determining the composition from which diffusion began within each profile was done by dividing the observed trace element concentration by the partition coefficient at each point in the profile. As we have no way of truly knowing the melt composition from which a given plagioclase formed, this yields an effective melt composition that the plagioclase roughly formed at, not accounting for changes in plagioclase concentration due to diffusion. To account for this, we generate a profile that represents a simplified series of discrete melt compositions in which that plagioclase formed that is based on both the height and width of peaks and troughs found within the effective melt composition profile (e.g., Mutch et al., 2021) . Using the observed An content we then generate an estimate of the initial plagioclase Sr and Mg profiles in equilibrium with this "simplified" liquid profile (Supplementary Figure 1). There are two main limitations to this approach. One is that it limits profiles that can be modeled to those that show peaks and troughs in their effective liquid composition profiles. The second is that it limits profiles to those that do not show significant signs of equilibration (i.e., they still have a positive relationship with An). This may inherently bias results towards plagioclase profiles that have not experienced much observable diffusion as those that have may have had gradients smoothed out via diffusive equilibration within the grain such that an initial profile from which diffusion began is not

discernable. We also compare this approach with a more "classical" method where we use the observed An distribution over regions where An changes rapidly to estimate a simple function distribution of Mg and Sr. While both methods produce similar results, we find that the method used in this study (i.e., Supplementary Figure 1) produces better fits to the observed data (Supplementary Figure 2) and involves fewer assumptions about melt evolution in the CGI magmatic system. More specifically, our method involves estimating a minimum amount of melt compositions from which the plagioclase grew, whereas, due to the An dependence on trace element partitioning in plagioclase (e.g., Equation 1), a step function for the initial distribution of Mg and Sr requires a complex melt chemistry evolution assumption that we do not necessarily have evidence for.

On constraining lock-up temperatures

The rate that diffusion occurs is strongly dependent on temperature. As such, temperature is an important input in all diffusion models. In the case of long-term magma storage, it is difficult to accurately assign a temperature, and storage conditions are unlikely to be isothermal in any case. We instead follow the approach of Cooper and Kent (2014) where we constrain the maximum time that a given crystal could spend at a given average temperature. This approach also allows use of diffusion timescales and the relationship between viscosity and temperature (Marsh, 1981) to constrain the maximum time that magma could spend in a state where it could be considered rheologically mobile and able to be erupted. Petrological modelling and experimental studies of silicic magmas, including monotonous intermediates, show that they experience a rapid increase in magma viscosity at crystallinities of 30-40% (e.g., Marsh, 1981, Gualda et al., 2021, Cooper and Kent, 2014, Caricchi and Blundy, 2015). For most intermediate and silicic compositions this change in crystallinity and viscosity occurs at temperatures of ~750 ± 20°C (Cooper and Kent, 2014; Bradshaw, 2017). Thus, diffusion timescales calculated at 750°C provide estimates of the maximum total time that a given crystal has resided in magma with a viscosity that allows it to be mobilized and erupted (e.g., Cooper and Kent, 2014). We note that this approach is a simplification, and there is unlike to be a simple “one size fits all” crystallinity for eruptible magma as the viscosities of highly crystalline magmas are approximations of complex multi-phase fluid dynamics (Bergantz *et al.*, 2017, Caricchi *et al.*, 2007; Mader *et al.*, 2013; Pistone *et al.*, 2013). Viscosities are also influenced by the presence of an exsolved volatile phase (Okumura et al., 2019; Pistone et al., 2013). However, the transition

from rheologically mobile to immobile with increasing crystallinity occurs rapidly with changing temperature, and thus changes in the crystallinity between 20-70% typically occur within the 750 ± 20°C temperature range. We have also explored the influence of temperature variation within this range and show that this ± 20°C range results in diffusion timescale changes by a factor of two (Supplementary Figure 3). Finally, empirical evidence also suggests that 40-50% crystallinity represents the upper limit for eruptible magma, as the crystallinities of erupted (and therefore eruptible) volcanic rocks are rarely above 45-50% (Marsh, 1981), and the crystallinities of Cerro Galán rocks themselves are only as high as 40-50% crystals (Folkes *et al.*, 2011b).

Recently it has also been shown that some regions of a magma reservoir may be stored for significant periods of time below the solidus and erupted without prior rejuvenation or remobilization (Mucek *et al.*, 2021), and there is also evidence for re-incorporation of plutonic lithics into voluminous eruptive products (Rivera *et al.*, 2016; Andersen *et al.*, 2017). However, although such regions could preserve very different thermal conditions, these portions of the system are unlikely to be representative of the overall magma storage conditions that contribute to the bulk of the 630 km^3 of erupted material associated with the CGI, as they are volumetrically minor relative to total erupted volume (e.g., Mucek et al., 2021).

Model uncertainties

The best fit diffusion timescale to the observed trace element profile was assessed using a standard chi-squared test that assigns a 'goodness of fit' for each iteration of the model. The smallest chi-squared value for a given model is then deemed to be the best fit diffusion time based on the input parameters. Uncertainties for each diffusion model were evaluated using a Monte Carlo approach where 1000 random profiles were generated for each modeled profile. Random profiles were based on the analytical uncertainty at each analyzed point (i.e., for each point in the profile a normally distributed random number was generated based on the observed mean analysis value and its 1 sigma uncertainty). Best fit diffusion times were then fit to each random profile in the Monte Carlo simulation keeping the initial boundary conditions and temperature fixed. As we are quantifying a duration above 750°C, for reasons listed above, and not a measured temperature with an uncertainty, we keep this temperature fixed as well. Overall uncertainties for a given diffusion model were calculated by taking the mean and standard deviation for the Monte Carlo simulation. Some of the distributions from Monte Carlo simulations more accurately represented either chi or log-normal distributions, so prior to taking

the mean and standard deviation they were first transformed to fit a normal distribution. Calculated means and standard deviations from the transformed distribution were then back transformed so that they were in correct time units (e.g., years and not log[years]). All data handling, figure creation, and diffusion modeling was completed using the programming language Python (version > 3.6) via the IPython environment (Pérez and Granger, 2007) and relies heavily on the following packages: numpy (Harris *et al.*, 2020); scipy (Virtanen *et al.*, 2020); matplotlib (Hunter, 2007); pandas (McKinney, 2010); statsmodels (Seabold and Perktold, 2010); seaborn (Waskom, 2021). For a more complete explanation of the diffusion modeling process and the intricacies of the model, we have created a Jupyter notebook and associated python module that are available for download (https://github.com/jlubbersgeo/diffusion_chronometry).

Rhyolite MELTS modeling

Modeling of phase equilibria in the CGI magmatic system was completed using Rhyolite MELTS for Excel (Gualda *et al.*, 2012; Gualda and Ghiorso, 2015). Model starting compositions were used that represent a range of potential mixtures derived from local basalt and Proterozoic basement compositions as isotopic and trace element evidence suggests that many of the geochemical characteristics of large Puna ignimbrites can be explained by a starting composition that is comprised of a 50-50 mixture of these two endmembers (Kay *et al.*, 2011). Basalt compositions were taken from Kay et al., (1994) and Drew et al., (2009) and basement compositions were taken from Ortiz et al., (2019). The exact starting compositions for each model can be found in the Supplementary Data spreadsheet. Log fO_2 is constrained and tested over a range of compositions between +0 and +1.7 NNO (Folkes *et al.*, 2011b), pressures range from 100 – 200 MPa (Grocke *et al.*, 2017), and water contents range between 0 and 6 wt%.

RESULTS

Geochemistry

Whole Rock

Bulk rock major and trace element data for our samples are consistent with previous work (Folkes *et al.*, 2011b; Wright *et al.*, 2011). Pumice found within the CGI is relatively homogeneous in SiO_2 and other major elements (Figure 2A) but has been interpreted to be the result of fractional crystallization (Folkes *et al.*, 2011b). Rare earth element diagrams for the CGI

show shallow Eu anomalies and middle - heavy rare earth concentrations of 10x chondrite are consistent with other large silicic eruptions that have been interpreted to be from relatively cold, wet, and oxidizing conditions (Bachmann and Bergantz, 2008a; Deering *et al.*, 2008, 2010). Although there are some more subtle differences in Eu/Eu*, overall REE trends are similar for both pumice types Figure 2B).

Plagioclase

Plagioclase from the CGI has An values that are normally distributed around $An_{36\pm4}$. There are, however, small numbers of analyses that display $An_{>60}$ and $An_{<25}$. High An values are exclusively found in plagioclase cores. Plagioclase trace element compositions from the CGI, like An, show mostly unimodal trace element distributions and plagioclase compositions largely overlap between white and gray pumice (Figure 3). However, when plagioclase analyses are observed incorporating spatial information, we find that there are small geochemical heterogeneities on the intracrystalline scale (see section below on Ba-An distributions). Furthermore, we find that, although most plagioclase display Mg concentrations of 30-50 μg/g and have a mean composition of An_{35}, some restricted zones in plagioclase cores contain concentrations up to 200 - 400 μg/g Mg and are An_{55} or greater (Figure 4). Strontium and Mg in plagioclase from the CGI also exhibit a positive relationship with An (Figure 5 A, C). This contrasts with negative correlations between Mg, Sr and An that would result from equilibrium partitioning with a single liquid composition, or from complete diffusive equilibrium Figure 5B, D). Thus, the Sr and Mg profiles in plagioclase must lie somewhere between their initial state (the composition when that part of the mineral formed) and full diffusive equilibration. Backscattered electron images with corresponding locations of LA-ICP-MS transects for all grains analyzed can be found in Supplementary Figure 4.

DISCUSSION

Diffusion of Mg and Sr in plagioclase

As discussed above, both Sr and Mg in plagioclase appear to be out of diffusive equilibrium with their plagioclase host. This is shown by the observation that both Sr and Mg profiles are significantly different from calculated equilibrium profiles, and by the positive correlations between An - Sr and An - Mg in individual crystals and in the CGI system as a whole (Figure 5) which are antithetic to trends expected from full diffusive equilibration. The

positive correlations between Sr, Mg and An reflect petrogenetic processes during the crystallization of plagioclase whereby Sr and Mg are removed from the melt by crystallization of plagioclase and mafic phases (Cooper and Kent, 2014) as progressively lower An plagioclase forms, producing the observed positive trends.

Magnesium in plagioclase diffusion models were completed for 37 transects and best fits range in duration from 5 to 142 years (Figure 6A) with an interquartile range of between 10 and 29 years. Strontium in plagioclase diffusion models were completed for 37 transects and range in duration from 7 years to 346 years with an interquartile range of between 30 and 85. We note that 37 diffusion models is significantly less than the 81 profiles measured by LA-ICP-MS. Diffusion models were not completed for a given trace element profile if either the initial profile could not be adequately discerned (i.e., no peaks or troughs discernable in the effective melt composition) or the model did not produce a solution that resembled the observed data. In the instance where model solutions do not fit the observed data well, timescales are discarded and not considered further in our petrologic interpretations. We hypothesize that the poor fit of these models is due to inaccurate characterization of an initial profile, which ultimately leads to the model to produce diffusion profiles that significantly deviate from the observed data. A summary of diffusion model results can be found in the Supplementary Data spreadsheet and a more detailed model report for each transect modeled can be found in Supplementary Figure 5.

Representative diffusion models for Mg and Sr in plagioclase can be found in Figure 7 and illustrate: 1) Variations of both Mg and Sr, for the most part, suggest that little diffusive equilibration has occurred, as their model best fits do not resemble their corresponding equilibrium profile; 2) Sr and Mg best fit diffusion models show that all plagioclase studied do not appear to have spent more than decadal to centennial timescales above 750°C. This is also consistent with the positive relationship observed between Sr, Mg and An. We find that there is no correlation between diffusion time and where on the grain the transect was measured (i.e., core, middle, rim). This, however, may also be due to the relatively large uncertainties in our timescale estimates.

There also appears to some systematic differences in the timescales recorded using Mg and Sr. Although the timescales estimated at 750°C for Sr and Mg overlap to a large degree (Figure 6A), we performed a two-sample Kolmogorov-Smirnov (KS) test which tests the null hypothesis that two samples are drawn from the same distribution. We find that Mg and Sr

timescale distributions are significantly different (i.e., the probability they are drawn from distributions is << .05), and in grains where Sr and Mg diffusion models were completed for the same transect (n = 23 out of 37) there appears to be a consistent difference in best fit diffusion, with Sr recording longer times by a factor or 2-4. In most cases this difference is outside our estimated uncertainty (Figure 6B). Overall, only 10 out of 23 transects in which both Sr and Mg diffusion models have been completed have times that overlap within 95% confidence limits (Figure 6B).

One explanation for the differences between Sr and Mg diffusion models might be differences in the petrologically-controlled variations of Sr and Mg that occurs with changes in An content during plagioclase formation, in ways that impacts our ability to develop reasonable initial distributions of these elements. In addition, there could be systematic variations in the estimates of diffusivity and how diffusivity varies with An content for both elements. Both Sr and Mg have different partitioning sensitivities to An content in plagioclase (i.e., the "A" parameter in Equation 1) which is not only used to calculate equilibrium profiles, but also incorporated into how the initial profile is chosen (e.g., calculating an effective liquid composition from which step functions are created), and determines how diffusion progresses (e.g., Equation 2). Therefore, uncertainties in this value could cause a decoupling of diffusion model times.

A second explanation is that there are also differences in the sensitivity of each element's diffusion model to the shape of the initial profile. Elements that have large discrepancies in diffusion rates should produce noticeably different diffusion widths after a sufficiently long period of time (Morgan and Blake, 2006). Conversely, when their diffusion widths and magnitudes appear similar, they will yield different diffusion times reflecting their individual diffusion rates, subsequently leading to the interpretation that diffusion has not progressed significantly from initial boundary conditions (Till *et al.*, 2015; Shamloo and Till, 2019). While CaAl – NaSi diffuses so slowly (e.g., Cherniak, 2010) that it is not useful in quantifying timescales of volcanic processes, we apply similar logic as Till et al. (2015) inasmuch as Mg profiles in the CGI plagioclase, using the Bindeman et al. (1998) partitioning model, simply could not have existed for $>10^3$ years at 750°C while still resembling the observed An profile more than equilibrium profile shapes and maintaining a positive correlation with An (Figure 8). While an overall diffusion width in this instance is challenging to accurately assess as models do

not start from smooth step functions, the observation that Sr and Mg profiles for the same grain are similar distances from their calculated initial profile (e.g., Figure 7) means that their diffusion times should be different proportionate to their difference in diffusion coefficient (e.g., ~ a factor of five at our observed An values). In this instance, the faster diffusion of Mg means that overestimation of the diffusion times is likely to be smaller with incorrect boundary conditions, and thus Mg diffusion models are likely to more accurately represent the duration at which that profile existed at or above 750°C.

Our best fit diffusion timescales at this temperature for both Mg and Sr in plagioclase are interpreted to represent the maximum total amount of time that an individual grain, or portion of a grain, and the local magma in thermal contact with this crystal, could have spent at magma reservoir conditions sufficient for the magma to be mobile. In addition, each grain is recording its own individual thermal history, and as diffusion is continuous from the moment a given chemical potential (i.e., zone boundary) within the mineral forms, the calculated timescale provides a "thermal budget" for all the processes that might impact the thermal state of the crystal. This includes initial crystal growth – which can occur over a wide range of temperatures in the Cerro Galán magmatic system (Bradshaw, 2017), including temperatures over 750°C, as well as long term storage, and transient reheating events associated with magma recharge and eventual eruption (e.g., Rubin et al., 2017).

Despite this potential complexity, our results collectively indicate that the population of CGI plagioclase we have examined have only spent decades to centuries at temperatures required to maintain eruptible magma. Moreover, we see broadly unimodal timescale distributions (Figure 6A) which suggests that although plagioclase populations may have different chemical histories (see "Plagioclase as a recorder of magma reservoir conditions" section below) they do not appear to have not experienced systematically different thermal histories. This may be due to the relatively high uncertainties in our diffusion timescale estimates, but also may reflect that diffusion of heat in silicic magmas is relatively rapid (e.g., Jaeger, 1964; Romine et al., 2012) relative to most chemical constituents via diffusion, allowing the reservoir to respond to heterogeneities in temperature faster than those in composition (e.g., Holycross and Watson, 2018).

Plagioclase as a recorder of magma reservoir conditions

Plagioclase can be also used to infer long-term magma reservoir thermochemical histories using a combination of trace element partitioning and diffusion chronometry. Plagioclase crystallizes over a wide range of temperatures in the CGI magma system (Supplementary Figure 6), suggesting that it should reflect crystallization from a melt that is becoming more progressively depleted with elements such as Sr that are compatible in plagioclase (Bindeman *et al.*, 1998; Nielsen *et al.*, 2017) or compatible in phases that are co-crystallizing with plagioclase (e.g., Ba in biotite and sanidine, Mg in biotite). Using partition coefficients from Bindeman et al., (1998) and our measured plagioclase compositions we have calculated melt compositions in equilibrium with observed plagioclase compositions and compared these to the erupted pumice glass compositions similar to how effective liquid compositions are generated in our diffusion models (Figure 9). We find that for Sr and Ba, many plagioclase equilibrium liquid compositions overlap with observed glass data, however observed Mg glass compositions are significantly lower than plagioclase equilibrium liquids. While a decrease in crystallization temperature to values that reflect a typical granitic solidus (e.g., ~650-680) shifts plagioclase equilibrium melt compositions to lower Mg abundances, even at these lower temperatures most calculated equilibrium and observed glass compositions for Mg do not overlap. As biotite is the only phase within the CGI in which Mg is a major component (Folkes *et al.*, 2011b), we take this observation to imply that the majority of CGI plagioclase crystallized from a magma that had substantially less biotite than what is observed in erupted pumice. However, this magma was not completely devoid of biotite as its co-crystallization with plagioclase is the only feasible way in which Sr, Mg, and Ba are all decreasing in the melt as fractionation of the CGI mineral assemblage occurs (e.g., Deering et al., 2011; Sliwinski et al., 2015). MELTS modeling predicts that biotite crystallization is neither solely an early nor late-stage phase (Supplementary Figure 6), so using its co-crystallization with plagioclase to delineate whether plagioclase has experienced long-term storage within the magmatic system is limited in this regard. Instead, we propose that the wide array (i.e., Figure 9; Ba concentrations ranging from ~1000 ppm to ~50 ppm) of melt compositions in equilibrium with observed plagioclase are, themselves, evidence for longer-term storage and the result of plagioclase crystallization from magma reservoir conditions that do not reflect those immediately prior to

493 eruption, but longer-term magma storage that is evolving due to fractionation of (predominantly)
494 plagioclase and biotite.
495 Another likely explanation for the wide array of plagioclase equilibrium liquid
496 compositions may be that some of the plagioclase studied here are antecrysts included from
497 previous magmatic activity at Cerro Galan caldera (e.g., systems responsible for producing the
498 Cueva Negra or Toconquis group ignimbrites) or at least contain cores that are inherited from
499 previous magmatic systems. This hypothesis is difficult for us to assess further, as there is very
500 little published information on the crystal cargo from these magmatic systems. While we find it
501 unlikely that all plagioclase sampled are antecrysts, transects with high An values (i.e., greater
502 than ~60) only found in the cores of some plagioclase observed (e.g., Figure 4) also correspond
503 with "outliers" in Figure 9 and with their plagioclase equilibrium liquids recording Mg values
504 orders of magnitude above most analyses, suggesting that they are inherited from a magmatic
505 system that is much less evolved than the CGI magmatic system. It should be noted that the
506 presence of antecrysts does not change our conclusions about the duration of storage of magma
507 at eruptible conditions as although antecrysts may have a more extended magmatic history, they
508 must still experience the same set of thermal conditions prior to eruption as autocrystic
509 plagioclase in the erupted CGI magma.
510 Incorporating a spatial component and expanding on Figure 9 provides insight into the
511 relative stage of magmatic development each transect is recording. As previously mentioned,
512 fractionation of biotite and sanidine will drive changes in Ba in the melt. Barium also diffuses
513 sufficiently slowly in plagioclase (Cherniak, 2002) that measured Ba contents will not be
514 significantly modified by diffusion, meaning equilibrium melt compositions calculated from
515 them should accurately record the composition of the melt when that portion of the crystal
516 formed. Looking at the relationship between these equilibrium melt compositions and An in a
517 single grain thus allows us to determine: 1) whether or not biotite or sanidine were present as that
518 portion of the plagioclase was growing, as a decrease in Ba with mineral growth implies a co-
519 crystallization with a Ba compatible phase and 2) the relative stage of magmatic development as
520 high concentrations of Ba in the equilibrium liquid imply crystallization from a melt that has not
521 experienced significant biotite or sanidine fractionation (e.g., van Zalinge et al., 2017).
522 Observed Ba-An relationships in plagioclase reveal a diversity of behavior (Figure 10)
523 and we classify this diversity into three broad stages. The first (i.e., Figure 10A; "evolved stage")

is characterized by transects that record low (e.g., 50-100 ppm) overall Ba equilibrium liquid concentrations which show evidence for recharge by having overall increases in An as the transect progresses towards the rim of the grain. Transects also frequently show evidence for potential dissolution of a Ba compatible phase with Ba equilibrium melt concentrations increasing as the transect progresses towards the rim, implying that Ba is being added to the melt. It is also possible that this may not be dissolution of a Ba compatible phase, but rather due to mass transfer from recharge, especially with most biotite in the CGI showing little textural indication of dissolution. As these transects record the lowest overall Ba concentrations, we suggest these are recording the either the later stages of magmatic development or magmatic environments that have experienced the highest degree of fractionation. The second stage (i.e., Figure10B, "main stage") is characterized by Ba equilibrium melt concentrations that represent the bulk of plagioclase analyses (e.g., 100 – 300ppm). These transects show frequent evidence for alternating between recharge and fractionation (e.g., the zig zag behavior of the Ba-An relationships in Figure 10B) and reflect a magmatic environment that we interpret to be one that is dominantly fractionating plagioclase and biotite but experiences periodic recharge that adds Ba to the melt either through dissolution of biotite or mass transfer. The third stage (i.e., Figure 10C; "long-term") is characterized by transects that have large overall Ba equilibrium melt concentrations (e.g., up to 1000 ppm) and ranges (e.g., up to 900 ppm decrease in Ba over the length of the transect), and the highest An values found within CGI plagioclase (up to An_{70}). These profiles are the minority of transects observed in our dataset (i.e., <5%) and all show signs of fractionation with a Ba compatible phase. We interpret these transects to reflect initial crystallization from a magmatic environment that is either 1) early in the CGI magmatic system's history that has not experienced significant biotite or sanidine fractionation such that Ba melt concentrations are still extremely high relative to observed erupted glass concentrations; 2) predates the CGI magmatic system (i.e., they are antecrysts); 3) is not related to magmatic activity at Cerro Galan caldera (e.g., they are scavenged from the surrounding wall-rock).

These observations reveal that individual plagioclase crystals are not only recording different crystallization environments, but also have the potential to record multiple crystallization/dissolution events (e.g., prior to their evacuation from the reservoir(s) in which they grew). This is also in contrast to the bulk rock major and trace element chemistry for the CGI which suggest a more chemically homogeneous system (Folkes *et al.*, 2011b). To determine

555 if there are statistically significant differences recorded in diffusion timescales between these
556 groups, we again performed a two-sample KS test. In this case our samples consisted of
557 plagioclase that show signs of co-crystallization with biotite/sanidine and plagioclase that do not.
558 We find that despite plagioclase recording very different chemical environments, there is no
559 statistically significant difference in diffusion timescales between groups (the probability they
560 are drawn from distributions is >> .05). These results hold for both Mg and Sr diffusion results.
561 Collectively these data are interpreted to show that although individual plagioclase experienced
562 and recorded quite different petrologic environments, there are no substantive differences
563 recorded in thermal history between these crystals.

564 **Periodic recharge**

565 Plagioclase from the CGI exhibit mean An values of An_{35}, however display frequent
566 $An_{>55}$ zones throughout many analyzed grains (Figure 4; Figure 10; Supplementary Figure 5). An
567 increase in An of this magnitude may be due to increases in temperature or pressure (Streck,
568 2008) or rapid ascent of water saturated magmas (Blundy *et al.*, 2006); however, we propose that
569 this increase in An is due to recharge of a less evolved magma, as increases in An are typically
570 not found at the rims of a given grain. Furthermore, these high An zones are also associated with
571 significantly higher concentrations of Mg (Figure 4; Figure 9) and Ba (e.g., Figure 9; Figure10)
572 which may also be further support for influence from a less evolved magma. These observations
573 also effectively rule out rapid ascent of water saturated magmas as a likely cause of high An
574 zones, as rapid ascent driven changes in An would also likely be one of the last events a
575 plagioclase records prior to eruption and be found at the rims of grains or as infilled sieved
576 textures, neither of which are observed.

577 Our diffusion timescales for Mg and Sr also put thermal and temporal limits on these
578 recharge events, as our data provide an estimate of the total time that a crystal could have been at
579 temperatures in excess of 750°C. As noted above, our calculated diffusion times define a *thermal*
580 *"budget"*; the total time a crystal spends above 750°C that includes the formation, storage, and
581 eruption of individual crystals. This logic applies regardless of the origin of the plagioclase (i.e.,
582 whether it is an antecryst or xenocryst). The relatively short durations we estimate for residence
583 at temperatures ≥ 750°C, imply that, although recharge events clearly occur and contribute to
584 chemical changes in the system, they did not increase the temperature of the CGI magma system
585 for significant periods of time.

586 Our data also show that grains that experience recharge occur throughout the magmatic
587 history of the CGI system (i.e., profiles that belong to both "evolved stage" and "main stage"
588 categories listed above). We take the ubiquity of high-An zones in both groups of plagioclase to
589 imply that the Cerro Galán magmatic system has been periodically recharged with a magma that
590 produces plagioclase of at least An_{55} and potentially as high as An_{70} compositions. This idea is
591 also supported by previous research that shows: 1) the presence of a volumetrically minor, less
592 evolved, pumice population (i.e., gray pumice) that Wright et al. (2011) used to suggest that
593 there was a second, less evolved but still silicic melt reservoir deeper in the crust that briefly
594 interacted with CGI magmas prior to eruption; 2) volatile zoning in apatite indicating recharge
595 shortly before eruption by a volatile-rich magma into a reservoir that contained local variations
596 in composition (Boyce and Hervig, 2008).

597 **Long term thermochemical conditions during crustal magma storage**

598 The results from our plagioclase trace element and diffusion modeling show that the
599 plagioclase measured in this study are recording a range of magma reservoir chemical
600 environments within the Cerro Galán magmatic system, and that overall, magmas stored at
601 thermal conditions where they are eruptible are only present for periods of decades to centuries
602 or less, regardless of whether or not plagioclase show signs of long-term residence (i.e., in
603 equilibrium with high Ba and Mg melts) or later-stage crystallization (i.e., in equilibrium with
604 melts that are depleted in Ba from fractionation of biotite and sanidine). This is important as it
605 implies that short diffusion times are not simply reflective of young crystals, and that the long-
606 term thermal history of the CGI magmatic system was one was dominated by storage
607 temperatures below 750°C. Below, we address how these timescales fit with previous literature
608 on magma remobilization timescales and what it means for the long-term thermochemical state
609 of the magma system.

610 Previously, the Cerro Galán magmatic system has been classified as homogeneous on the
611 basis of bulk rock and major phase chemistry (Folkes *et al.*, 2011b). Whereas homogeneity of a
612 given system is ultimately defined by the scale of investigation (Bachmann *et al.*, 2002), the CGI
613 is homogenous inasmuch as it does not display bulk rock major element zoning characteristic of
614 many large silicic eruptions (e.g., Bachmann et al., 2014; Chesner and Rose, 1991; Szymanowski
615 et al., 2019). The CGI, however, also has been interpreted as the result of assimilation-
616 fractionation from an initial composition that is a 50-50 mix of local metamorphic basement and

mantle derived basalts (Folkes *et al.*, 2011b; Kay *et al.*, 2011), suggesting that there may have been large scale thermochemical zoning related to progressive differentiation at some point in its history (Bachmann and Bergantz, 2008b). Huber et al., (2012) find that these reservoir scale heterogeneities may be removed in crystal-rich, eutectoid systems with high degrees of exsolved volatiles on the order of years or less, which is significantly shorter than the time required to reactivate a given mush body via repeated injection of hotter magmas (Hartung *et al.*, 2019). Based on heterogeneous crystal cargo that display frequent zoning (Figure 4; Figure 7; Supplementary Figure 4), evidence for long term storage with repeated recharge of less evolved, volatile rich material (Boyce and Hervig, 2008; Wright *et al.*, 2011), and short times at remobilizing temperatures (Figure 6), we argue it is highly plausible then, that the Cerro Galán magma system was in a chemically heterogeneous but uneruptible state for a significant portion of its history and was only homogenized and remobilized shortly before eruption similar to other voluminous crystal-rich dacitic eruptions (e.g., Fish Canyon Tuff; Charlier *et al.*, 2007).

CONCLUSION

We applied diffusion modeling of Mg and Sr in plagioclase from the 2.08 Ma, 630 km^3, Cerro Galán Ignimbrite (CGI) to investigate the long-term thermochemical magma storage conditions of large silicic magma reservoirs. Our results indicate that, although bulk-rock geochemistry implies a magmatic system that is chemically homogeneous at the time of eruption, plagioclase are recording diverse crystallization environments (i.e., co-crystallization with Ba-compatible phases such as biotite and sanidine as well as crystallization without Ba-compatible phases) throughout their crystallization history that largely do not reflect those at the time of eruption. Furthermore, despite this evidence for long-term storage within the reservoir, CGI plagioclase are only recording timescales of decades to centuries at temperatures required to maintain eruptible volumes of magma. We interpret these results to reflect that the CGI magmatic system existed in a predominantly immobile, but chemically heterogeneous state for most of its residence within the crust. These results help to further constrain the long-term thermochemical storage conditions of magma systems capable of producing catastrophic caldera forming eruptions.

ACKNOWLEDGEMENTS

We would like to thank Cristian Metzke and Agustín Ortiz for their help in the field, Frank Tepley and Marie Takach for their assistance with gathering EPMA data, Chris Russo for his help with LA-ICP-MS work, Sumit Chakraborty and Tyler Schlieder for conversations and advice on the intricacies of plagioclase diffusion modeling, the OSU VIPER group for their support throughout the duration of this experiment, and the open-source coding community for providing the tools necessary to complete this work. We also thank Dan Morgan, Smruti Sourav Rout, and one anonymous reviewer for their constructive feedback on earlier versions of this manuscript. This work was supported by NSF grants EAR1948862 and EAR1763639 to AJRK.

DATA AVAILABILITY

All data underlying this article are available in its online supplementary material. Diffusion modeling code can be accessed in the following GitHub repository: https://github.com/jlubbersgeo/diffusion_chronometry.

REFERENCES

Andersen, N. L., Jicha, B. R., Singer, B. S. & Hildreth, W. (2017). Incremental heating of Bishop Tuff sanidine reveals preeruptive radiogenic Ar and rapid remobilization from cold storage. **114**, 12407–12412.

Annen, C., Blundy, J. D., Leuthold, J. & Sparks, R. S. J. (2015). Construction and evolution of igneous bodies: Towards an integrated perspective of crustal magmatism. *Lithos*. Elsevier B.V. **230**, 206–221.

Annen, C., Blundy, J. D. & Sparks, R. S. J. (2006). The genesis of intermediate and silicic magmas in deep crustal hot zones. *Journal of Petrology* **47**, 505–539.

Bachmann, O. & Bergantz, G. W. (2008a). Rhyolites and their source mushes across tectonic settings. *Journal of Petrology* **49**, 2277–2285.

Bachmann, O. & Bergantz, G. W. (2008b). Deciphering Magma Chamber Dynamics from Styles of Compositional Zoning in Large Silicic Ash Flow Sheets. *Reviews in Mineralogy and Geochemistry* **69**, 651–674.

Bachmann, O., Deering, C. D., Lipman, P. W. & Plummer, C. (2014). Building zoned ignimbrites by recycling silicic cumulates: insight from the 1,000 km3 Carpenter Ridge Tuff, CO. *Contributions to Mineralogy and Petrology* **167**, 1025.

Bachmann, O., Dungan, M. A. & Lipman, P. W. (2002). The Fish Canyon Magma Body , San Juan Volcanic Field , Colorado : Rejuvenation and Eruption of an Upper-Crustal Batholith. **43**, 1469–1503.

Barboni, M., Boehnke, P., Schmitt, A. K., Harrison, T. M., Shane, P., Bouvier, A.-S. & Baumgartner, L. (2016). Warm storage for arc magmas. *Proceedings of the National Academy of Sciences* **113**, 13959–13964.

Bindeman, I. N., Davis, A. M. & Drake, M. J. (1998). Ion microprobe study of plagioclase- basalt partition experiments at natural concentration levels of trace elements. *Geochimica et Cosmochimica Acta* **62**, 1175–1193.

Blundy, J., Cashman, K. & Humphreys, M. (2006). Magma heating by decompression-driven crystallization beneath andesite volcanoes. *Nature* **443**, 76–80.

Boyce, J. W. & Hervig, R. L. (2008). Magmatic degassing histories from apatite volatile stratigraphy. *Geology* **36**, 63–66.

Bradshaw, R. W. (2017). Crystal Records of the Origin, Evolution, and Thermal Histories of Magmas. Oregon State University.

Chamberlain, K. J., Morgan, D. J. & Wilson, C. J. N. (2014). Timescales of mixing and mobilisation in the Bishop Tuff magma body : perspectives from diffusion chronometry. *Contributions to Mineralogy and Petrology*.

690 Charlier, B. L. A., Bachmann, O., Davidson, J. P., Dungan, M. A. & Morgan, D. J. (2007). The upper crustal
691 evolution of a large silicic magma body: Evidence from crystal-scale Rb - Sr isotopic heterogeneities in the
692 fish canyon magmatic system, Colorado. *Journal of Petrology* **48**, 1875–1894.
693 Cherniak, D. J. (2002). Ba diffusion in feldspar. *Geochimica et Cosmochimica Acta* **66**, 1641–1650.
694 Cherniak, D. J. (2010). Cation diffusion in feldspars. *Reviews in Mineralogy and Geochemistry* **72**, 691–733.
695 Cherniak, D. J. & Watson, E. B. (1994). A study of strontium diffusion in plagioclase using Rutherford
696 backscattering spectroscopy. *Geochimica et Cosmochimica Acta* **58**, 5179–5190.
697 Chesner, C. & Rose, Wi. (1991). Stratigraphy of the Toba Tuffs and the evolution of the Toba Caldera Complex,
698 Sumatra, Indonesia. *Bulletin of Volcanology* **53**, 343–356.
699 Cooper, K. M. & Kent, A. J. R. (2014). Rapid remobilization of magmatic crystals kept in cold storage. *Nature*.
700 Nature Publishing Group **506**, 480–3.
701 Costa, F., Chakraborty, S. & Dohmen, R. (2003). Diffusion coupling between major and trace elements and a model
702 for the calculation of magma chamber residence times using plagioclase. *Geochimica et Cosmochimica Acta*
703 **67**, 2189–2200.
704 Costa, F., Dohmen, R. & Chakraborty, S. (2008). Time Scales of Magmatic Processes from Modeling the Zoning
705 Patterns of Crystals. *Reviews in Mineralogy and Geochemistry* **69**, 545–594.
706 Couperthwaite, F. K., Thordarson, T., Morgan, D. J., Harvey, J. & Wilson, M. (2020). Diffusion Timescales of
707 Magmatic Processes in the Moinui Lava Eruption at Mauna Loa, Hawai`i, as Inferred from Bimodal Olivine
708 Populations. *Journal of Petrology* **61**.
709 de Silva, S. L. & Gregg, P. M. (2014). Thermomechanical feedbacks in magmatic systems: Implications for growth,
710 longevity, and evolution of large caldera-forming magma reservoirs and their supereruptions. *Journal of*
711 *Volcanology and Geothermal Research*. Elsevier B.V. **282**, 77–91.
712 Deering, C. D., Bachmann, O. & Vogel, T. A. (2011). The Ammonia Tanks Tuff: Erupting a melt-rich rhyolite cap
713 and its remobilized crystal cumulate. *Earth and Planetary Science Letters* **310**, 518–525.
714 Deering, C. D., Cole, J. W. & Vogel, T. A. (2008). A rhyolite compositional continuum governed by lower crustal
715 source conditions in the taupo volcanic zone, New Zealand. *Journal of Petrology* **49**, 2245–2276.
716 Deering, C. D., Gravley, D. M., Vogel, T. A., Cole, J. W. & Leonard, G. S. (2010). Origins of cold-wet-oxidizing to
717 hot-dry-reducing rhyolite magma cycles and distribution in the Taupo Volcanic Zone, New Zealand.
718 *Contributions to Mineralogy and Petrology* **160**, 609–629.
719 Degruyter, W. & Huber, C. (2014). A model for eruption frequency of upper crustal silicic magma chambers. *Earth*
720 *and Planetary Science Letters* **403**, 117–130.
721 Dohmen, R. & Blundy, J. (2014). A PREDICTIVE THERMODYNAMIC MODEL FOR ELEMENT
722 PARTITIONING BETWEEN PLAGIOCLASE AND MELT AS A FUNCTION OF PRESSURE ,
723 TEMPERATURE AND COMPOSITION. **314**, 1319–1372.
724 Drew, S. T., Ducea, M. N. & Schoenbohm, L. M. (2009). Mafic volcanism on the Puna Plateau, NW Argentina:
725 Implications for lithospheric composition and evolution with an emphasis on lithospheric foundering.
726 *Lithosphere*. Geological Society of America **1**, 305–318.
727 Folkes, C. B., De Silva, S. L., Schmitt, A. K. & Cas, R. A. F. (2011a). A reconnaissance of U-Pb zircon ages in the
728 Cerro Galán system, NW Argentina: Prolonged magma residence, crystal recycling, and crustal assimilation.
729 *Journal of Volcanology and Geothermal Research* **206**, 136–147.
730 Folkes, C. B., de Silva, S. L., Wright, H. M. & Cas, R. A. F. (2011b). Geochemical homogeneity of a long-lived,
731 large silicic system; evidence from the Cerro Galán caldera, NW Argentina. *Bulletin of Volcanology* **73**, 1455–
732 1486.
733 Folkes, C. B., Wright, H. M., Cas, R. A. F., de Silva, S. L., Lesti, C. & Viramonte, J. G. (2011c). A re-appraisal of
734 the stratigraphy and volcanology of the Cerro Galán volcanic system, NW Argentina. *Bulletin of Volcanology*
735 **73**, 1427–1454.
736 Gelman, S. E., Gutiérrez, F. J. & Bachmann, O. (2013). On the longevity of large upper crustal silicic magma
737 reservoirs. *Geology* **41**.
738 Giletti, B. J. & Casserly, J. E. D. (1994). Strontium diffusion kinetics in plagioclase feldspars. *Geochimica et*
739 *Cosmochimica Acta* **58**, 3785–3793.
740 Grocke, S. B., Andrews, B. J. & de Silva, S. L. (2017). Experimental and petrological constraints on long-term
741 magma dynamics and post-climactic eruptions at the Cerro Galán caldera system, NW Argentina. *Journal of*
742 *Volcanology and Geothermal Research*. Elsevier B.V. **347**, 296–311.
743 Gualda, G. A. R. & Ghiorso, M. S. (2015). MELTS-Excel: A Microsoft Excel-based MELTS interface for research
744 and teaching of magma properties and evolution. *Geochemistry, Geophysics, Geosystems* **16**, 315–324.

Gualda, G. A. R., Ghiorso, M. S., Lemons, R. V. & Carley, T. L. (2012). Rhyolite-MELTS: A modified calibration of MELTS optimized for silica-rich, fluid-bearing magmatic systems. *Journal of Petrology* **53**, 875–890.

Harris, C. R. *et al.* (2020). Array Programming with NumPy. *Nature*. Springer US **585**, 357–362.

Hartung, E., Weber, G. & Caricchi, L. (2019). The role of H2O on the extraction of melt from crystallising magmas. *Earth and Planetary Science Letters*. Elsevier B.V. **508**, 85–96.

Hildreth, W. (1981). Gradients in Silicic Magma Chambers Implications for Lithospheric Magmatism. *Journal of Geophysical Research* **86**, 10153–10192.

Holycross, M. E. & Watson, E. B. (2018). Trace element diffusion and kinetic fractionation in wet rhyolitic melt. *Geochimica et Cosmochimica Acta*. Elsevier Ltd **232**, 14–29.

Huber, C., Bachmann, O. & Dufek, J. (2012). Crystal-poor versus crystal-rich ignimbrites: A competition between stirring and reactivation. *Geology* **40**, 115–118.

Huber, C., Townsend, M., Degruyter, W. & Bachmann, O. (2019). Optimal depth of subvolcanic magma chamber growth controlled by volatiles and crust rheology. *Nature Geoscience*. Springer US **12**, 762–768.

Hunter, J. D. (2007). Matplotlib: A 2D Graphics Environment. *Computing in Science and Engineering* **9**, 90–95.

Jaeger, J. C. (1964). Thermal Effects of Intrusions. *Reviews of Geophysics* **2**.

Jellinek, A. M. & DePaolo, D. J. (2003). A model for the origin of large silicic magma chambers: Precursors of caldera-forming eruptions. *Bulletin of Volcanology* **65**, 363–381.

Johnson, D. M., Hooper, P. R. & Conrey, R. M. (1999). XRF Analysis of Rocks and Minerals for Major and Trace Elements on a Single Low Dilution Li-tetraborate Fused Bead. *Advances in X-ray Analysis* **41**, 843–867.

Kaiser, J. F., de Silva, S., Schmitt, A. K., Economos, R. & Sunagua, M. (2017). Million-year melt–presence in monotonous intermediate magma for a volcanic–plutonic assemblage in the Central Andes: Contrasting histories of crystal-rich and crystal-poor super-sized silicic magmas. *Earth and Planetary Science Letters*. Elsevier B.V. **457**, 73–86.

Karakas, O., Degruyter, W., Bachmann, O. & Dufek, J. (2017). Lifetime and size of shallow magma bodies controlled by crustal-scale magmatism. *Nature Geoscience* **10**, 446–450.

Kay, S. M., Coira, B. & Viramonte, J. (1994). Young mafic back arc volcanic rocks as indicators of continental lithospheric delamination beneath the Argentine Puna Plateau, central Andes. *Journal of Geophysical Research* **99**.

Kay, S. M., Coira, B., Wörner, G., Kay, R. W. & Singer, B. S. (2011). Geochemical, isotopic and single crystal 40Ar/39Ar age constraints on the evolution of the Cerro Galán ignimbrites. *Bulletin of Volcanology* **73**, 1487–1511.

Kent, A. J. R., Rowe, M. C., Thornber, C. R. & Pallister, J. S. (2008). Trace element and Pb isotope composition of plagioclase from dome samples from the 2004-2005 eruption of Mount St. Helens, Washington. *US Geological Survey Professional Paper* 809–826.

Kent, A. J. R. & Ungerer, C. A. (2006). Analysis of light lithophile elements (Li, Be, B) by laser ablation ICP-MS: Comparison between magnetic sector and quadrupole ICP-MS. *American Mineralogist* **91**, 1401–1411.

Klemetti, E. W., Deering, C. D., Cooper, K. M. & Roeske, S. M. (2011). Magmatic perturbations in the Okataina Volcanic Complex, New Zealand at thousand-year timescales recorded in single zircon crystals. *Earth and Planetary Science Letters*. Elsevier B.V. **305**, 185–194.

Knaack, C., Cornelius, S. & Hooper, P. (1994). *Trace element analyses of rocks and minerals by ICP-MS.* .

LaTourrette, T. & Wasserburg, G. J. (1998). Mg diffusion in anorthite: implications for the formation of early solar system planetesimals. *Earth and Planetary Science Letters* **158**, 91–108.

Laumonier, M., Karakas, O., Bachmann, O., Gaillard, F., Lukács, R., Seghedi, I., Menand, T. & Harangi, S. (2019). Evidence for a persistent magma reservoir with large melt content beneath an apparently extinct volcano. *Earth and Planetary Science Letters*. Elsevier B.V. **521**, 79–90.

Longerich, H. P., Jackson, S. E. & Günther, D. (1996). Laser ablation inductively coupled plasma mass spectrometric transient signal data acquisition and analyte concentration calculation. *Journal of Analytical Atomic Spectrometry* **11**, 899–904.

Lubbers, J., Kent, A. & Russo, C. (2021). LaserTRAM-DB: A Time Resolved Analysis Module for the complete reduction of Laser Ablation Inductively Coupled Plasma Mass Spectrometry data. *Earth ArXiv*.

Lundstrom, C. C. & Glazner, A. F. (2016). Silicic magmatism and the volcanic-plutonic connection. *Elements* **12**.

Marsh, B. D. (1981). On the crystallinity, probability of occurrence, and rheology of lava and magma. *Contributions to Mineralogy and Petrology* **78**, 85–98.

Mason, B. G., Pyle, D. M. & Oppenheimer, C. (2004). The size and frequency of the largest explosive eruptions on Earth. *Bulletin of Volcanology* **66**, 735–748.

McKinney, W. (2010). Data Structures for Statistical Computing in Python. *Proceedings of the 9th Python in Science Conference* **1**, 56–61.

Morgan, D. J. & Blake, S. (2006). Magmatic residence times of zoned phenocrysts: Introduction and application of the binary element diffusion modelling (BEDM) technique. *Contributions to Mineralogy and Petrology* **151**, 58–70.

Mucek, A. E., Danišík, M., de Silva, S. L., Miggins, D. P., Schmitt, A. K., Pratomo, I., Koppers, A. & Gillespie, J. (2021). Resurgence initiation and subsolidus eruption of cold carapace of warm magma at Toba Caldera, Sumatra. *Communications Earth & Environment* **2**.

Mutch, E. J. F., Maclennan, J., Shorttle, O., Rudge, J. F. & Neave, D. A. (2021). DFENS: Diffusion Chronometry Using Finite Elements and Nested Sampling. *Geochemistry, Geophysics, Geosystems*. Blackwell Publishing Ltd **22**.

Nielsen, R. L., Ustunisik, G., Weinsteiger, A. B., Tepley, F. J., Johnston, A. D. & Kent, A. J. R. (2017). Trace element partitioning between plagioclase and melt: An investigation of the impact of experimental and analytical procedures. *Geochemistry, Geophysics, Geosystems*. Blackwell Publishing Ltd **18**, 3359–3384.

Okumura, S., L. de Silva, S., Nakamura, M. & Sasaki, O. (2019). Caldera-forming eruptions of mushy magma modulated by feedbacks between ascent rate, gas retention/loss and bubble/crystal framework interaction. *Scientific Reports* **9**, 1–12.

Ortiz, A., Suzaño, N., Hauser, N., Becchio, R. & Nieves, A. (2019). New hints on the evolution of the Eastern Magmatic Belt, Puna Argentina. SW Gondwana margin: Zircon U-Pb ages and Hf isotopes in the Pachamama Igneous-Metamorphic Complex. *Journal of South American Earth Sciences*. Elsevier Ltd **94**.

Pérez, F. & Granger, B. E. (2007). IPython : A System for Interactive Scientific Computing. *IEEE Journals & Magazines* **9**, 21–29.

Pistone, M., Caricchi, L., Ulmer, P., Reusser, E. & Ardia, P. (2013). Rheology of volatile-bearing crystal mushes: Mobilization vs. viscous death. *Chemical Geology* **345**.

Rivera, T. A., Schmitz, M. D., Jicha, B. R. & Crowley, J. L. (2016). Zircon petrochronology and 40Ar/39Ar sanidine dates for the mesa falls tuff: Crystal-scale records of magmatic evolution and the short lifespan of a large yellowstone magma chamber. *Journal of Petrology* **57**, 1677–1704.

Romine, W. L., Whittington, A. G., Nabelek, P. I. & Hofmeister, A. M. (2012). Thermal diffusivity of rhyolitic glasses and melts: Effects of temperature, crystals and dissolved water. *Bulletin of Volcanology*. Springer Verlag **74**, 2273–2287.

Rout, S. S., Blum-Oeste, M. & Wörner, G. (2021). Long-Term Temperature Cycling in a Shallow Magma Reservoir: Insights from Sanidine Megacrysts at Taápaca Volcano, Central Andes. *Journal of Petrology*. Oxford University Press **62**.

Rubin, A. E., Cooper, K. M., Till, C. B., Kent, A. J. R., Costa, F., Bose, M., Gravley, D., Deering, C. & Cole, J. (2017). Rapid cooling and cold storage in a silicic magma reservoir recorded in Individual Crystals. *Science* **356**, 1154–1156.

Ruth, D. C. S., Costa, F., Bouvet De Maisonneuve, C., Franco, L., Cortés, J. A. & Calder, E. S. (2018). Crystal and melt inclusion timescales reveal the evolution of magma migration before eruption. *Nature Communications*. Springer US **9**.

Seabold, S. & Perktold, J. (2010). Statsmodels: Econometric and Statistical Modeling with Python. *Proceedings of the 9th Python in Science Conference*, 92–96.

Shamloo, H. I. & Till, C. B. (2019). Decadal transition from quiescence to supereruption: petrologic investigation of the Lava Creek Tuff, Yellowstone Caldera, WY. *Contributions to Mineralogy and Petrology*. Springer Berlin Heidelberg **174**, 1–18.

Shea, T., Costa, F., Krimer, D. & Hammer, J. E. (2015). Accuracy of timescales retrieved from diffusion modeling in olivine: A 3D perspective. *American Mineralogist* **100**, 2026–2042.

Sliwinski, J. T., Bachmann, O., Ellis, B. S., Dávila-Harris, P., Nelson, B. K. & Dufek, J. (2015). Eruption of shallow crystal cumulates during explosive phonolitic eruptions on Tenerife, Canary Islands. *Journal of Petrology*. Oxford University Press **56**, 2173–2194.

Streck, M. J. (2008). Mineral Textures and Zoning as Evidence for Open System Processes. *Reviews in Mineralogy and Geochemistry* **69**, 595–622.

Szymanowski, D., Ellis, B. S., Wotzlaw, J.-F. & Bachmann, O. (2019). Maturation and rejuvenation of a silicic magma reservoir: High-resolution chronology of the Kneeling Nun Tuff. *Earth and Planetary Science Letters*. Elsevier B.V. **510**, 103–115.

Szymanowski, D., Wotzlaw, J.-F., Ellis, B. S., Bachmann, O., Guillong, M. & von Quadt, A. (2017). Protracted near-solidus storage and pre-eruptive rejuvenation of large magma reservoirs. *Nature Geoscience* **10**.

Tierney, C. R., Schmitt, A. K., Lovera, O. M. & de Silva, S. L. (2016). Voluminous plutonism during volcanic quiescence revealed by thermochemical modeling of zircon. *Geology* **44**, 683–686.

Till, C. B., Vazquez, J. A. & Boyce, J. W. (2015). Months between rejuvenation and volcanic eruption at Yellowstone caldera, Wyoming. *Geology* **43**, 695–698.

Turcotte, D. & Schubert, G. (2002). *Geodynamics*. Cambridge University Press.

Van Orman, J. A., Cherniak, D. J. & Kita, N. T. (2014). Magnesium diffusion in plagioclase: Dependence on composition, and implications for thermal resetting of the 26Al-26Mg early solar system chronometer. *Earth and Planetary Science Letters*. Elsevier B.V. **385**, 79–88.

van Zalinge, M. E., Sparks, R. S. J. & Blundy, J. D. (2017). Petrogenesis of the large-volume cardones ignimbrite, Chile; development and destabilization of a complex magma-mush system. *Journal of Petrology*. Oxford University Press **58**, 1975–2006.

Virtanen, P. *et al.* (2020). SciPy 1.0: fundamental algorithms for scientific computing in Python. *Nature Methods* **17**, 261–272.

Walker, B. A., Klemetti, E. W., Grunder, A. L., Dilles, J. H., Tepley, F. J. & Giles, D. (2013). Crystal reaming during the assembly, maturation, and waning of an eleven-million-year crustal magma cycle: Thermobarometry of the Aucanquilcha Volcanic Cluster. *Contributions to Mineralogy and Petrology* **165**, 663–682.

Waskom, M. (2021). Seaborn: Statistical Data Visualization. *Journal of Open Source Software* **6**, 3021.

Wilson, C. J. N., Cooper, G. F., Chamberlain, K. J., Barker, S. J., Myers, M. L., Kemp, F. I.- & Farrell, J. (2021). No single model for supersized eruptions and their magma bodies. *Nature Reviews Earth & Environment*. Springer US.

Wright, H. M. N., Folkes, C. B., Cas, R. A. F. & Cashman, K. V. (2011). Heterogeneous pumice populations in the 2.08-Ma Cerro Galán Ignimbrite: Implications for magma recharge and ascent preceding a large-volume silicic eruption. *Bulletin of Volcanology* **73**, 1513–1533.

FIGURES

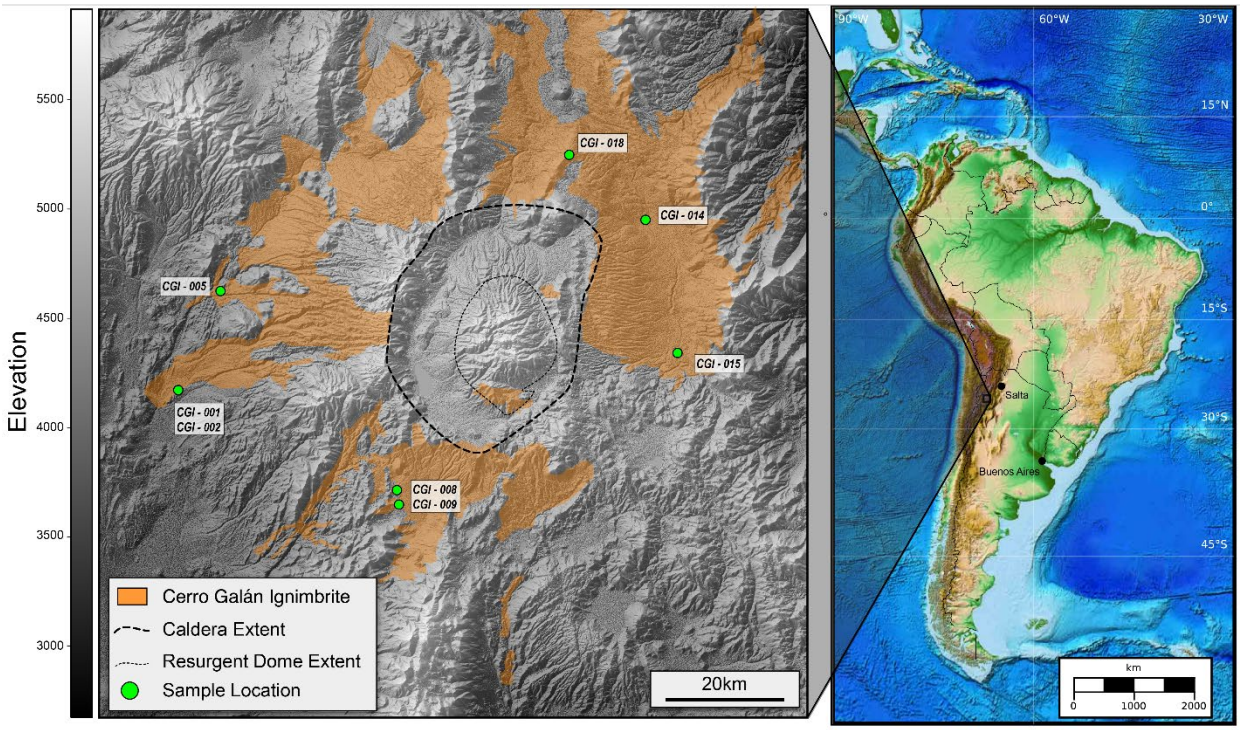

Figure 1: Digital elevation map (DEM) of the Cerro Galán Caldera and its location within the Central Andean Volcanic Zone (CAVZ). Orange shading represents the extent of the Cerro Galán Ignimbrite and green dots are sampling locations for samples used in this experiment.

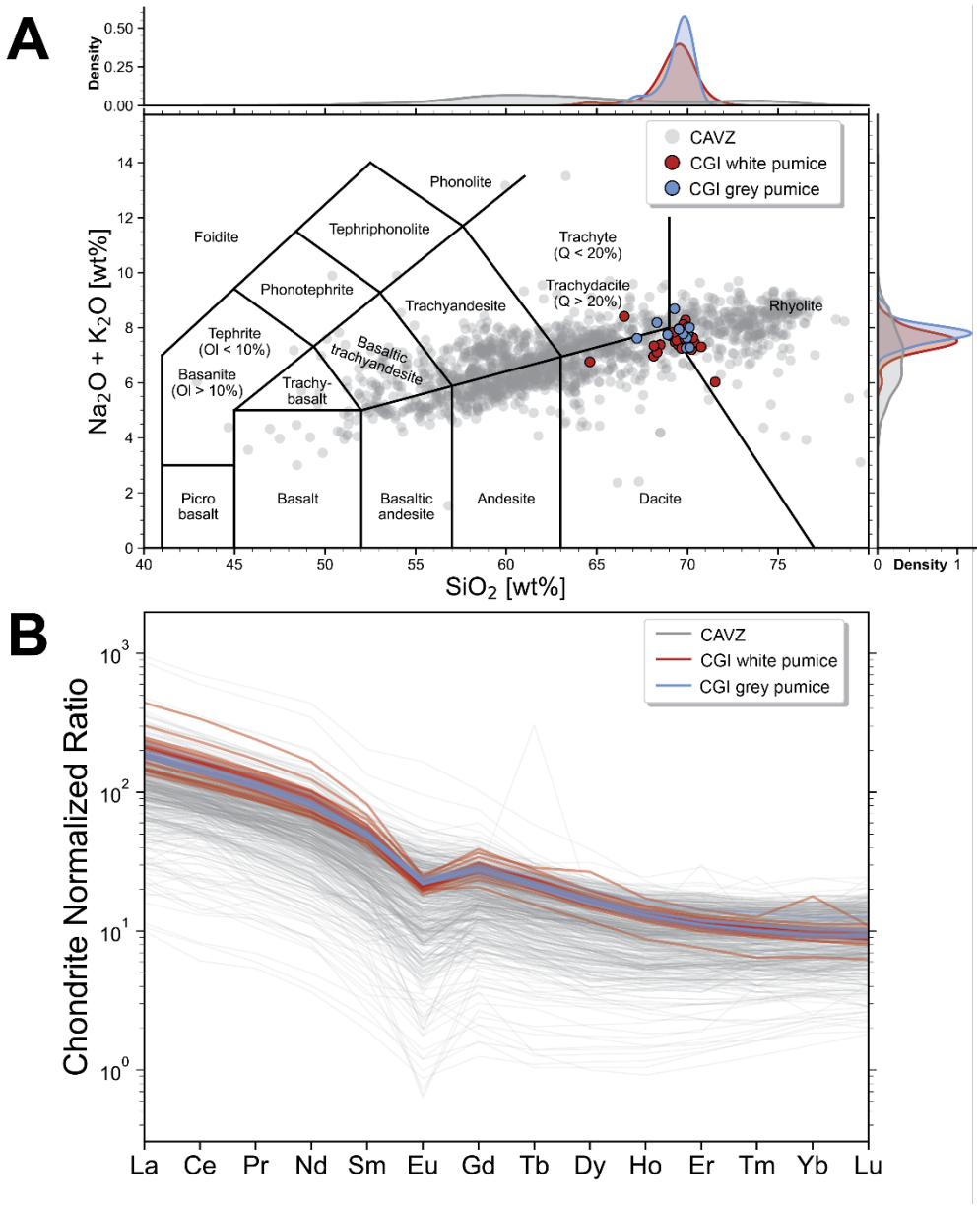

Figure 2: A) Total alkalis vs silica (TAS) diagram for CGI pumice compared to other CAVZ volcanics from the last 10Ma. Note the overlapping between the two pumice types as well as the unimodal distribution of data in both silica and total alkalis. B) REE diagram for CGI pumice (gray and white) compared to other CAVZ volcanics from the last 10 Ma. It can be seen here that CGI pumice have REE trends that are more consistent with cold, wet, oxidizing than hot, dry, reducing rhyolites from other large volcanic eruptions (Deering et al., 2010).

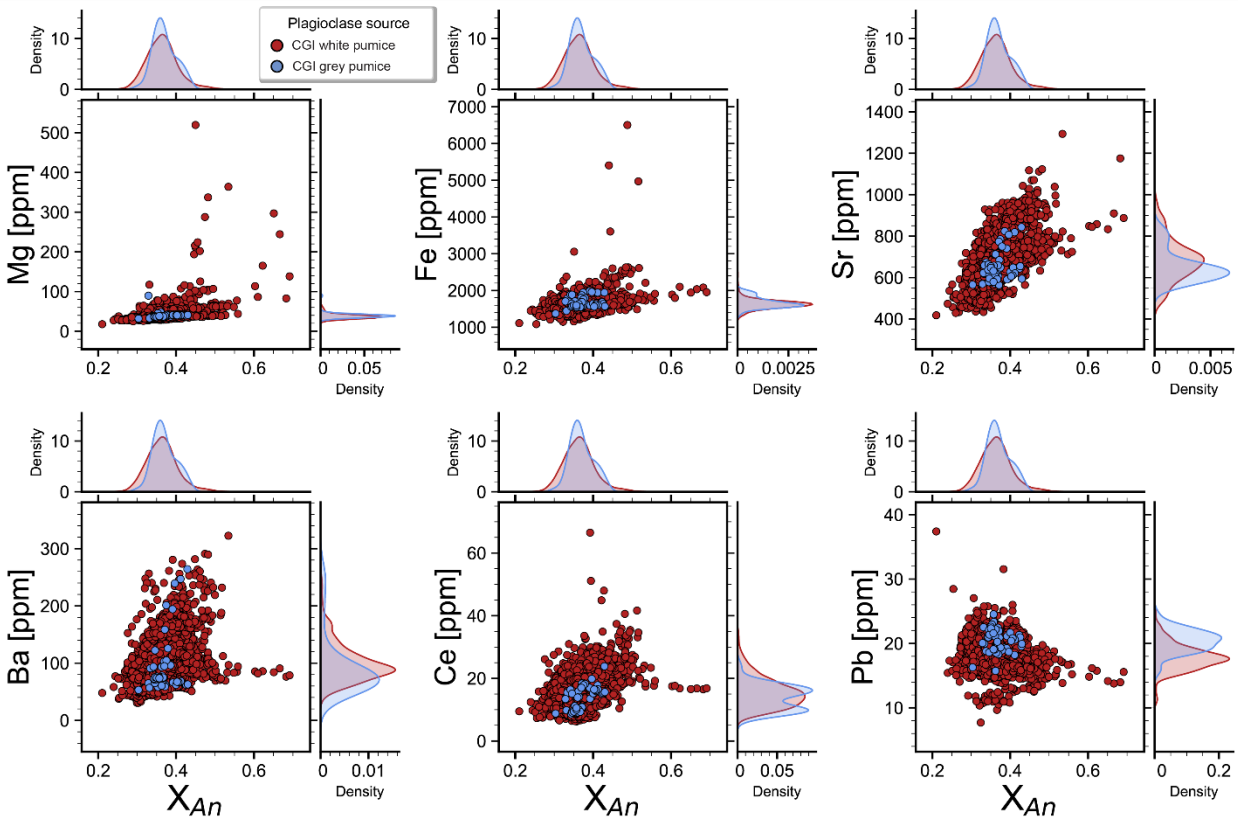

Figure 3 Panel of selected trace elements in CGI plagioclase filtered by what pumice type they are from (i.e., gray or white). Similar to bulk rock pumice data, plagioclase from the CGI overlap in composition for all trace elements measured and show unimodal distributions. Note, however, the elevated Mg concentrations found at An_{40} and above.

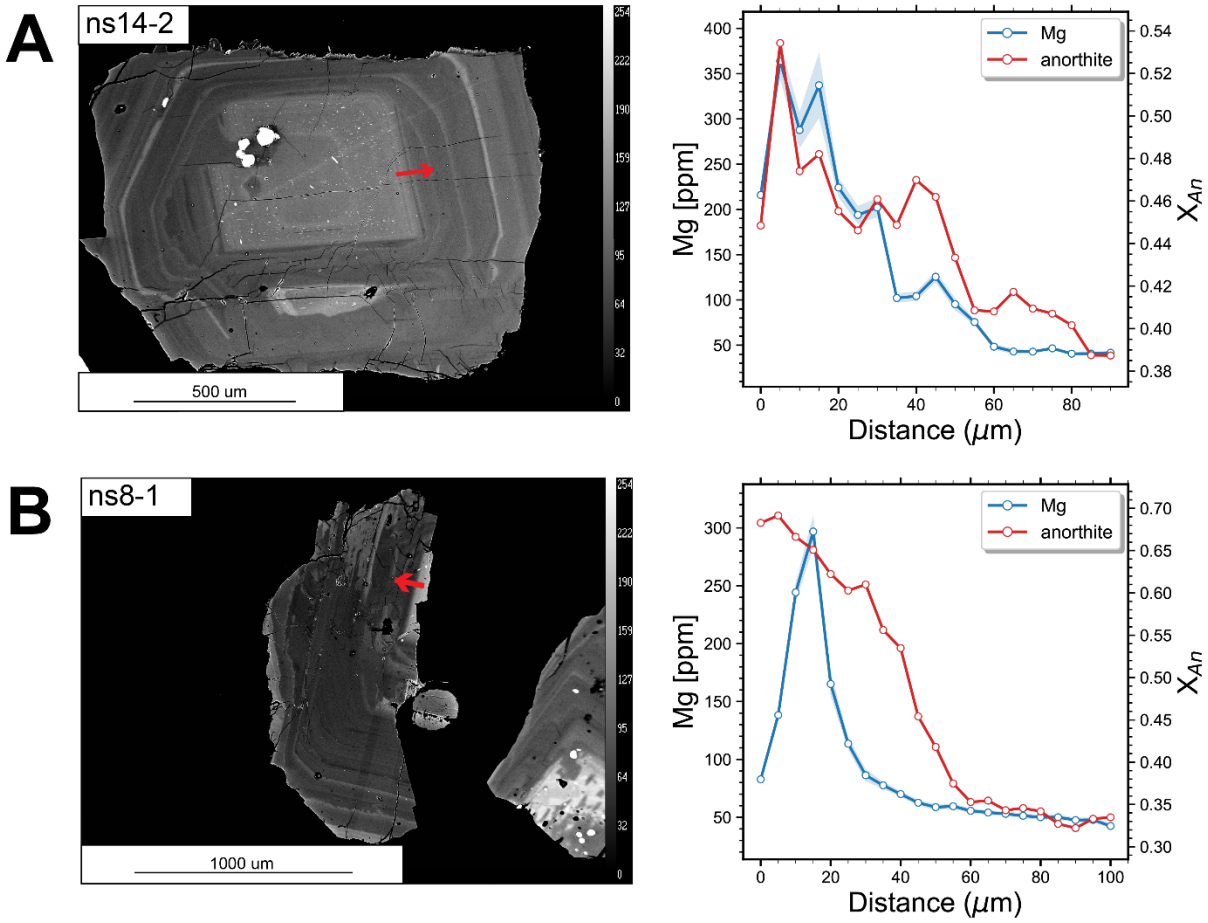

Figure 4: Plagioclase from the CGI exhibiting high-An cores. High-An cores in CGI plagioclase also consistently contain significantly higher Mg concentrations (e.g., > 200 µg/g). Some high-An core boundaries have Mg profile that also mimic the shape of the An profile well suggesting little to no diffusive equilibration (A), while others show significant deviation from the shape of the An profile (B).

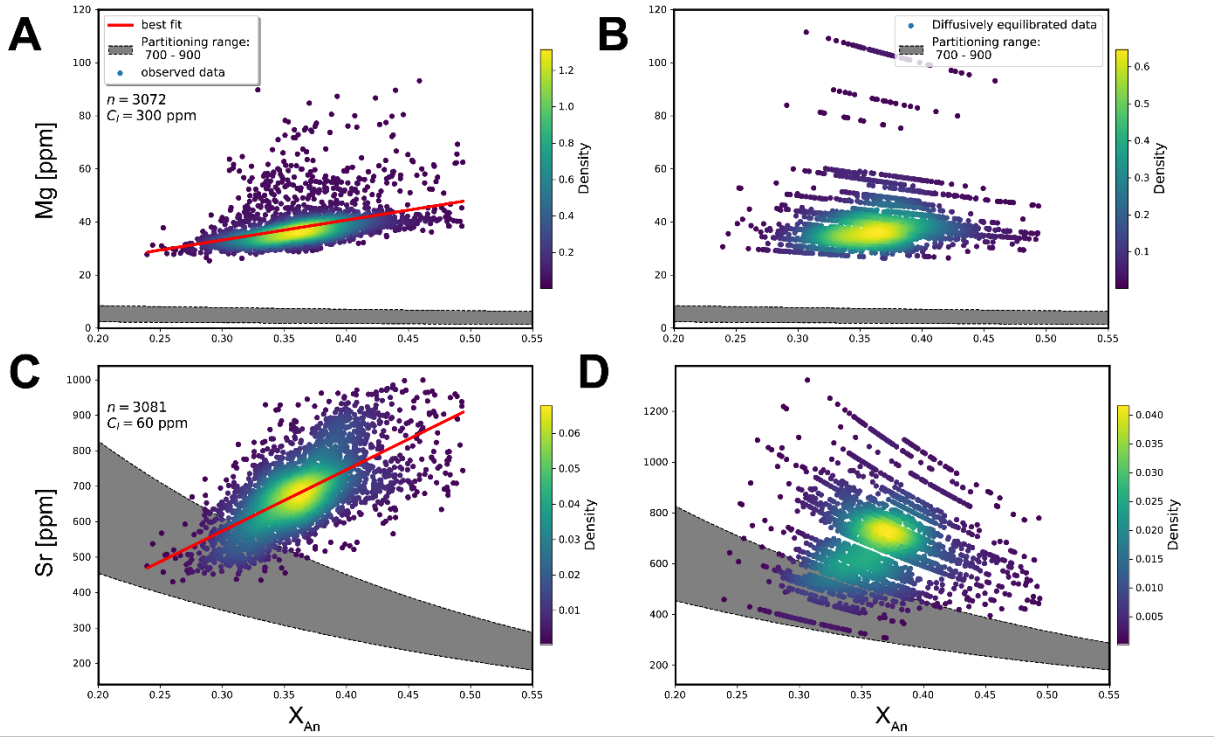

Figure 5: Strontium and Mg vs An in CGI plagioclase in both observed data (A, C) and calculated equilibrated data (B, D). Gray area is the range that would be predicted using Cs = Kd*Cl where Kd is calculated using Equation 1 and observed median glass composition. Based on the observed global positive correlations between Sr and Mg vs. An, CGI plagioclase are not in diffusive equilibration. Note, that even though diffusively equilibrated plagioclase do not fall within the gray region in (B, D), their slope still broadly matches that of the gray region. Gray region location on the charts is ultimately determined by an assumed liquid composition. B and D then suggest that CGI plagioclase have formed in a liquid that is elevated in Sr and Mg relative to erupted glass compositions.

Figure 6

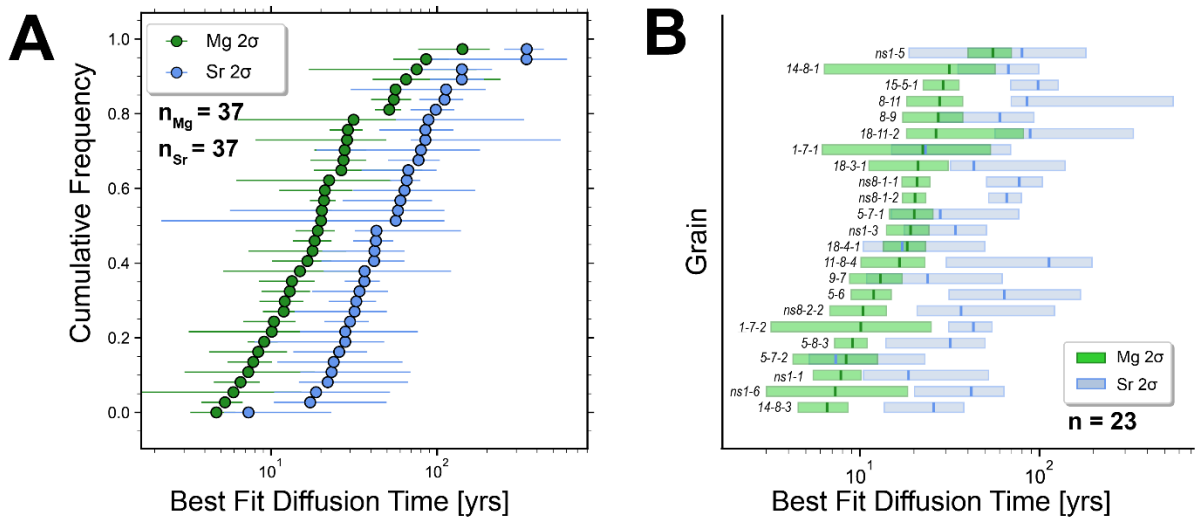

Figure 6: (A) Cumulative distribution plot of diffusion model results for both Sr and Mg in CGI plagioclase. (B) Comparison of Sr and Mg diffusion model results for transects in which both elements were modeled showing the discrepancy between Sr and Mg diffusion results. Labels correspond to the transect name, dark lines are mean best fit diffusion times of the Monte Carlo simulation, and boxes represent corresponding 2 sigma uncertainties.

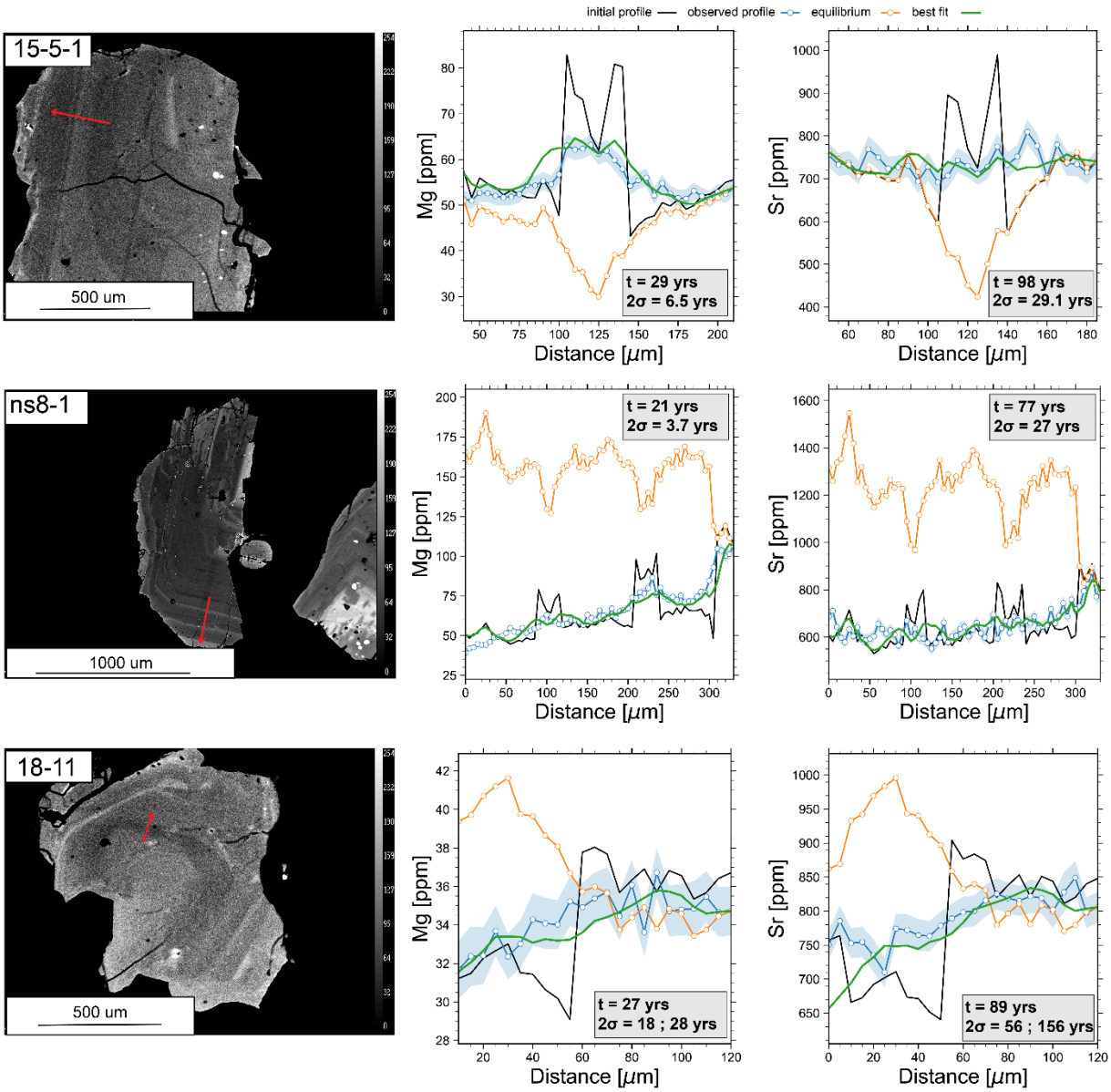

Figure 7: Representative plagioclase from the CGI. Left column: BSE images and the approximate location of the LA-ICP-MS transect analyzed. Middle column: Magnesium diffusion model annotated with best fit time and 2 sigma uncertainties. Right column: Strontium diffusion model annotated with best fit time and 2 sigma uncertainties. Note, that despite having diffusion coefficients that differ by a factor of ~5, diffusion widths (e.g., observed data deviation from model initial profiles) are relatively similar.

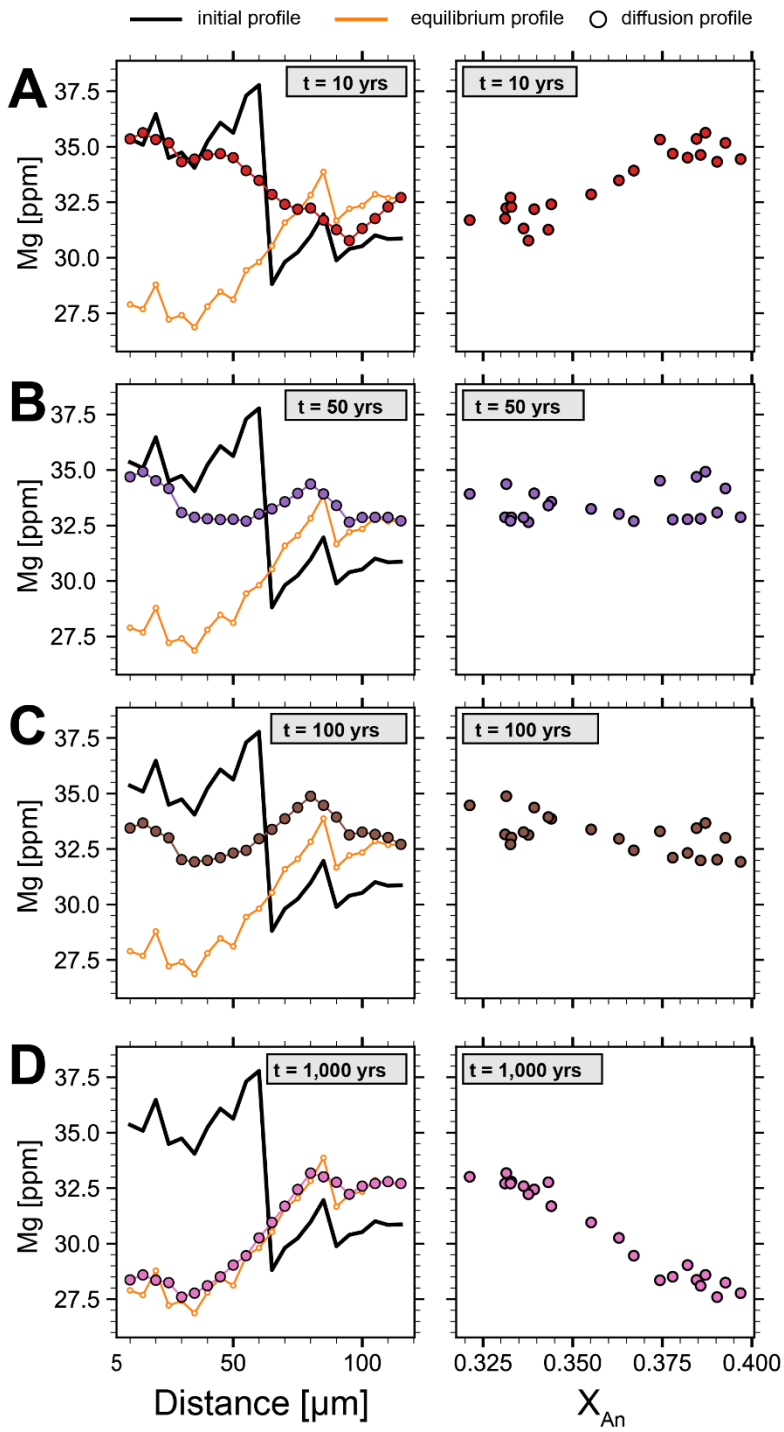

Figure 8: Magnesium diffusion model for transect 15-4 in both Mg vs. distance (left column) and Mg vs. An (right column). Different colored curves/dots correspond to different durations of the model: A) 10 years; B) 50 years; C) 100 years; D) 1000 years. Collectively these time-steps illustrate that as a given profile experiences longer durations of diffusion, it will progress towards its calculated equilibrium profile. In Mg vs An space (right column), this is a shift from positive to negative correlation. As negative correlations are never observed between Mg and An in CGI plagioclase, we take this to mean that CGI plagioclase have not spent long durations of time at or above 750 °C.

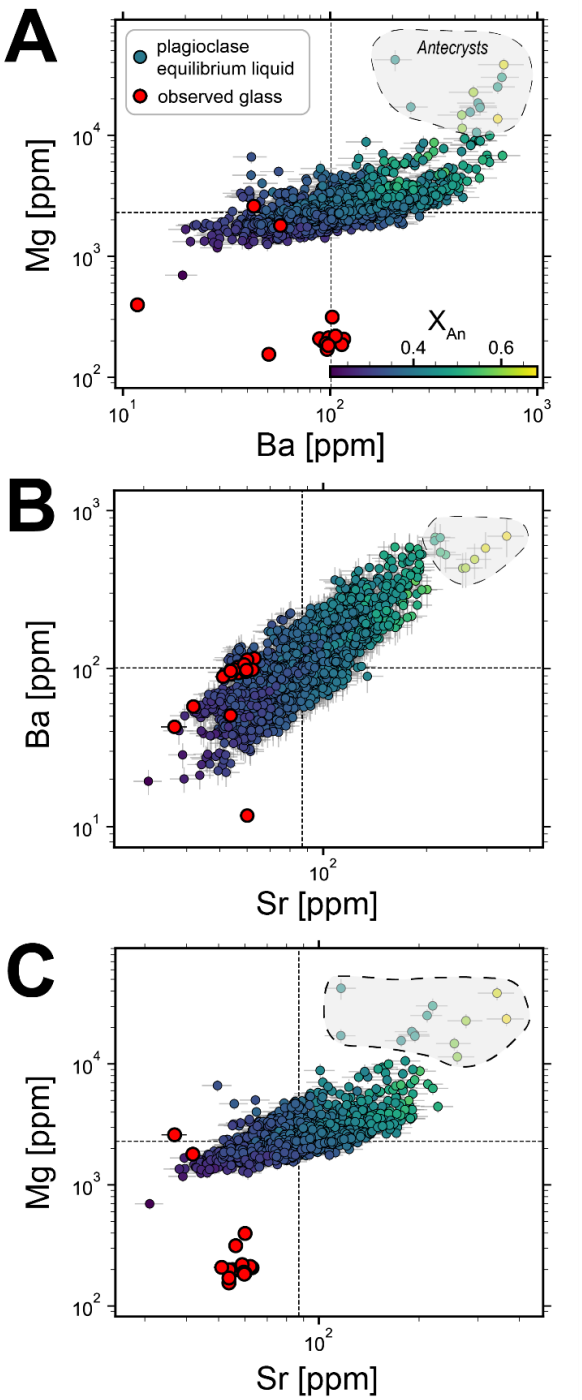

Figure 9: Comparing melt compositions in equilibrium with CGI plagioclase (colormapped circles) to observed glass compositions (red circles) for A) Mg vs Ba; B) Ba vs. Sr; C) Mg vs Sr. We see that the observed glass is more depleted in Sr (from plag fractionation), Mg (from biotite fractionation), and Ba (from biotite, sanidine, and, to a lesser degree plagioclase, fractionation). The elevated Mg equilibrium liquid comps suggest that much of the plagioclase that we analyzed crystallized before significant biotite fractionation. Potential antecrysts are identified as analyses that have Mg concentrations that are over an order of magnitude greater than the majority of analyses and outlined by the gray shaded regions in each plot.

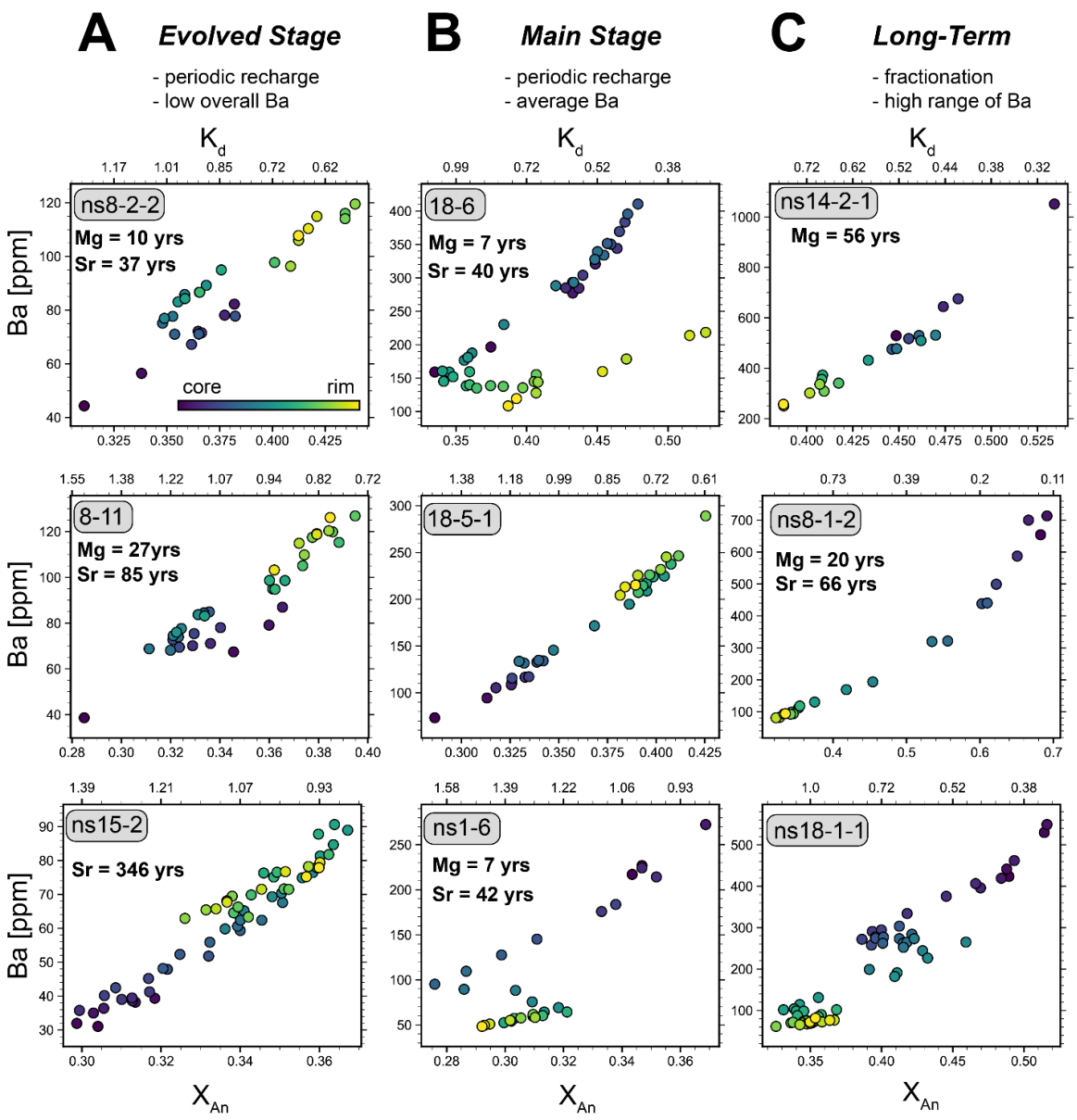

Figure 10: Schematic of different Ba equilibrium liquid – An relationships observed in CGI plagioclase. Circles are colored by the distance along the transect with darker colors being towards the interior of the grain and lighter colors being towards the rim. Top x axis is showing the partition coefficient for Ba in plagioclase at the equivalent X_{An} value on the primary x axis for 750 °C to indicate that at Ba is incompatible in plagioclase at $X_{An} > \sim 0.35$. Where diffusion models have been completed for a transect their best fit diffusion time is annotated in the upper left corner. Columns denote which stage of magmatic development the transect is hypothesized to be recording. Combined with Figure 9, this suggests that CGI plagioclase are recording diverse crystallization environments over a spectrum of melt compositions that are largely driven by the fractionation of plagioclase, biotite, and sanidine.

Supplementary Appendix and Figures:

Thermal budgets of magma storage constrained by diffusion chronometry: the Cerro Galán ignimbrite

Jordan Lubbers[1,2*], Adam Kent[1], Shanaka de Silva[1]
[1]College of Earth, Ocean, and Atmospheric Sciences, Oregon State University, Corvallis OR, 97331, USA
Now at:

[2]Alaska Volcano Observatory U.S. Geological Survey, Anchorage AK, 99508, USA

*Corresponding author: jelubber@gmail.com (920) 737-4821

Keywords: diffusion chronometry; thermal history; caldera forming eruption; silicic magmatism; plagioclase

Appendix 1:

Below we show the discretized solution to Equation 7 from Costa et al., (2003):

$$\frac{\delta C}{\delta t} = \left(\frac{\delta D}{\delta x}\frac{\delta C}{\delta x} + D\frac{\delta^2 C}{\delta x^2}\right) - \frac{A}{RT}\left(D\frac{\delta C}{\delta x}\frac{\delta X_{An}}{\delta x} + C\frac{\delta D}{\delta x}\frac{\delta X_{An}}{\delta x} + DC\frac{\delta^2 X_{An}}{\delta x^2}\right)$$

Following the method of Costa et al., (2008), the discretized version used in the model is then:

$$C_{i,j+1} = C_{i,j} + \Delta t\left[\left(\frac{D_{i+1,j} - D_{i,j}}{\Delta x}\right)\left(\frac{C_{i+1,j} - C_{i,j}}{\Delta x}\right) + D_{i,j}\left(\frac{C_{i+1,j} - 2C_{i,j} + C_{i-1,j}}{\Delta x^2}\right)\right] - \frac{A}{RT}\left[D_{i,j}\left(\frac{C_{i+1,j} - C_{i,j}}{\Delta x}\cdot\frac{An_{i+1,j} - An_{i,j}}{\Delta x}\right) + C_{i,j}\left(\frac{D_{i+1,j} - D_{i,j}}{\Delta x}\cdot\frac{An_{i+1,j} - An_{i,j}}{\Delta x}\right) + D_{i,j}C_{i,j}\left(\frac{An_{i+1,j} - 2An_{i,j} + An_{i-1,j}}{\Delta x^2}\right)\right]$$

Where points in space are denoted by "i" and steps in time are denoted by "j".

Costa, F., Chakraborty, S., & Dohmen, R. (2003). *Diffusion coupling between trace and major elements and a model for calculation of magma residence times using plagioclase*. https://doi.org/10.1016/S0016-7037(00)01345-5

Costa, F., Dohmen, R., & Chakraborty, S. (2008). Time scales of magmatic processes from modeling the zoning patterns of crystals. *Reviews in Mineralogy and Geochemistry*, *69*, 545–594. https://doi.org/10.2138/rmg.2008.69.14

Supplementary Figures

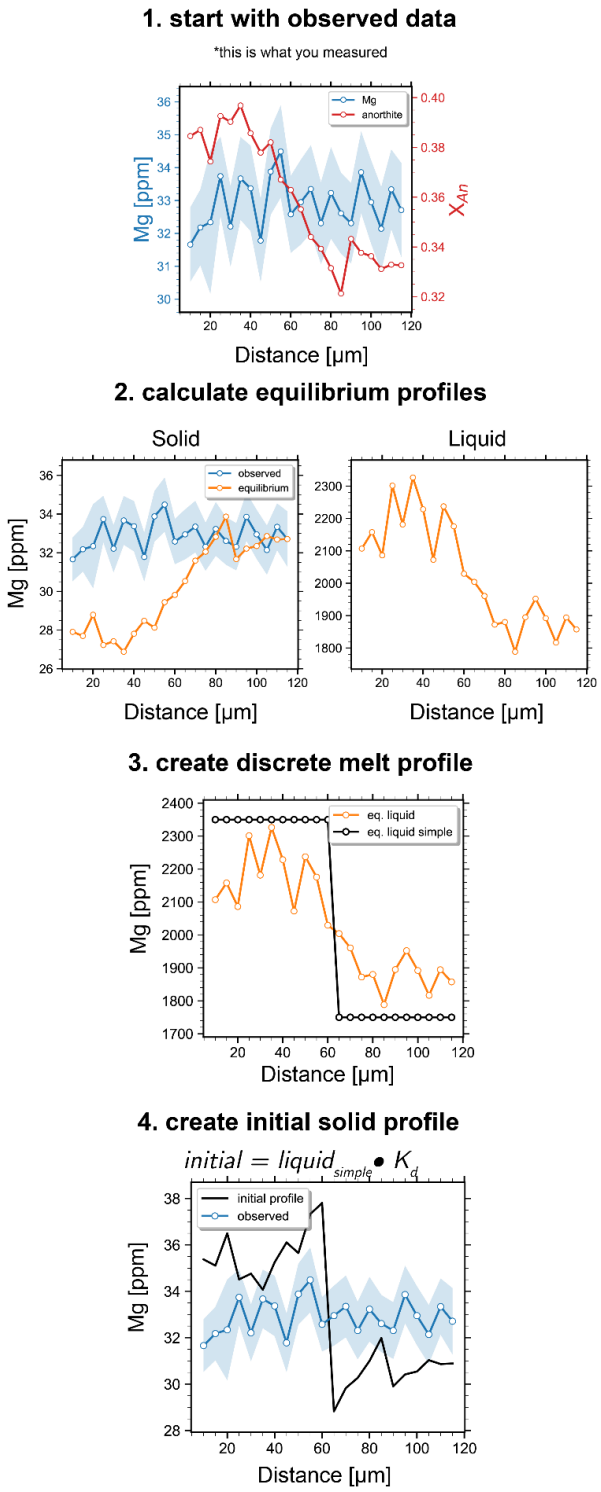

Figure S1: Figure representing how initial profiles are determined in our diffusion model using "effective melt compositions".

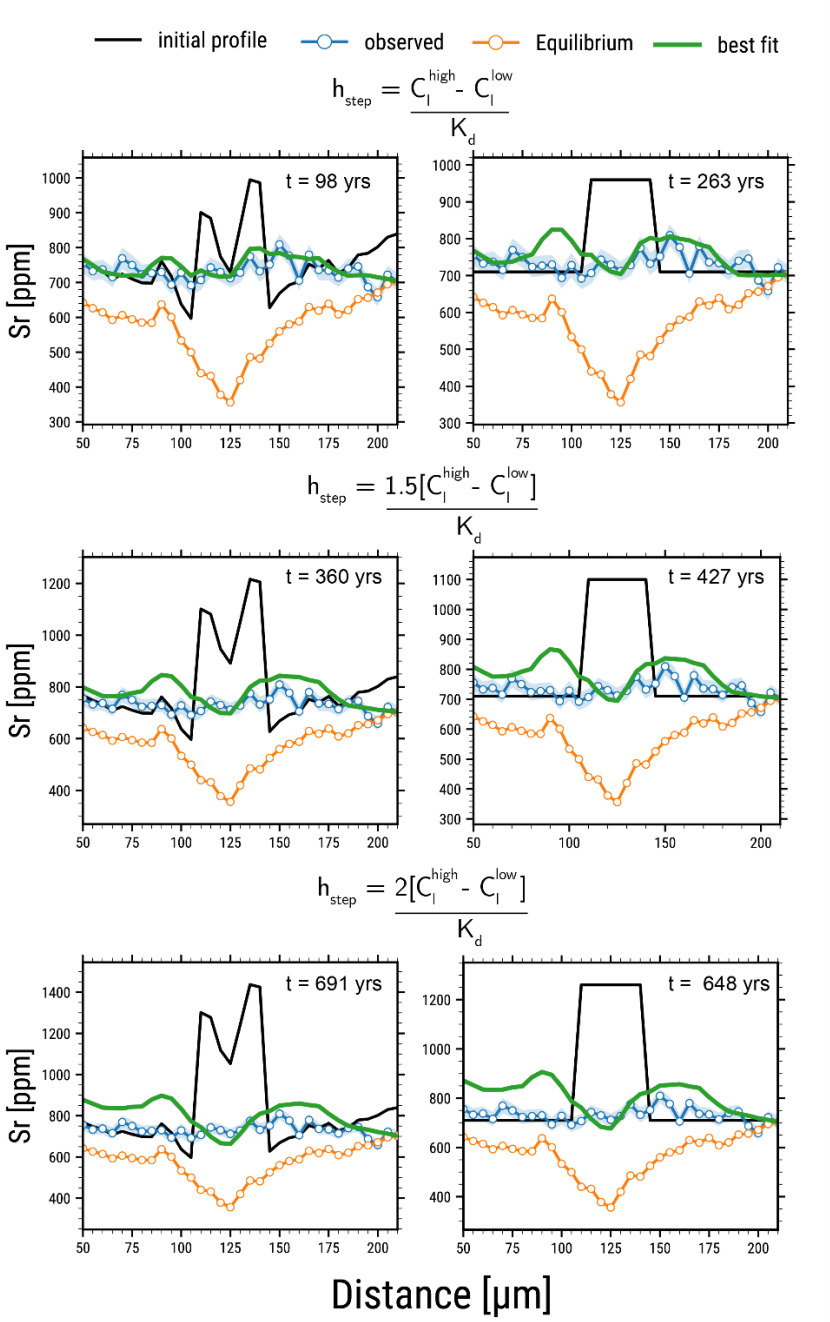

Figure S2: Influence of initial model profile geometry on the overall model fit quality. Shown is transect 15-5-1 (Figure 7 top row in main manuscript text) modeled at 6 different scenarios. Left column diffusion models have initial model profiles calculated using the methodology in Figure S1 (i.e., creating a step function in the effective melt composition profile and then applying that discrete melt profile to the observed data). Rows vary the height of the step function. In the top row the height is the observed maximum and minimum values of the effective melt composition profile and is the method used in this study. Middle row is 1.5 times the height of the top row, and the bottom row is 2 times the height of the top row. Right column is using the "classical" step function approach where a step function is created by assuming discrete solid compositions in the crystal only. We show that, of all 6 scenarios, only the method used in this study adequately produces a fit to the observed data using the solution to the diffusion equation outlined in Costa et al., (2003).

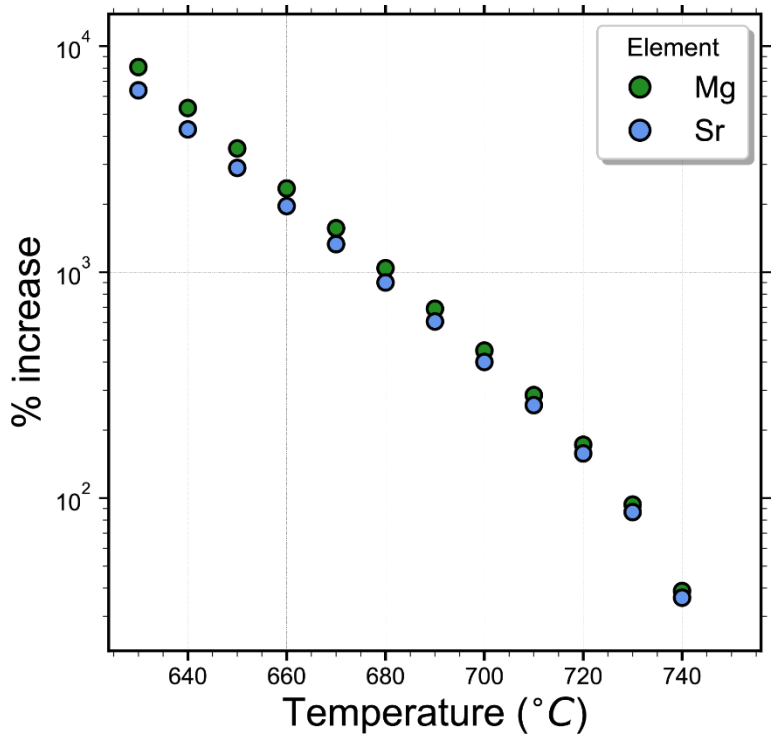

Figure S3: Influence of temperature on our diffusion model. Shown is a percent increase in diffusion time from models run at 750 degrees C vs temperature (i.e., if diffusion models were run at 680 degrees C it would have a best fit time ~10 times longer).

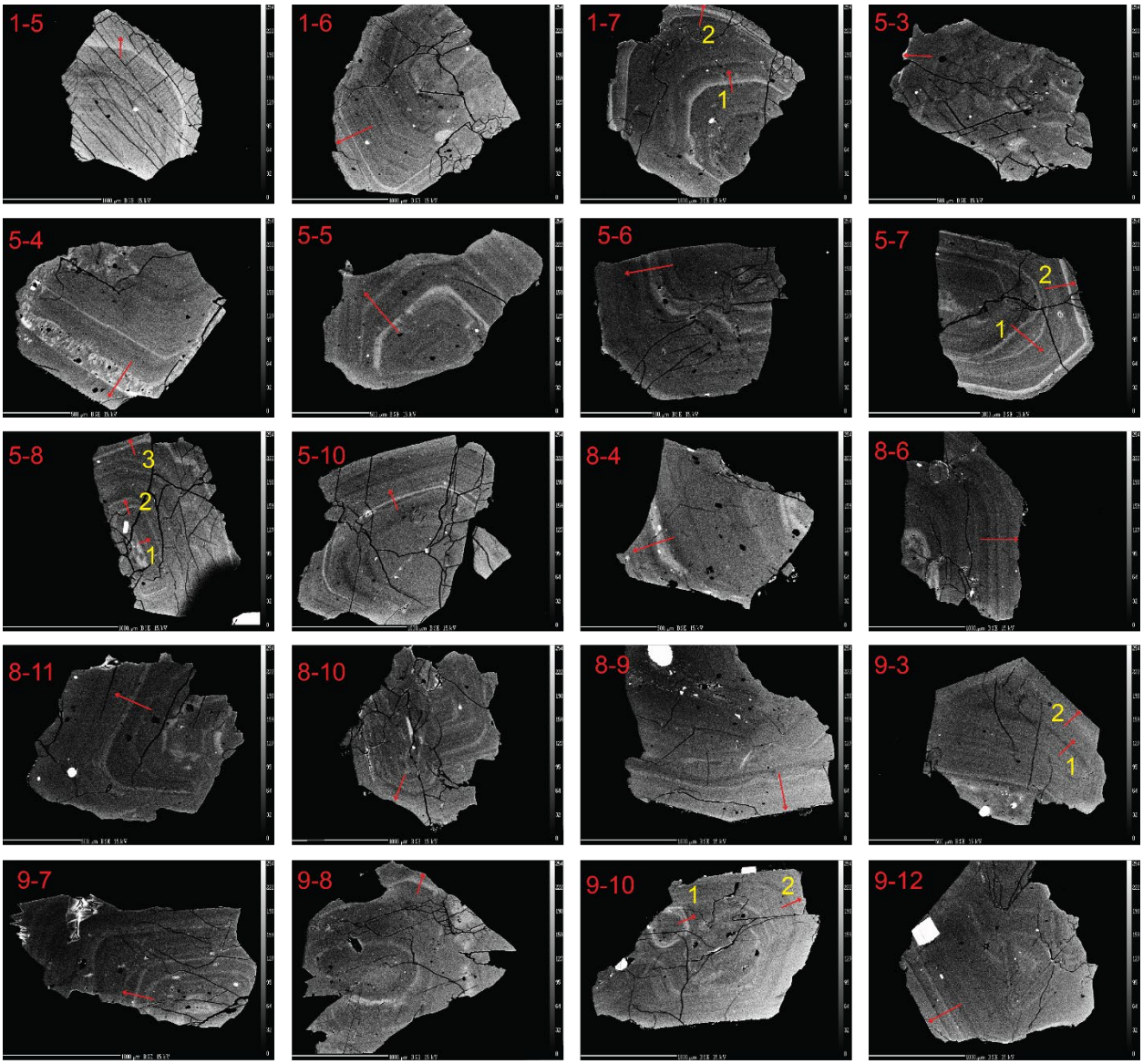

Figure S4: All BSE images for plagioclase grains with geochemical data. Red arrows are approximate length and direction of LA-ICP-MS transect. All transects are 50 um wide.

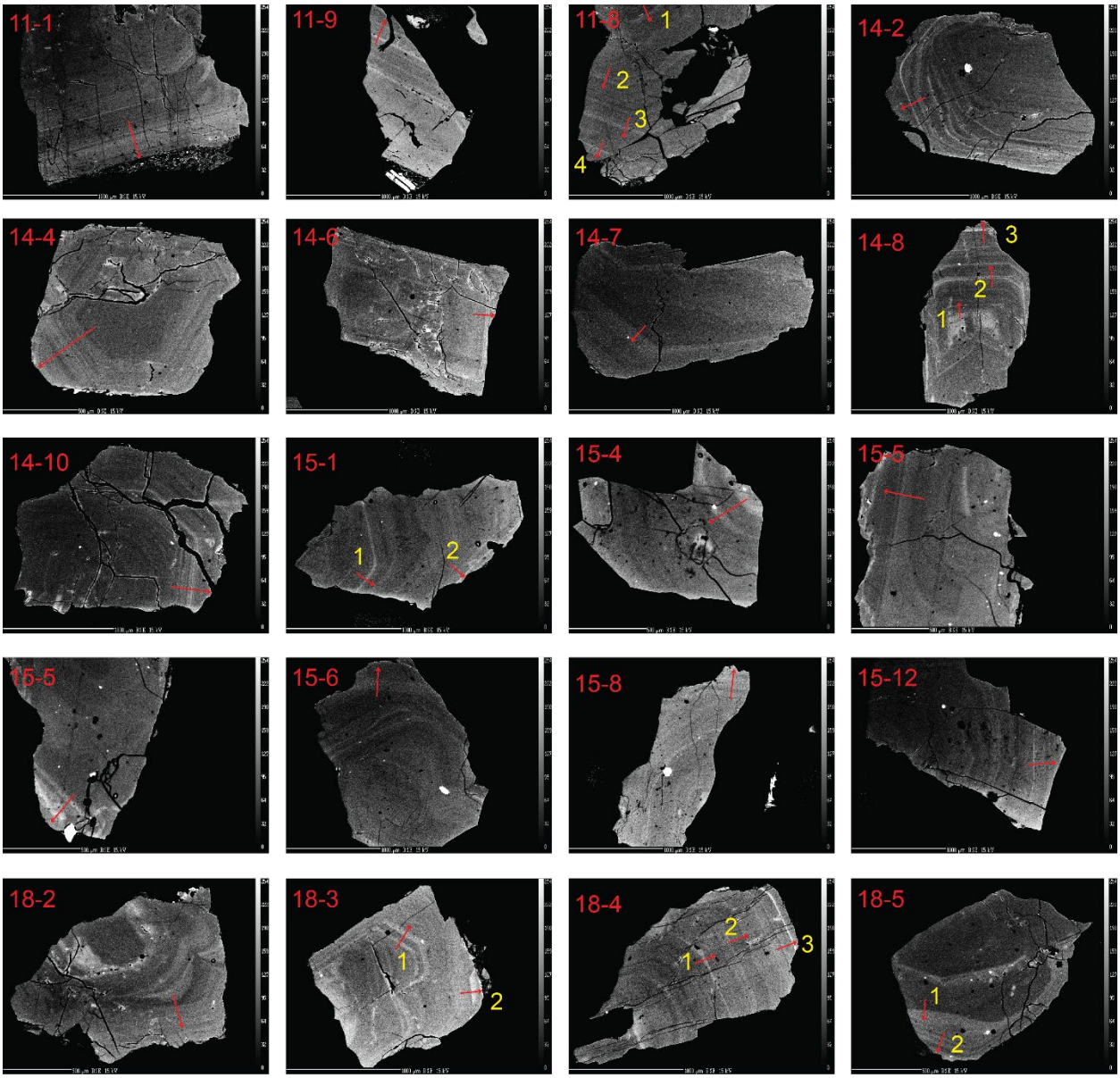

Figure S4 continued

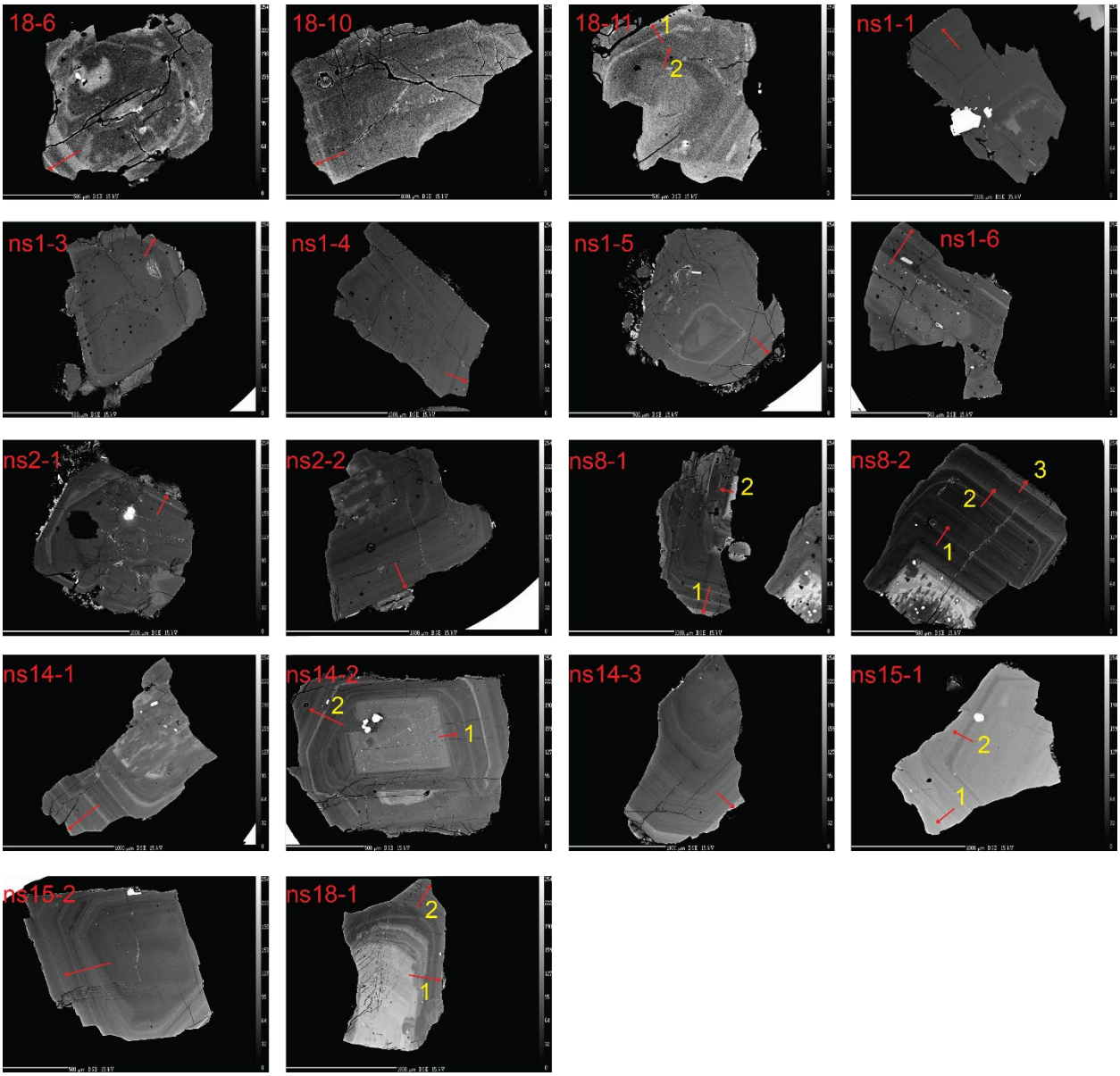

Figure S4 continued

Figure S5: All 37 Sr and Mg diffusion models. Each diffusion model has an A,B,C,D with the transect name located at the top. A) Observed trace element profile and An profile. B) Effective liquid composition calculated by Sr or Mg / K_d or for each point in the profile. Orange line is the "simplified" effective liquid created by using local peaks and valleys to create a series of discrete compositions that resemble step functions. C) Diffusion model result. Black line is the initial profile, blue line and shaded area are the observed Sr or Mg data and 1 sigma uncertainty, respectively, green is model best fit to the observed data, and the orange line is the calculated equilibrium profile based on the most rimward (right) analysis. D) The results of the Monte Carlo simulation. Histogram of best fit times along with the statistics of the distribution (i.e., mean, 2-sigma uncertainty, median, etc.). Where data have been transformed to fit a normal distribution prior to finding the uncertainty there will be two values for the 2-sigma uncertainty (i.e., lower and upper 2-sigma uncertainty).

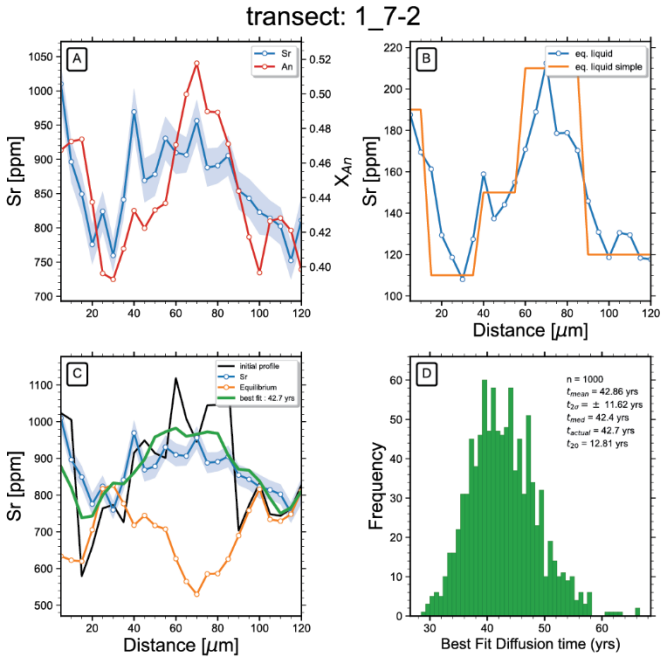

transect: 5_6

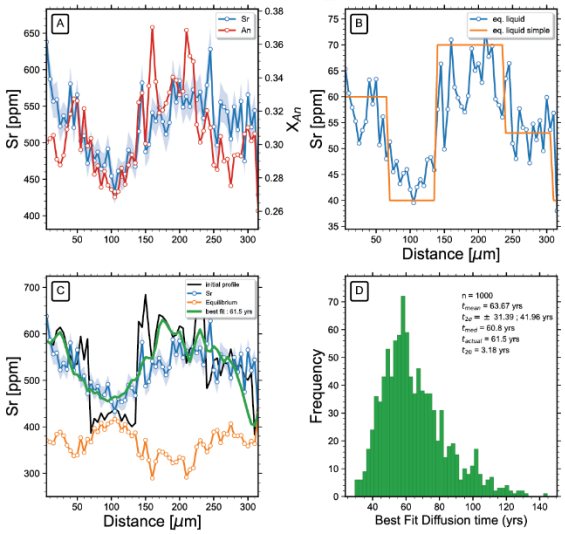

transect: 5_7-1

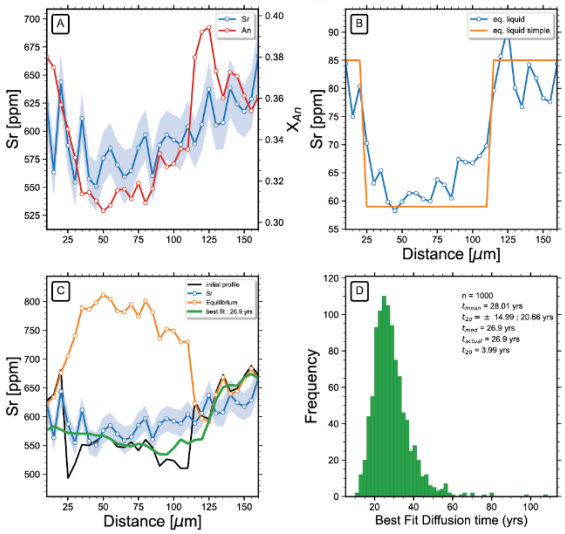

transect: 5_7-2

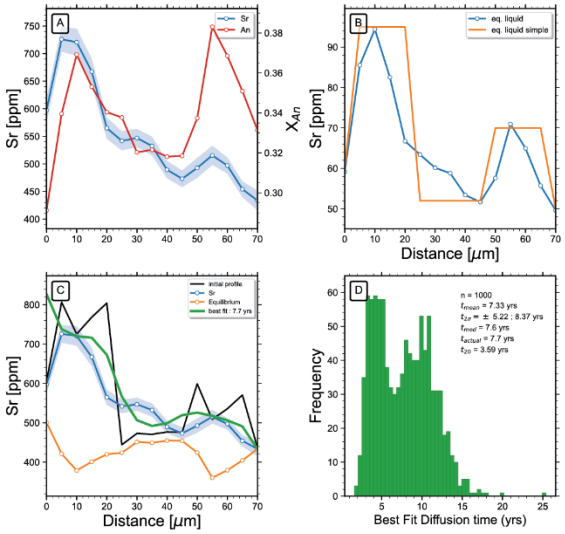

transect: 5_8-3

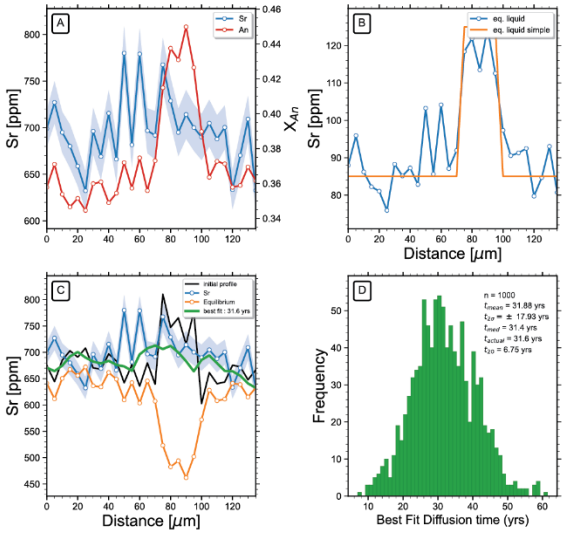

transect: 5_10

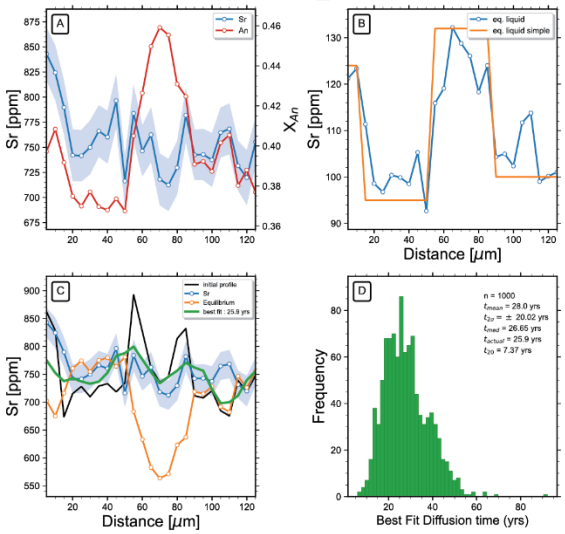

transect: 8_4

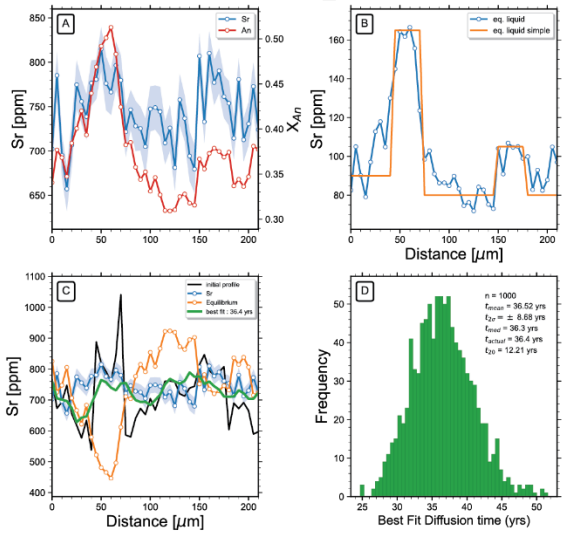

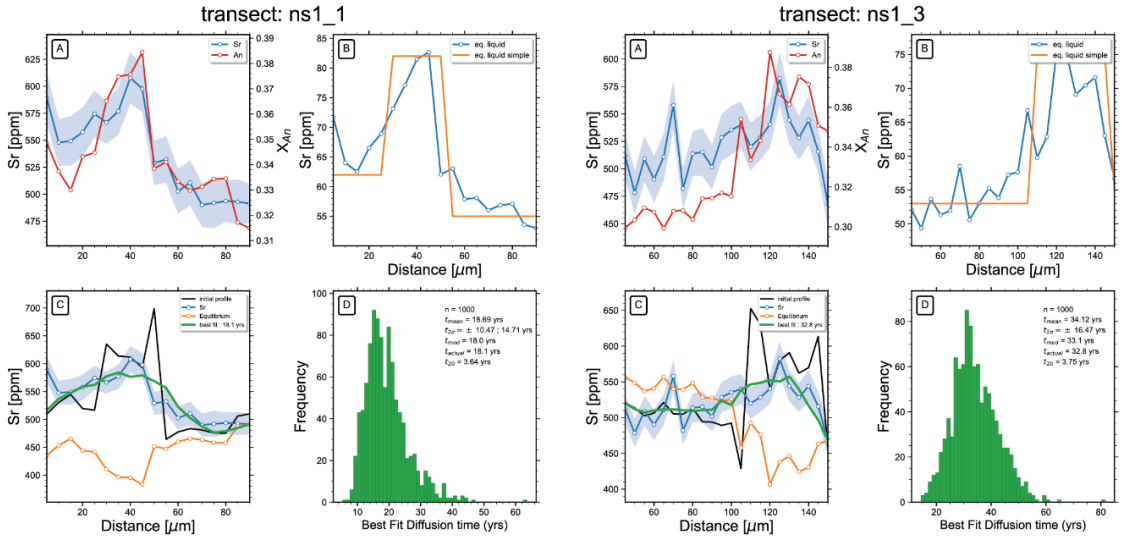
transect: ns1_1
A
Sr
An
Sr [ppm]
X_{An}
B
eq. liquid
eq. liquid simple
Distance [μm]
C
initial profile
Sr
Equilibrium
best fit : 18.1 yrs
Distance [μm]
D
n = 1000
t_{mean} = 18.69 yrs
$t_{2\sigma}$ = ± 10.47 ; 14.71 yrs
t_{mod} = 18.0 yrs
t_{actual} = 18.1 yrs
t_{20} = 3.64 yrs
Frequency
Best Fit Diffusion time (yrs)

transect: ns1_3
A
Sr
An
Sr [ppm]
X_{An}
B
eq. liquid
eq. liquid simple
Distance [μm]
C
initial profile
Sr
Equilibrium
best fit : 32.8 yrs
Distance [μm]
D
n = 1000
t_{mean} = 34.12 yrs
$t_{2\sigma}$ = ± 16.47 yrs
t_{mod} = 33.1 yrs
t_{actual} = 32.8 yrs
t_{20} = 3.75 yrs
Frequency
Best Fit Diffusion time (yrs)

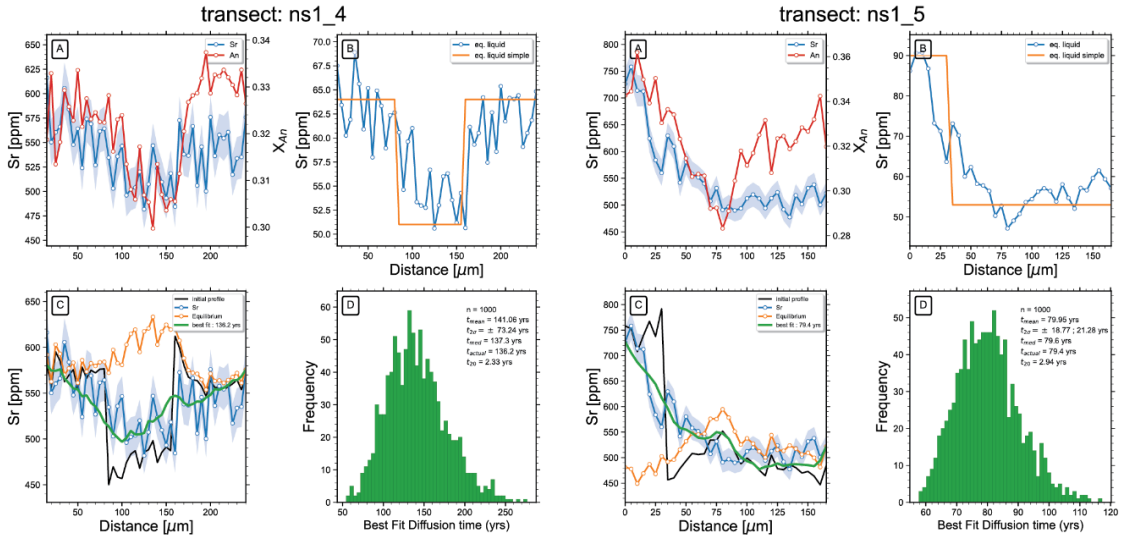
transect: ns1_4
A
Sr
An
Sr [ppm]
X_{An}
B
eq. liquid
eq. liquid simple
Distance [μm]
C
initial profile
Sr
Equilibrium
best fit : 136.2 yrs
Distance [μm]
D
n = 1000
t_{mean} = 141.06 yrs
$t_{2\sigma}$ = ± 73.24 yrs
t_{mod} = 137.3 yrs
t_{actual} = 136.2 yrs
t_{20} = 2.33 yrs
Frequency
Best Fit Diffusion time (yrs)

transect: ns1_5
A
Sr
An
Sr [ppm]
X_{An}
B
eq. liquid
eq. liquid simple
Distance [μm]
C
initial profile
Sr
Equilibrium
best fit : 79.4 yrs
Distance [μm]
D
n = 1000
t_{mean} = 79.95 yrs
$t_{2\sigma}$ = ± 18.77 ; 21.28 yrs
t_{mod} = 79.6 yrs
t_{actual} = 79.4 yrs
t_{20} = 2.94 yrs
Frequency
Best Fit Diffusion time (yrs)

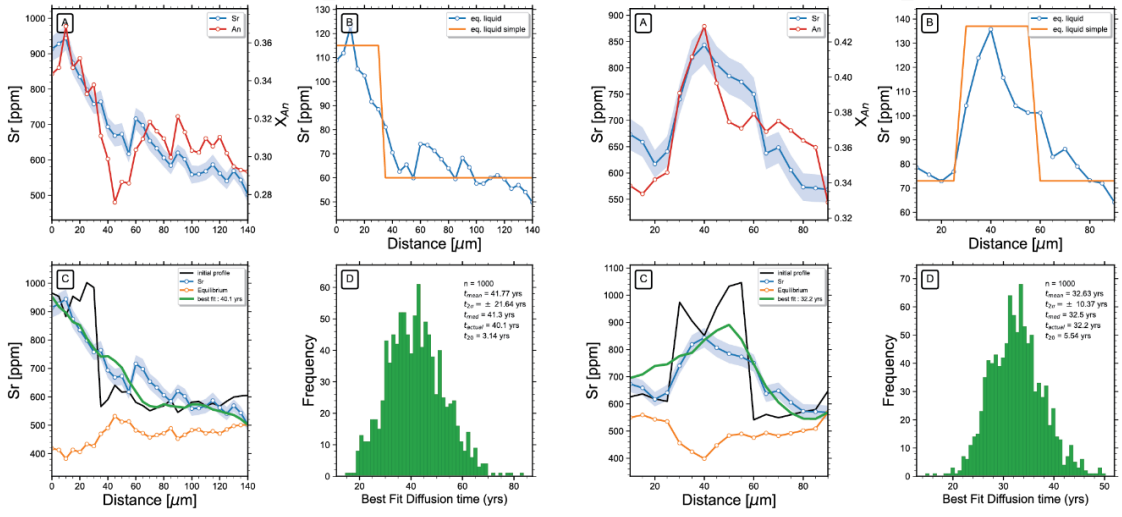
transect: ns1_6
A
Sr
An
Sr [ppm]
X_{An}
B
eq. liquid
eq. liquid simple
Distance [μm]
C
initial profile
Sr
Equilibrium
best fit : 40.1 yrs
Distance [μm]
D
n = 1000
t_{mean} = 41.77 yrs
$t_{2\sigma}$ = ± 21.64 yrs
t_{mod} = 41.3 yrs
t_{actual} = 40.1 yrs
t_{20} = 3.14 yrs
Frequency
Best Fit Diffusion time (yrs)

transect: ns2_1
A
Sr
An
Sr [ppm]
X_{An}
B
eq. liquid
eq. liquid simple
Distance [μm]
C
initial profile
Sr
Equilibrium
best fit : 32.2 yrs
Distance [μm]
D
n = 1000
t_{mean} = 32.63 yrs
$t_{2\sigma}$ = ± 10.37 yrs
t_{mod} = 32.5 yrs
t_{actual} = 32.2 yrs
t_{20} = 5.54 yrs
Frequency
Best Fit Diffusion time (yrs)

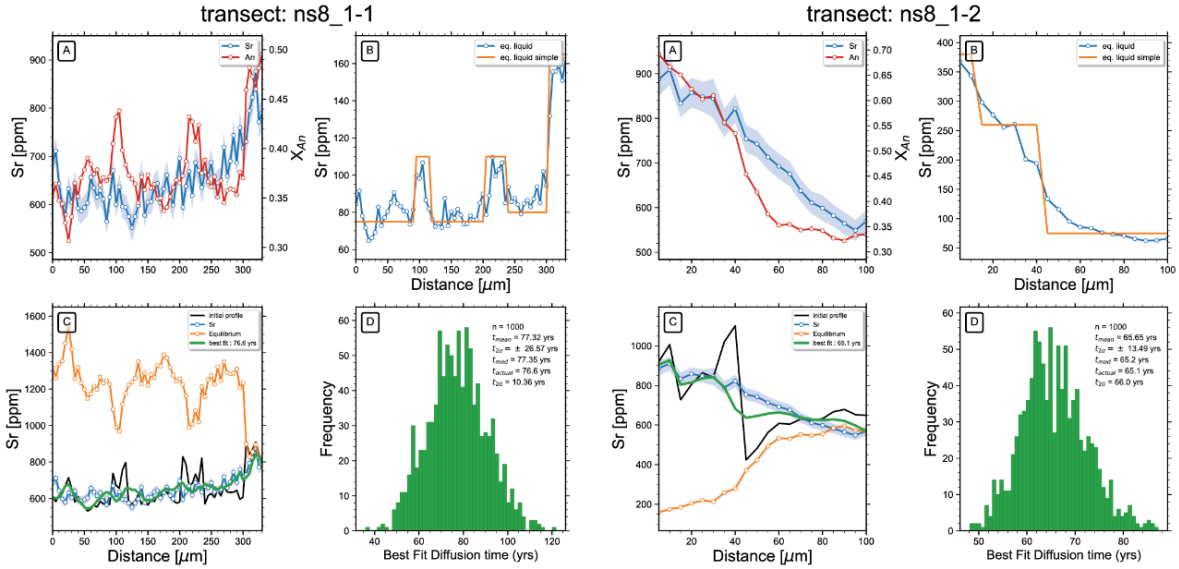
transect: ns8_1-1
A
Sr
An
Sr [ppm]
X_{An}
B
eq. liquid
eq. liquid simple
Distance [μm]
C
initial profile
Sr
Equilibrium
best fit : 76.6 yrs
D
n = 1000
t_{mean} = 77.32 yrs
$t_{2\sigma}$ = ± 26.57 yrs
t_{med} = 77.35 yrs
t_{actual} = 76.6 yrs
$t_{2\sigma}$ = 10.36 yrs
Frequency
Best Fit Diffusion time (yrs)
transect: ns8_1-2
best fit : 65.1 yrs
n = 1000
t_{mean} = 65.65 yrs
$t_{2\sigma}$ = ± 13.49 yrs
t_{med} = 65.2 yrs
t_{actual} = 65.1 yrs
$t_{2\sigma}$ = 66.0 yrs

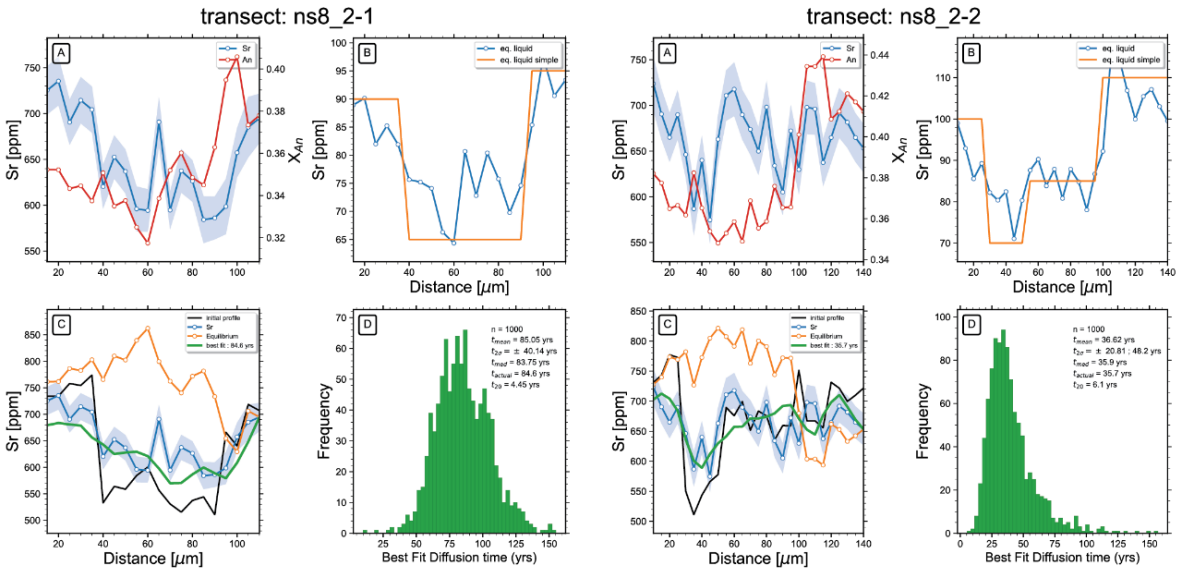
transect: ns8_2-1
best fit : 84.6 yrs
n = 1000
t_{mean} = 85.05 yrs
$t_{2\sigma}$ = ± 40.14 yrs
t_{med} = 83.75 yrs
t_{actual} = 84.6 yrs
$t_{2\sigma}$ = 4.45 yrs
transect: ns8_2-2
best fit : 35.7 yrs
n = 1000
t_{mean} = 36.62 yrs
$t_{2\sigma}$ = ± 20.81 : 48.2 yrs
t_{med} = 35.9 yrs
t_{actual} = 35.7 yrs
$t_{2\sigma}$ = 6.1 yrs

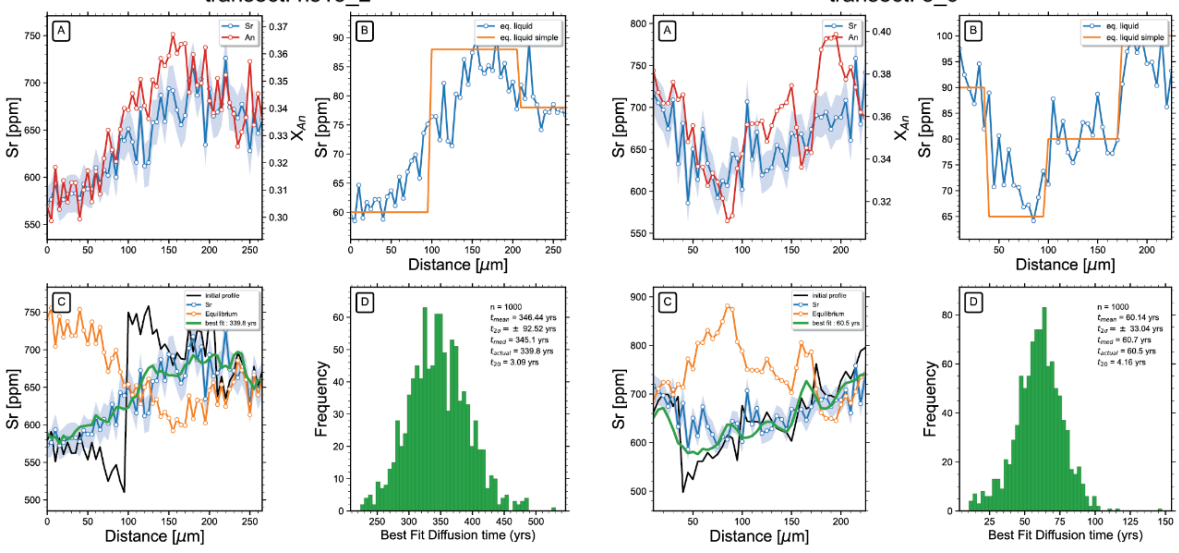
transect: ns15_2
best fit : 339.8 yrs
n = 1000
t_{mean} = 346.44 yrs
$t_{2\sigma}$ = ± 92.52 yrs
t_{med} = 345.1 yrs
t_{actual} = 339.8 yrs
$t_{2\sigma}$ = 3.09 yrs
transect: 8_9
best fit : 60.5 yrs
n = 1000
t_{mean} = 60.14 yrs
$t_{2\sigma}$ = ± 33.04 yrs
t_{med} = 60.7 yrs
t_{actual} = 60.5 yrs
$t_{2\sigma}$ = 4.16 yrs

transect: 8_11

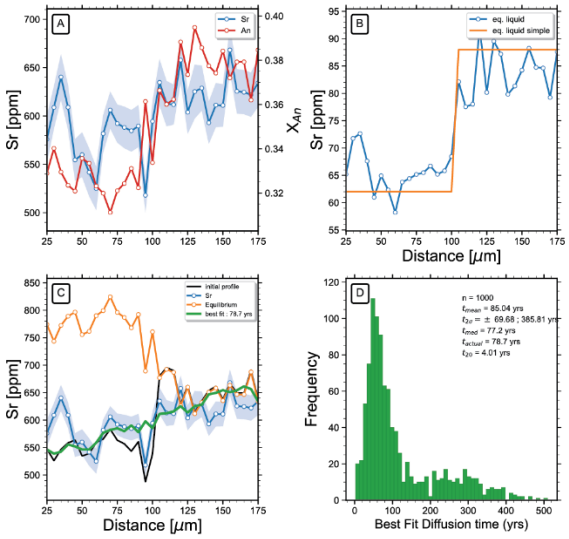

transect: 9_3_2

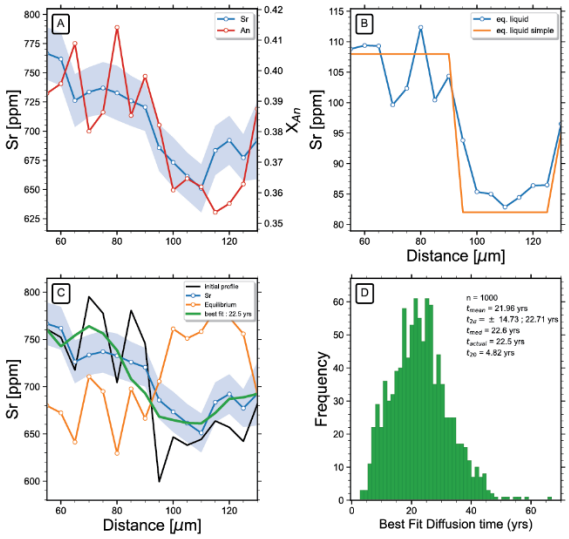

transect: 9_7

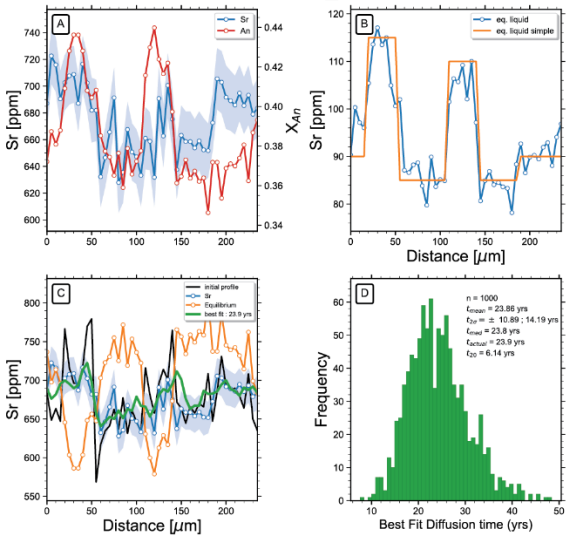

transect: 11_8_3

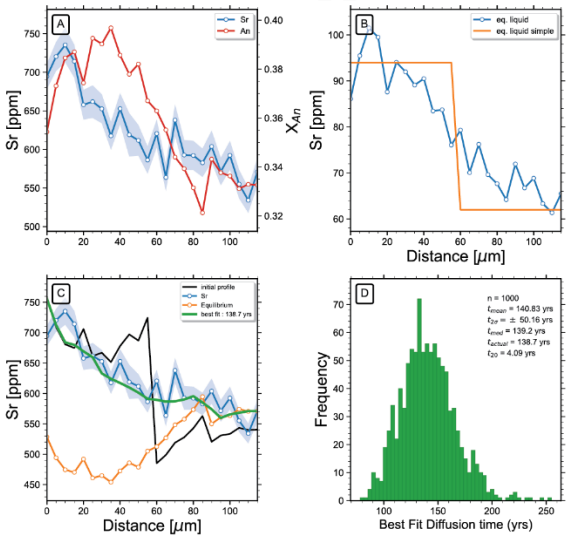

transect: 11_8_4

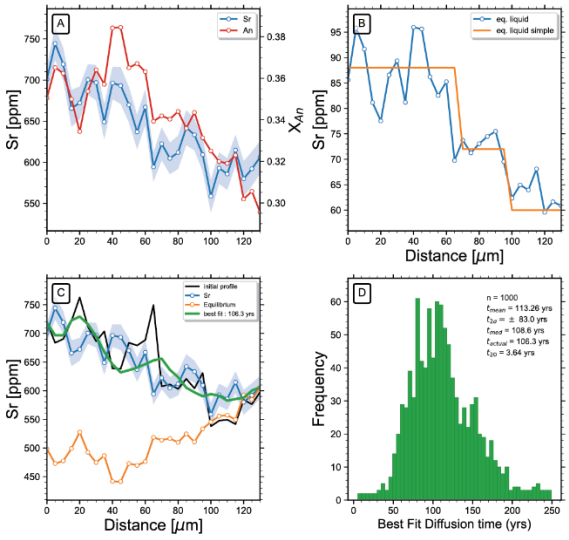

transect: 11_9

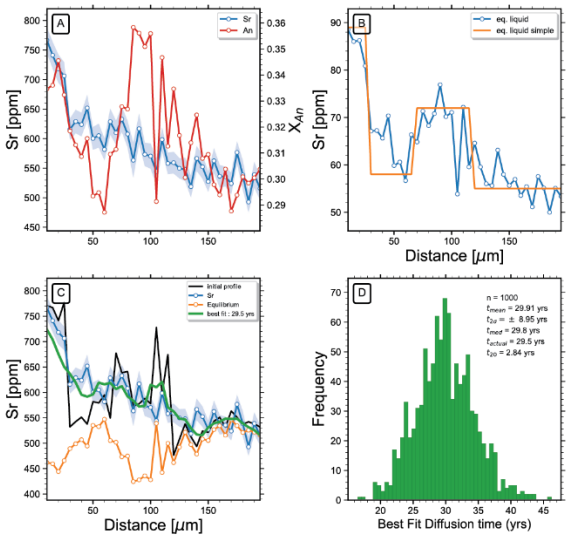

transect: 14_2

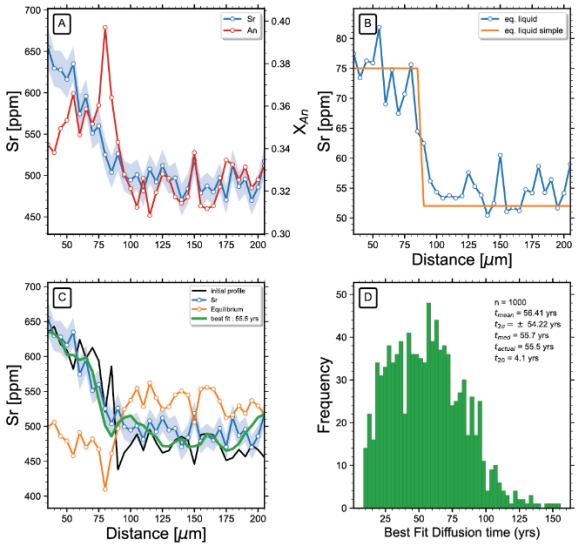

transect: 14_8_1

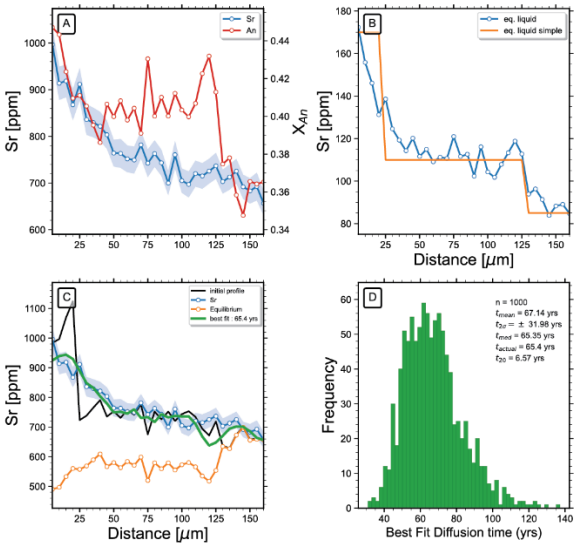

transect: 14_8_3

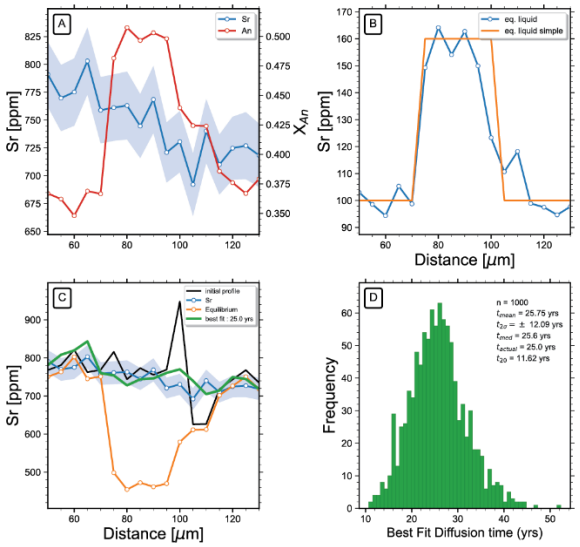

transect: 15_1_1

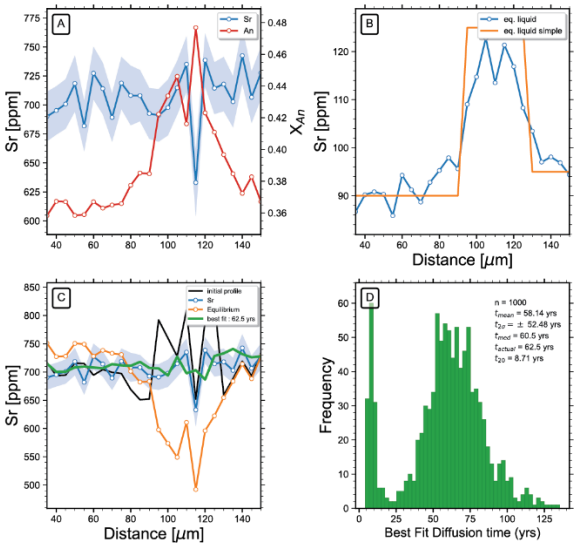

transect: 15_5_1

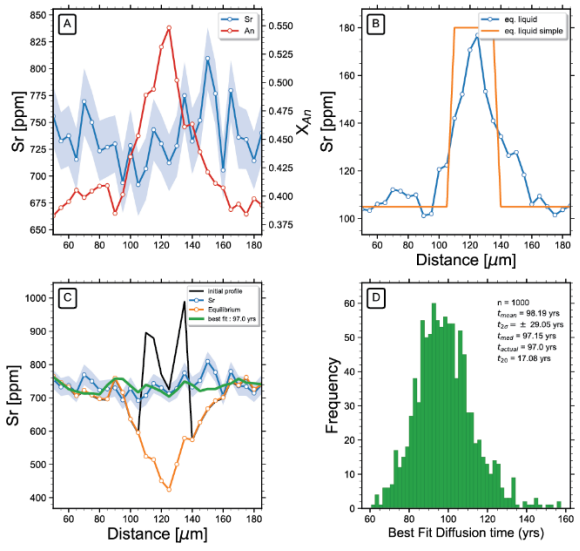

transect: 15_6

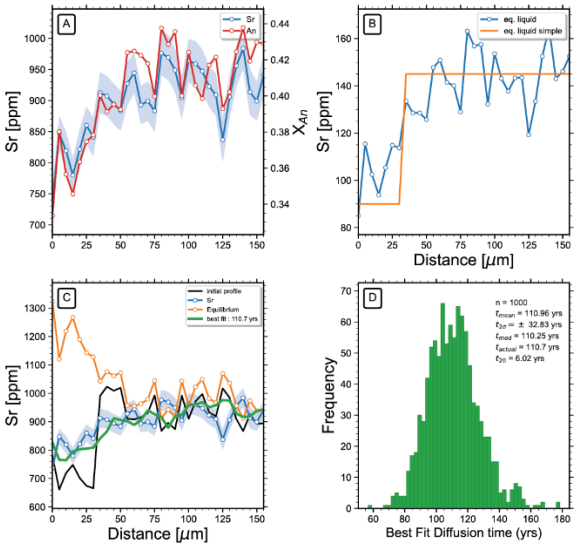

transect: 18_3_1

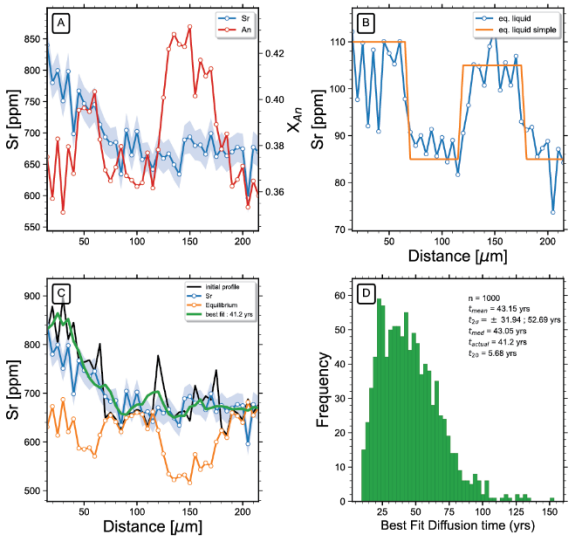

transect: 18_4_1

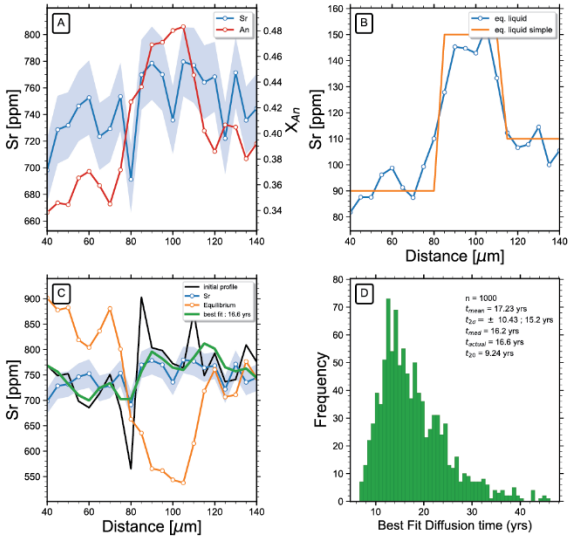

transect: 18_10

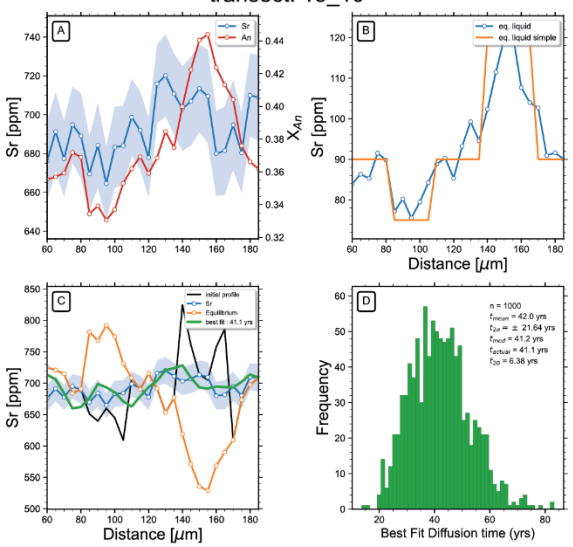

transect: 18_11_2

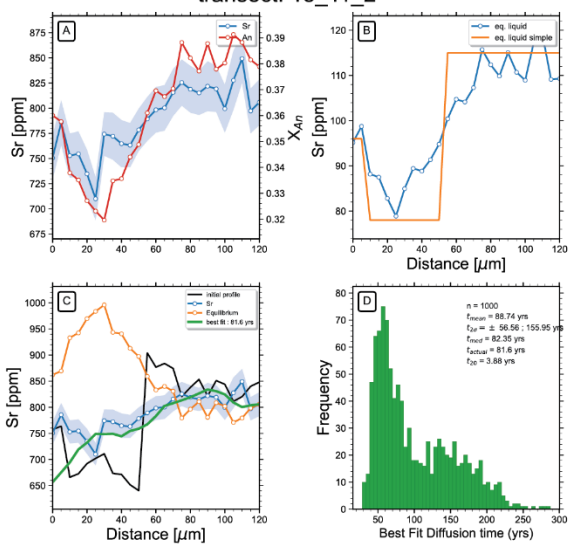

transect: 5_4

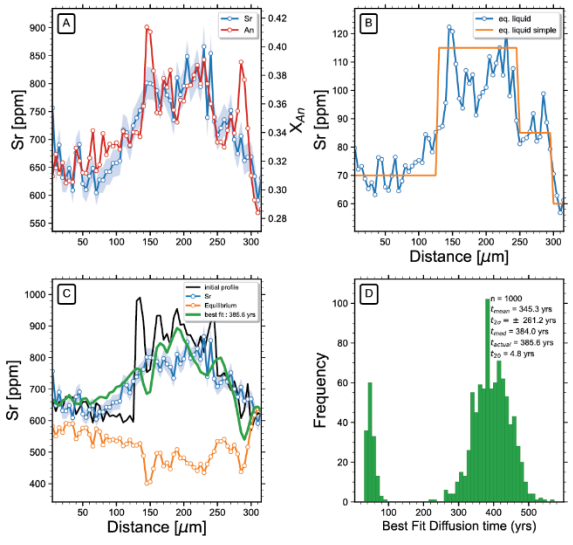

transect: 1_7-1

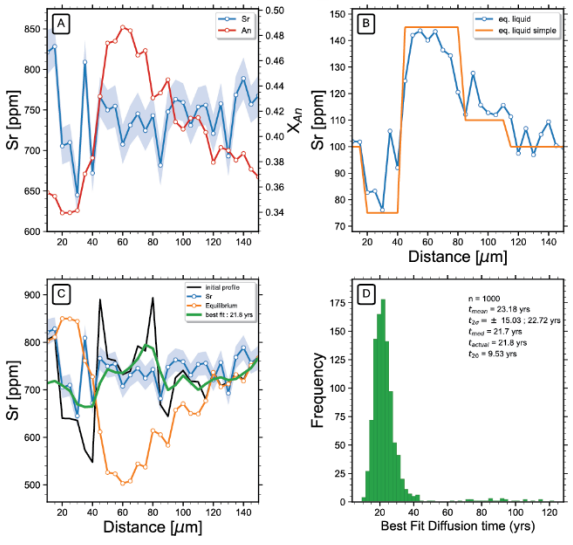

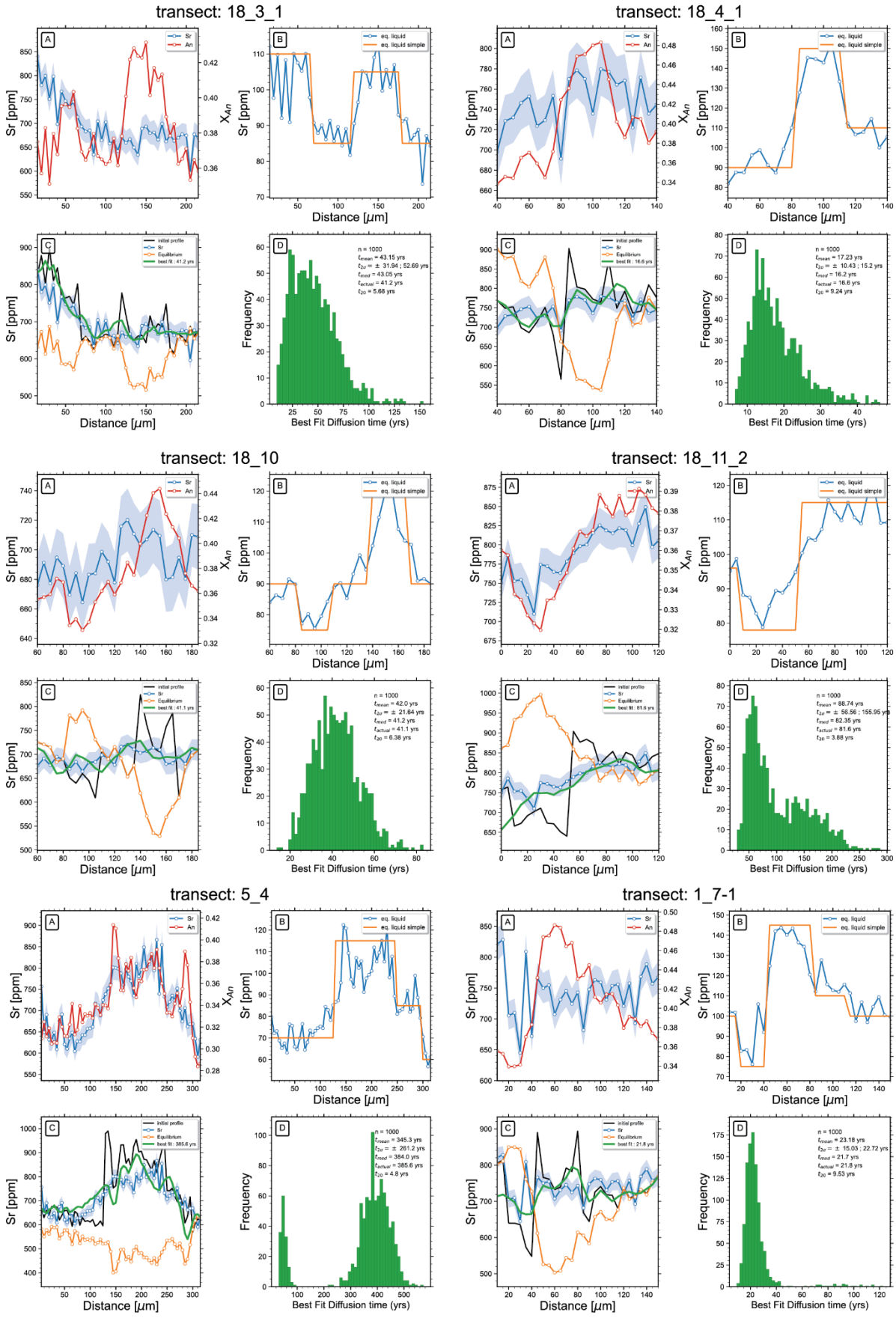
transect: 18_3_1
transect: 18_4_1
transect: 18_10
transect: 18_11_2
transect: 5_4
transect: 1_7-1
A
B
C
D
Sr
An
eq. liquid
eq. liquid simple
initial profile
Equilibrium
Sr [ppm]
X_{An}
Distance [μm]
Frequency
Best Fit Diffusion time (yrs)

transect: 8_11

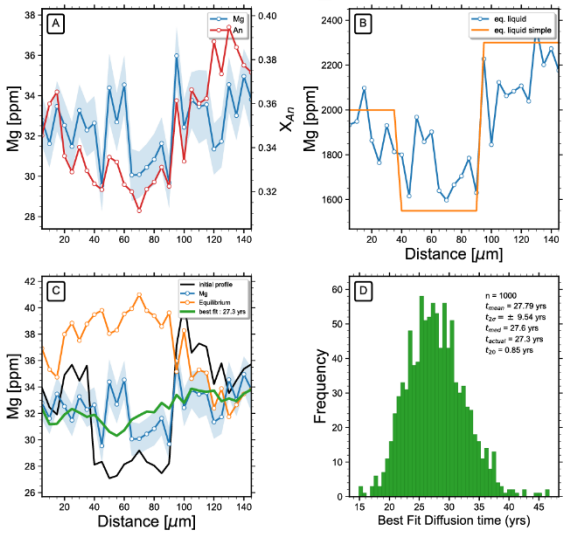

transect: 8_9

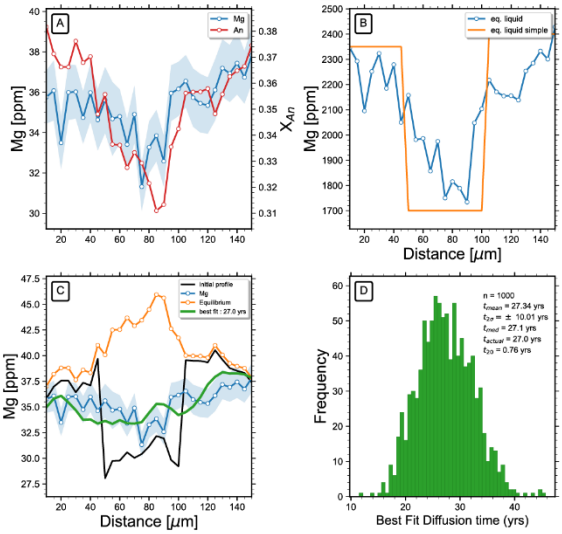

transect: 9_10_1

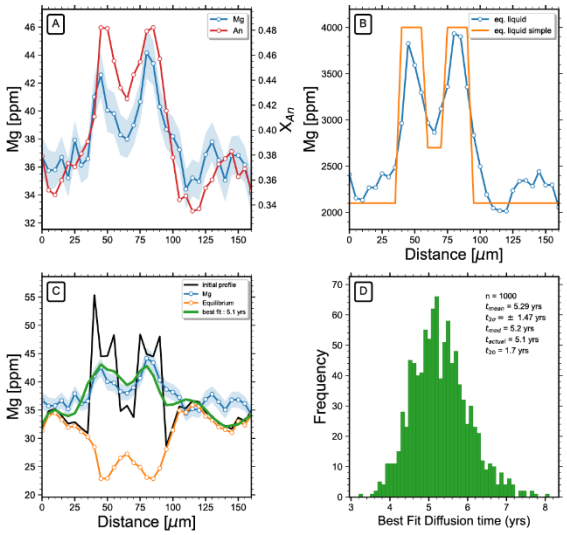

transect: 9_10_2

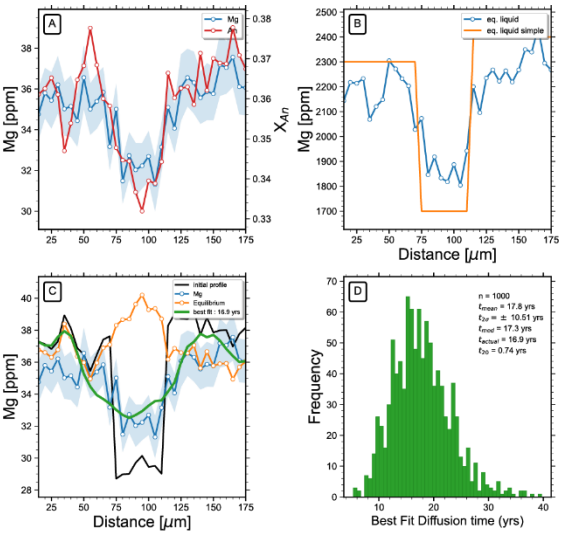

transect: 9_7

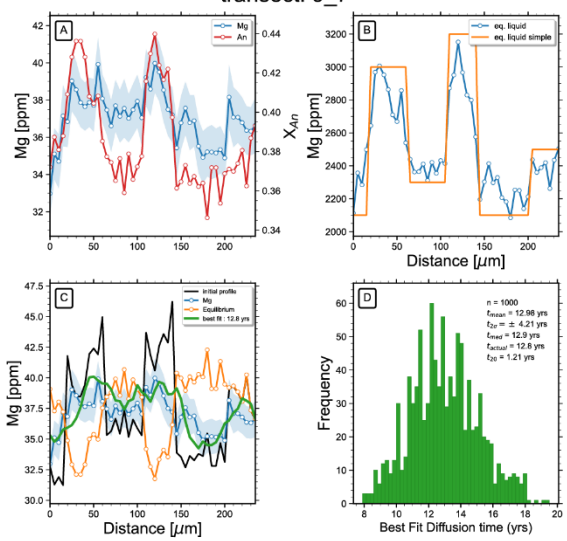

transect: ns1_1

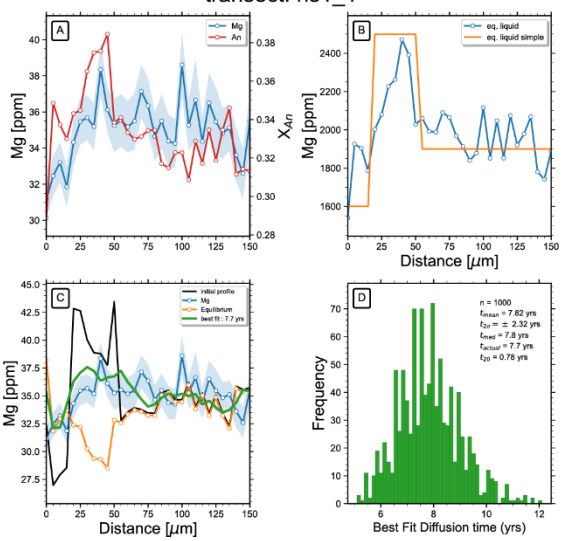

transect: ns1_3

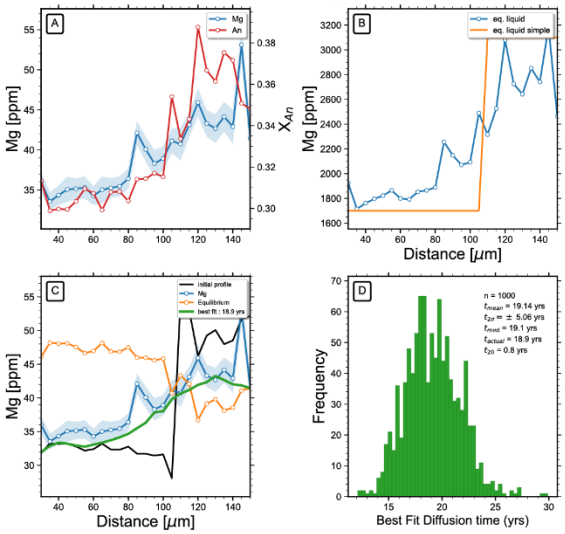

transect: ns1_5

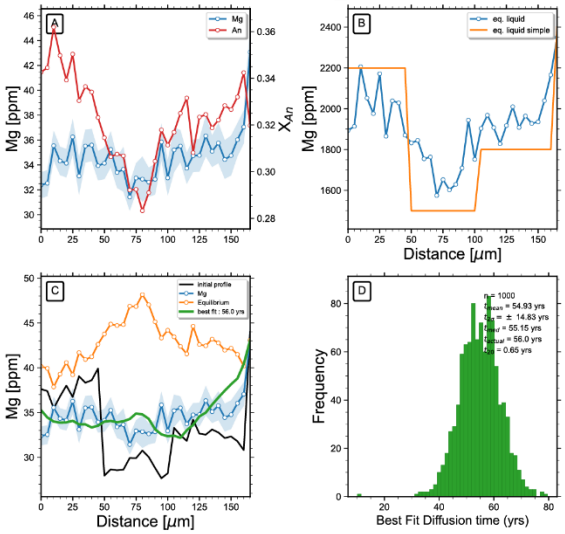

transect: ns1_6

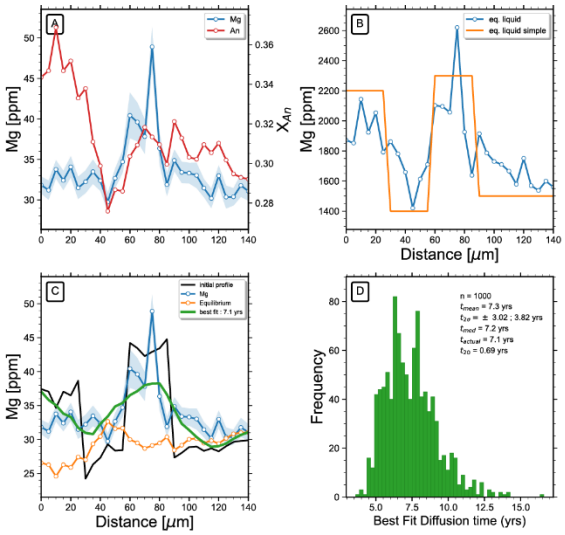

transect: ns14_2-1

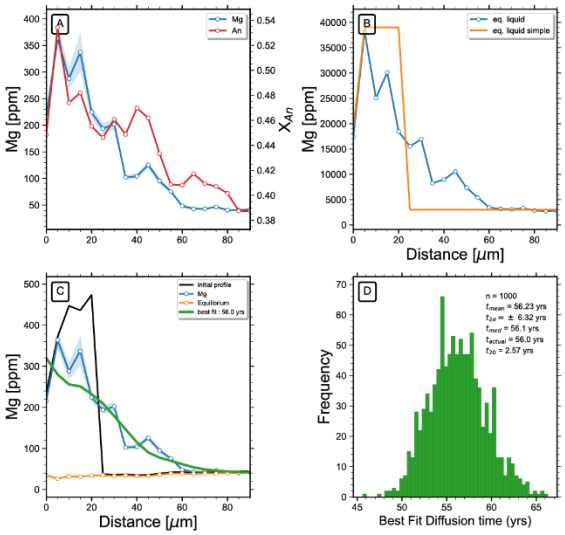

transect: ns15_1-2

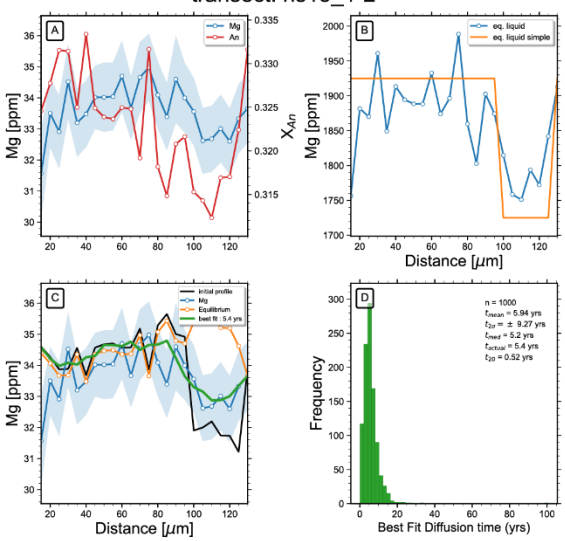

transect: ns2_2

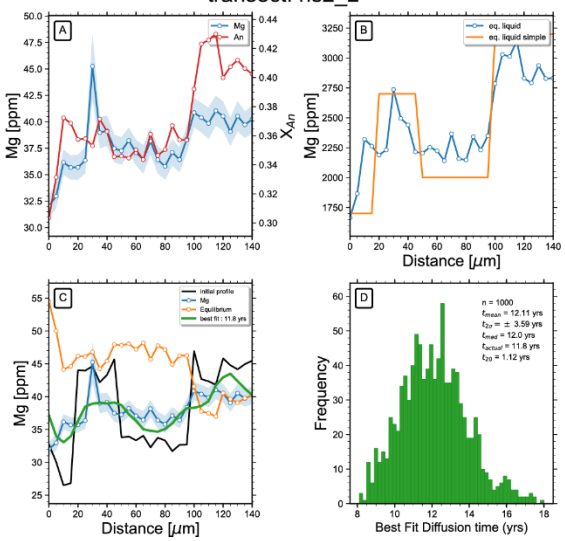

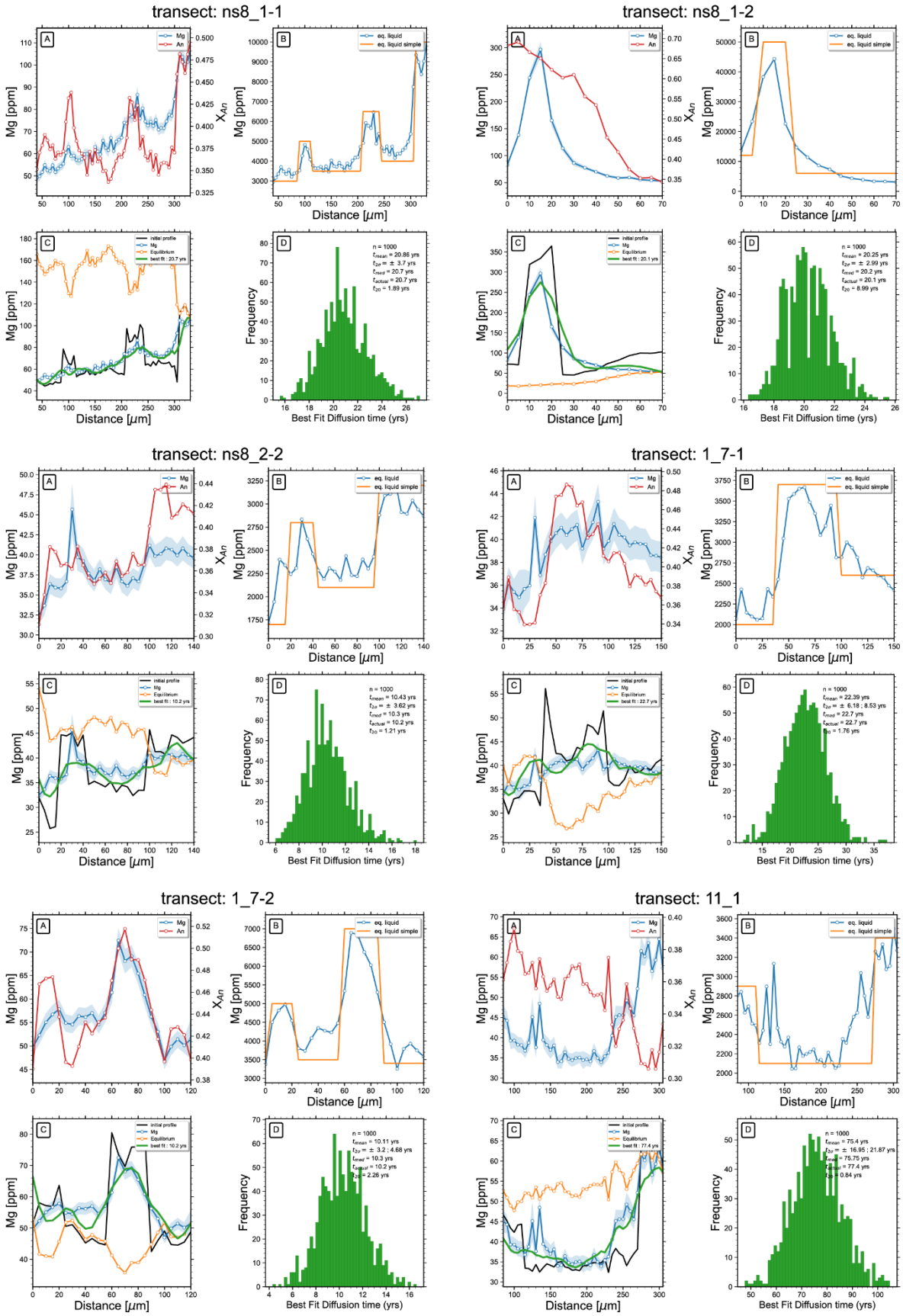
transect: ns8_1-1
transect: ns8_1-2
transect: ns8_2-2
transect: 1_7-1
transect: 1_7-2
transect: 11_1
A
B
C
D
Mg
An
eq. liquid
eq. liquid simple
initial profile
Equilibrium
Mg [ppm]
X_{An}
Distance [μm]
Frequency
Best Fit Diffusion time (yrs)

transect: 11_8_4

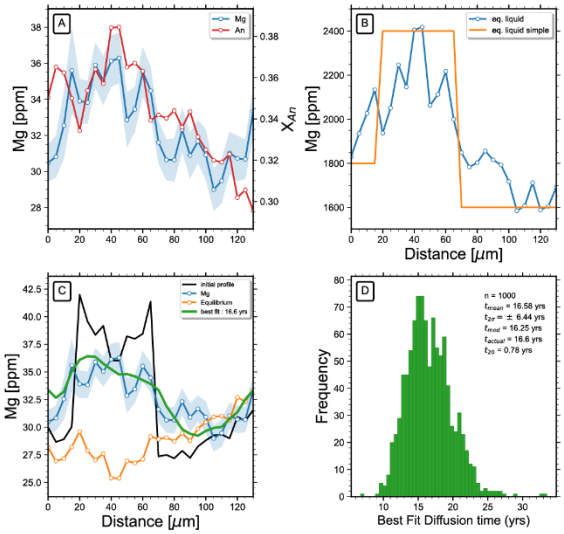

transect: 14_7

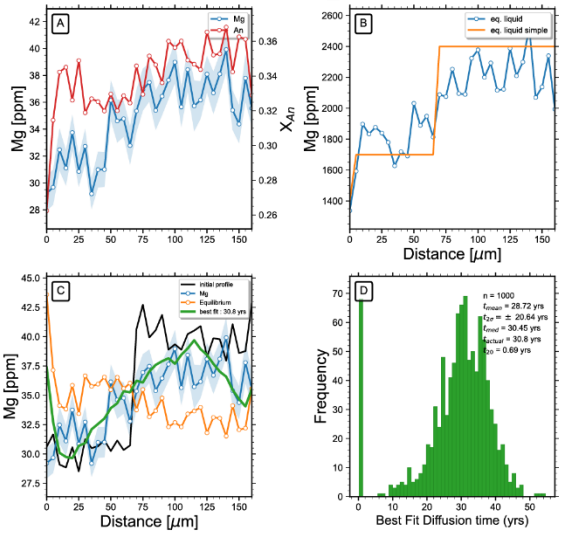

transect: 14_8_1

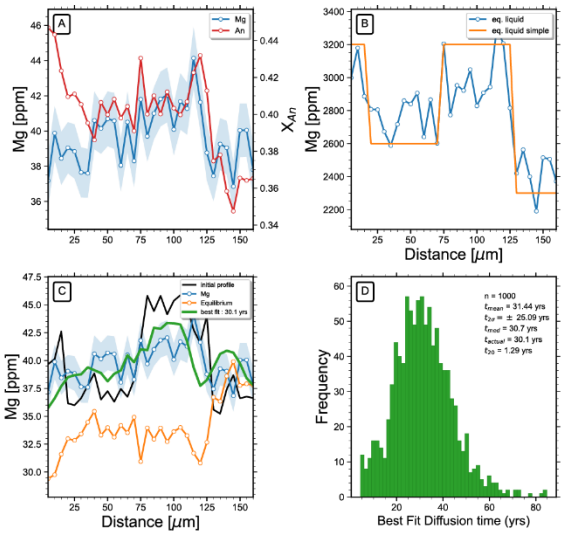

transect: 14_8_3

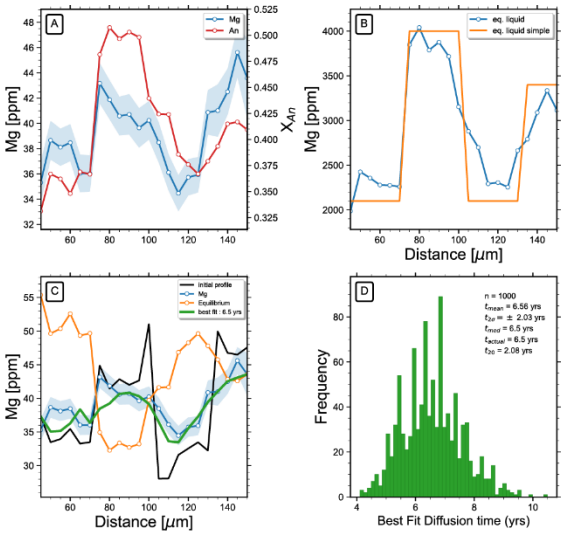

transect: 15_4

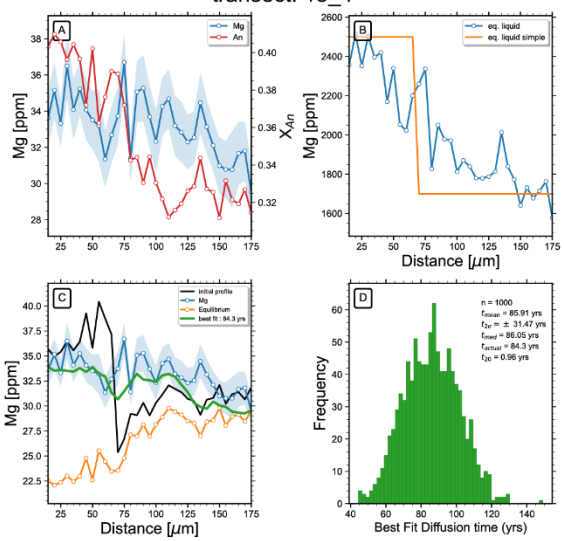

transect: 15_5_1

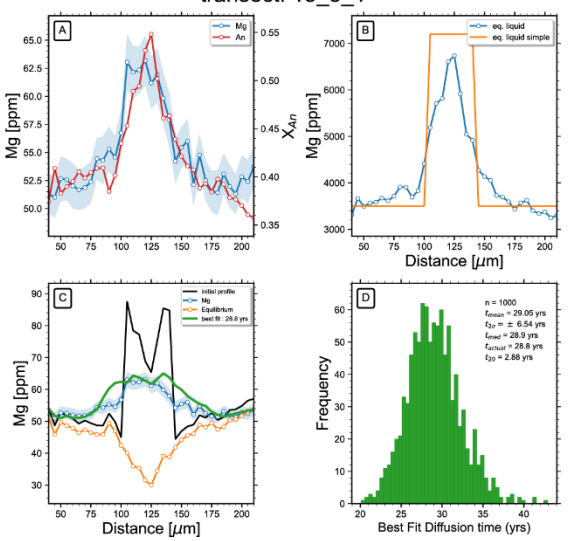

transect: 15_5_2

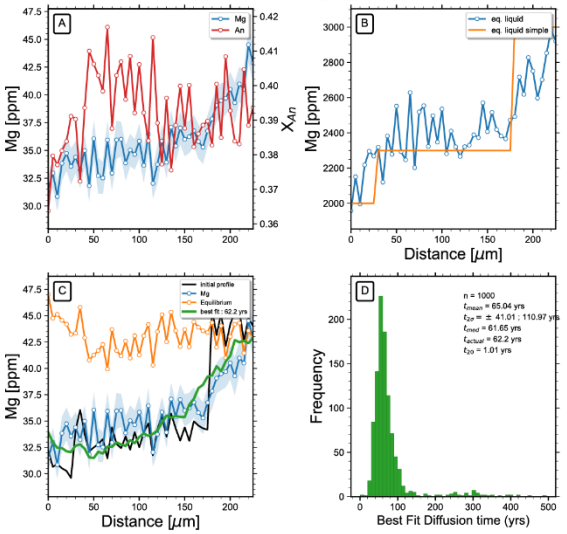

transect: 15_8

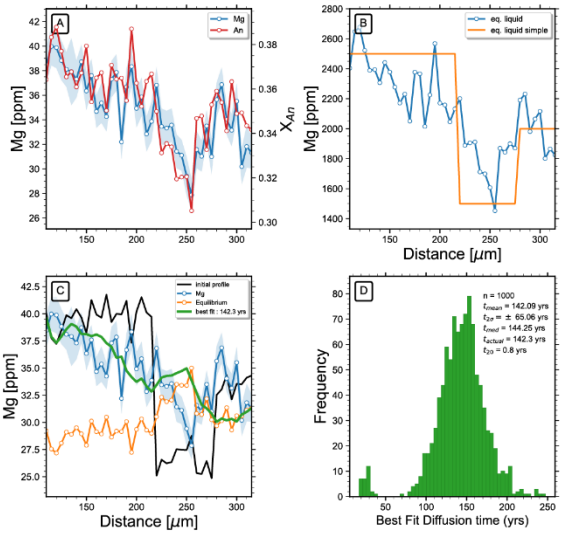

transect: 18_11_1

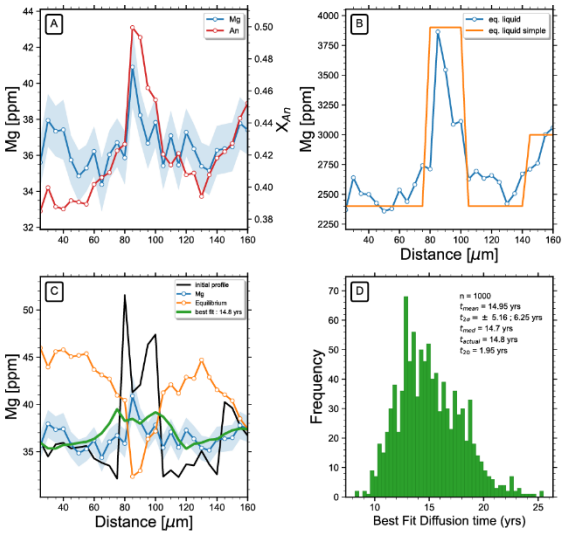

transect: 18_11_2

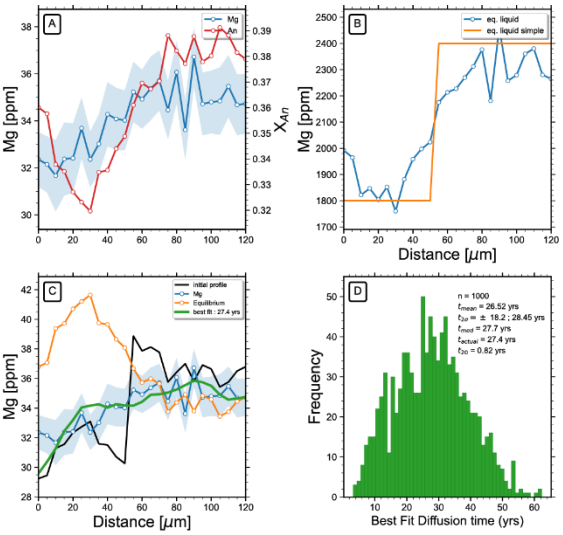

transect: 18_3_1

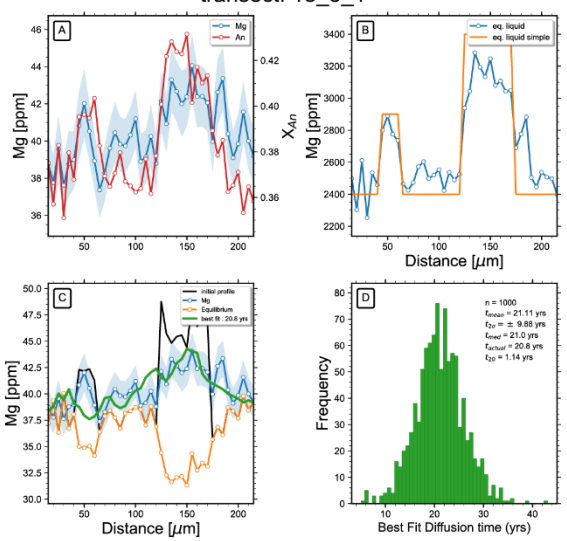

transect: 18_3_2

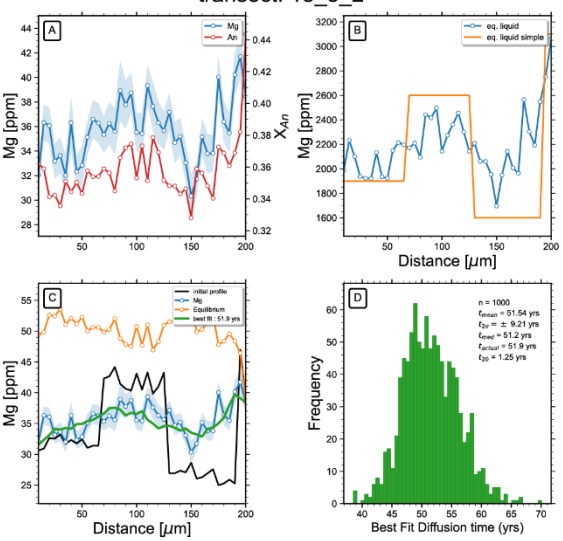

transect: 18_4_1

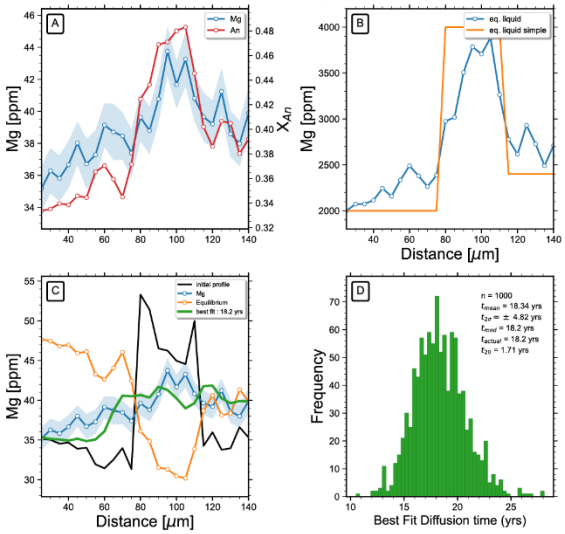

transect: 18_5_2

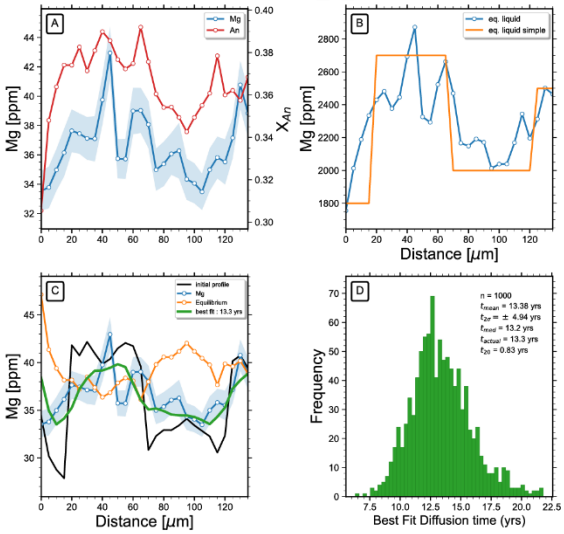

transect: 5_5

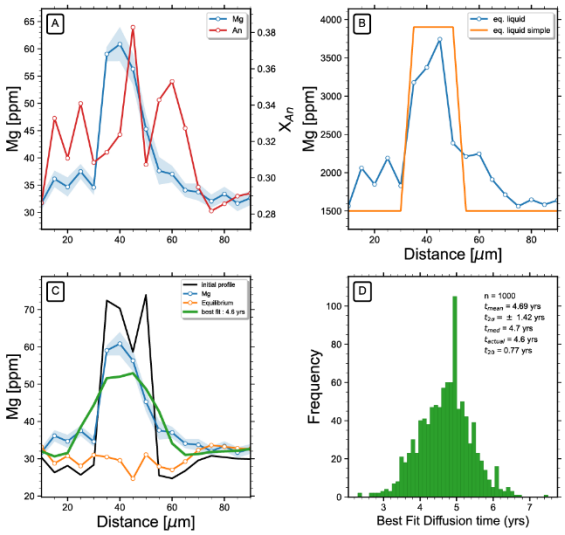

transect: 5_6

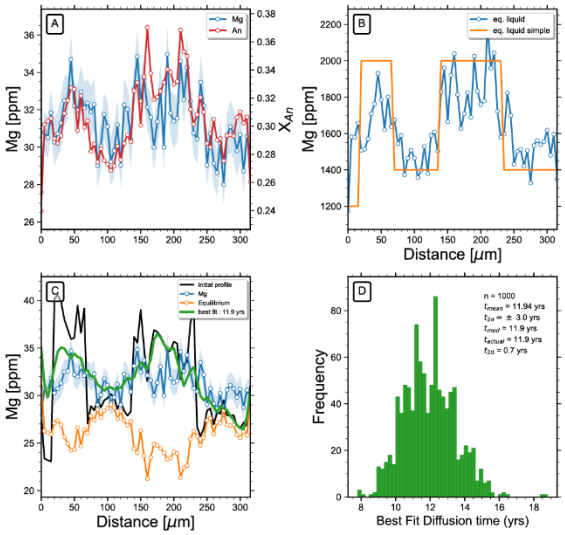

transect: 5_7-1

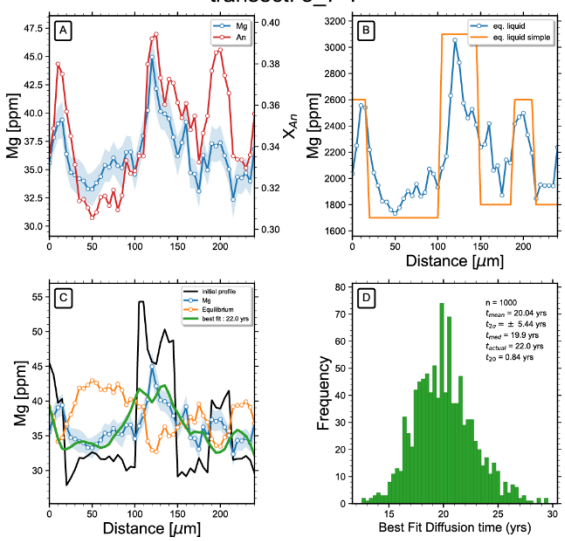

transect: 5_7-2

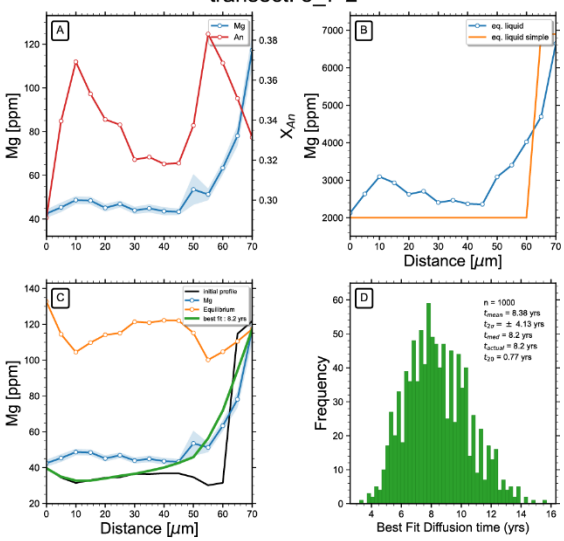

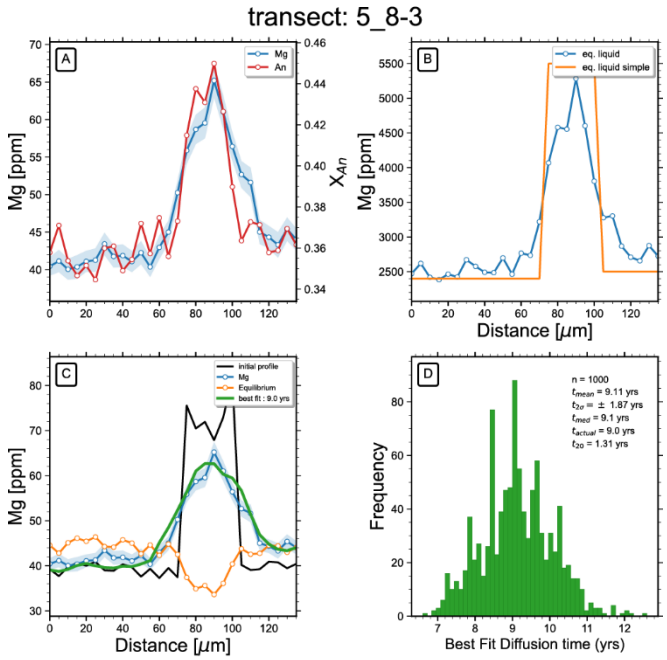
transect: 5_8-3
A
Mg
An
Mg [ppm]
X_{An}
B
eq. liquid
eq. liquid simple
Mg [ppm]
Distance [μm]
C
initial profile
Mg
Equilibrium
best fit : 9.0 yrs
Mg [ppm]
Distance [μm]
D
n = 1000
t_{mean} = 9.11 yrs
$t_{2\sigma}$ = ± 1.87 yrs
t_{med} = 9.1 yrs
t_{actual} = 9.0 yrs
$t_{2\sigma}$ = 1.31 yrs
Frequency
Best Fit Diffusion time (yrs)

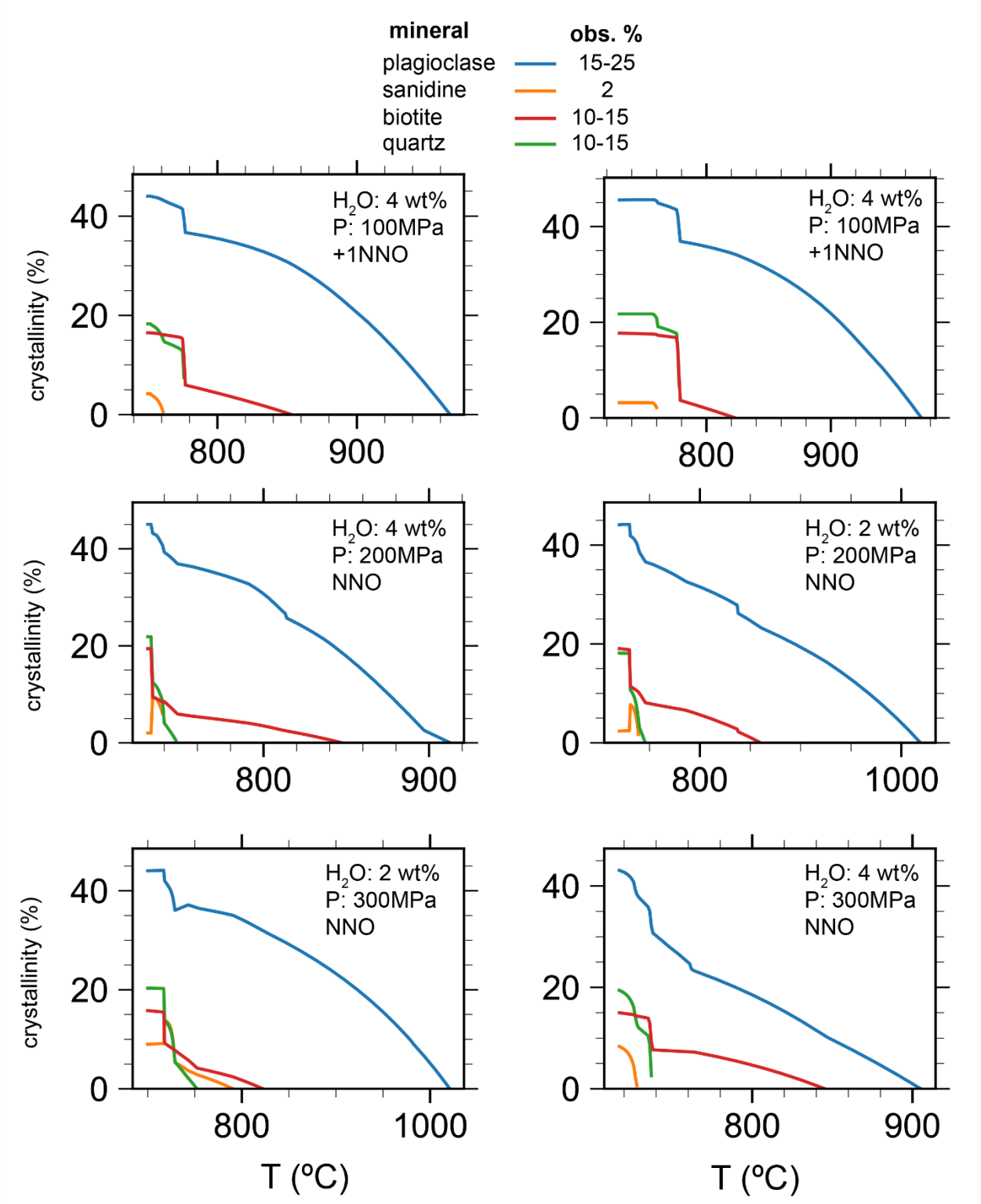

Figure S6: Representative MELTS models that produce reasonably accurate phase proportions (e.g., those that match those reported in Folkes et al., 2011) illustrating the relative position of major phases found in the CGI on the liquid line of descent. We show here that the majority of biotite and sanidine crystallization occurs late on in the CGI magmatic system.